THE INTERACTION OF GALAXIES AND THEIR SURROUNDINGS THROUGH COSMIC RAYS

RANITA JANA

Thesis submitted for the Degree of

DOCTOR OF PHILOSOPHY

Thesis Supervisor:

BIMAN NATH

Raman Research Institute
Bengaluru 560080, Karnataka, India

Jawaharlal Nehru University
New Delhi 110067, Delhi, India

Submitted: April 21, 2021

Declaration

I, ***Ranita Jana*** (Enrolment No.: RRI/2016/017), declare that the work reported in this thesis titled '***The interaction of galaxies and their surroundings through cosmic rays***', is entirely original. This thesis is composed independently by me at ***Raman Research Institute (RRI)*** under the supervision of ***Prof. Biman Nath*** and is the result of my own work unless otherwise stated. I further declare that the subject matter presented in this thesis has not previously formed the basis for the award of any degree, diploma, membership, associateship, fellowship or any other similar title of any university or institution. I also declare, this thesis has been checked through the plagiarism software TURNITIN.

Signature of Supervisor	Signature of Candidate
Prof. Biman Nath	**Ranita Jana**
Professor, RRI	Research Fellow, RRI

Astronomy & Astrophysics Group
Raman Research Institute (RRI)
Bengaluru 560080, Karnataka IN

Date:
Place:

Certificate

This is to certify that the work contained in the thesis titled '***The interaction of galaxies and their surroundings through cosmic rays***', submitted by ***Ranita Jana*** (Enrolment No.: RRI/2016/017) to the Jawaharlal Nehru University for the award of the degree of ***Doctor of Philosophy (Ph.D.)*** in Physical Sciences, is the bonafide record of orginal research work carried out by the candidate from August 2016 — March 2021, under my guidance and supervision at Raman Research Institute (RRI), Bengaluru, India. The results embodied in the thesis have not been submitted to any other University or Institute for the award of any degree or diploma.

Signature of Director	Signature of Supervisor
Prof. S. Sridhar	**Prof. Biman Nath**
Director & Professor, RRI	Professor, RRI

Astronomy & Astrophysics Group
Raman Research Institute (RRI)
Bengaluru 560080, Karnataka IN

Date:
Place:

Acknowledgements

As my 5 years long journey of being a PhD student comes to an end, I would like to thank all of you who have been an integral part of this journey. First, I would like to express my sincere gratitude to my PhD supervisor Prof. Biman Nath for his support and guidance. He constantly motivated me to take up challenging problems and work hard towards solving them. His style of working has helped to push my limits and taught a great deal of life lessons. I not only cherish our academic discussions but also our conversations on science popularization.

I sincerely thank my collaborator Prof. Peter L. Biermann (MPIfRA, Germany) for his critical approach of thinking which has greatly improved this thesis. I would also like to thank my other collaborator Dr. Siddhartha Gupta (University of Chicago), who is also my senior at RRI. He introduced me to numerical hydrodynamical simulations which has been used in a major part of this thesis. I feel blessed to have Prof. Prateek Sharma (IISC, Bangalore) as a mentor. Our bi-weekly group meetings have been immensely helpful for me to discuss new ideas.

The diverse research groups working in the Astronomy and Astrophysics department at RRI has provided me a vibrant research atmosphere. I would like to thank all the faculties, postdoctoral fellows and PhD students in the department for the stimulating discussions which has helped me to thrive. Special thanks to Sonali for your comments on the introduction chapter of the thesis.

I sincerely acknowledge the Department of Science & Technology (DST), Government of India for providing me the Institute fellowship during my PhD. I am also thankful to *Accounts Section*, *Administration* and our *Group Secretary* Harini for their help in processing official documents promptly. I have always received help from the *Computer Section* whenever I had any problem. I have been greatly benefited by the amazing collection of printed books and online resources at RRI library. Thanks to the *Library Section* for maintaining them so efficiently.

I was in high school when I decided to take up Astrophysics as my future specialization. I would like to thank Shima Ghosh Dastidar, my geography teacher, who planted this idea in my mind. Later a lot of people have nurtured this idea including Prof. Narayan Banerjee (IISER, Kolkata), Prof. Jishnu and Mira Dey (Presidency University, Kolkata) and Dr. Debi Prasad Duari (M.P. Birla Institute of Fundamental Research). My father, who has now been retired as a Physics teacher from a govt. school at a remote

village in Sundarban, is the reason I chose to do my higher studies in Physics. He is an amazing teacher who can explain physics problems in a very interactive and lucid language. He always try to find logic behind natural phenomena using the knowledge of Physics and that inspired me. My schooling has been done in Kolkata, which is hundred km away from his workplace. I used to stay with my mother, who has now retired as a nursing staff from a govt. hospital. My father used to visit us in the weekend and would teach me physics and mathematics. Both my parents have always encouraged me and motivated me to follow my dreams. I am really grateful to my mother who has raised me single handedly and has been my pillar of support through my thick and thin.

Last but not the least, I would like to thank my friends who have sticked to me through this roller coaster ride. They have constructively criticized me, questioned me and helped me to grow as an individual. My small but well packed group of friends at RRI made this journey a memorable one. Apart from that, I am indebted to my friends from my Jadavpur University days. Sumeru is one such good old friend who has saved me from the lowest point of my life by listening and giving the best advice. I am thankful to Avik for constantly motivating me from my University days through his positive attitude. I would also like to thank Subhajit for his immense support through out this journey. He has always had my back whenever I stumbled upon any confusion or difficulties and over the years, he has truly become the anchor in my life.

Contents

Synopsis

Introduction

Galaxies are the largest gravitationally bound structures in the Universe that can form stars. The morphology and star formation rate of the galaxies evolve with time. They interact with each other through merger events. They also interact with the surrounding diffuse gaseous medium in a number of ways. Both these interactions play an important role in the evolution of galaxies. The aim of this thesis is to study the interaction between galaxies and their surrounding medium.

The diffuse gaseous medium surrounding the galactic disk is known as the circum-galactic medium (CGM) and the all pervading medium between the galaxies is known as the intergalactic medium (IGM). The virial radius of the host dark matter halo of the galaxy is considered to be the boundary separating the CGM and IGM.

Galaxies continuously accrete mass from the CGM and IGM through the gravitaional potential of the dark matter halo. They also interact through stellar radiation and gaseous outflow triggered by the star formation and supernova activities. Another type of interaction that is being studied in recent times is the interaction through high energy particles or cosmic rays. We will mainly focus on the interactions involving cosmic rays in this thesis.

Cosmic ray heating of the inter-galactic medium

The high energy particles or cosmic rays are accelerated in the sites of star formation and supernova explosions in the galactic disk. They diffuse through the interstellar medium before coming out of galaxies. Then they interact with the IGM gas through *Coulomb interaction*. By this process, they lose a large fraction of their energy which eventually increases the IGM temperature.

This effect is being studied recently in light of preheating of the Universe in the beginning of Epoch of Reionization (EOR). The global 21 cm signal, which is an important probe of EOR, directly depends on the deviation of the HI spin temperature from that of the cosmic microwave background (CMB). The spin temperature is modified by the kinetic temperature of IGM filling the early Universe. Sazonov & Sunyaev (2015) worked out the global IGM temperature increase due to cosmic rays at redshift $z \sim 10-30$. Later Leite et. al. (2017) speculated that the heating of IGM through cosmic rays might be clustered around galaxies. To check this proposition, we worked out the radial as well as temporal temperature profile around high redshift galaxies. We found that for the predicted distribution of galaxies at high redshift from ΛCDM cosmology and typical values of diffusion coefficient, the increase in IGM temperature is not concentrated around the galaxies. We believe that future observations of global 21 cm radiation will shed more light on this inevitable physical process.

Another significant result from our study is that the increased temperature around the galaxies can inhibit the cosmological gas accretion. As a result, the star formation rate of the galaxy will get suppressed. Hence cosmic ray heating of IGM not only modifies the global 21 cm radiation but also plays a crucial role in the galactic evolution. These results, derived from *analytical calculations* demand further investigation through *simulations* in a cosmological set-up.

High redshift radio background due to cosmic rays

In the wake of the first ever detection of global 21 cm signal from 'cosmic-dawn' by the EDGES group, there was a concern regarding the depth of the absorption trough which was larger than expected and could not be explained by the standard ΛCDM cosmological models. There have been numerous attempts to explain the trough using high redshift radio backgrounds, dark matter particles and various other exotic physics. At the same time, there have been concerns (eg. Hills et. al. (2018)) related to the modelling and analysis of the EDGES data.

Instead of trying to *explain* the EDGES results, we put a limit on the depth of the absorption trough considering two astrophysical processes – i) radio background from population III stars and ii) cosmic ray heating of high redshift IGM. At $z \sim 20$ the first generation of stars were born in dark matter mini-halos of mass $10^{5-7} M_\odot$. Within a few Myr most of them exploded in such powerful supernova explosions that they destroyed their host halos. The high energy cosmic ray electrons accelerated in these explosion sites interacted with the intergalactic medium (IGM) magnetic field and gave rise to synchrotron emission. As a result, a uniform radio background was formed which was capable to increase the absorption trough depth. The resulting radio background from this process was found to be substantial enough to explain the EDGES result. However, the cosmic ray protons which were also accelerated at the same time were capable of increasing the temperature of the IGM which can potentially decrease the depth of the trough. The two competing processes — *the production of the radio background and the heating of IGM* — determine the depth of the

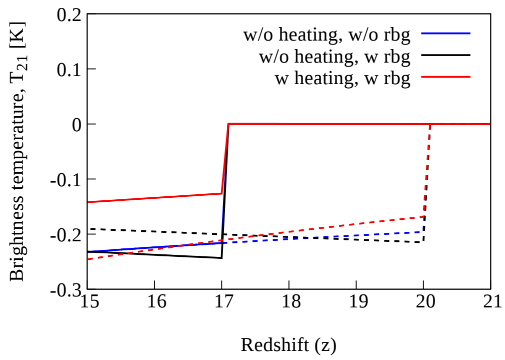

Figure 1: The evolution of differential brightness temperature of 21 cm radiation with redshift using solid (or dotted) curves if the Lyman-α coupling happened at $z \sim 17$ (or 20).

trough in 21 cm brightness temperature. We showed that the differential brightness temperature at the trough cannot be greater than ∼ 0.25 K (as seen in Fig. 1), which can be tested in future experiments.

Role of cosmic rays in galactic outflows

The process of star formation in galaxies often lead to gaseous outflows. Understanding these galactic scale outflows is important because they play a significant role in galactic evolution. Thermal pressure due to shock heating of the interstellar medium (ISM) has been the focus of most previous studies. The effect of non-thermal pressure components, such as radiation coming out from young stars and cosmic rays (CRs) have also been suggested as important driving mechanisms. However, their effects have mostly been studied in large cosmological simulations.

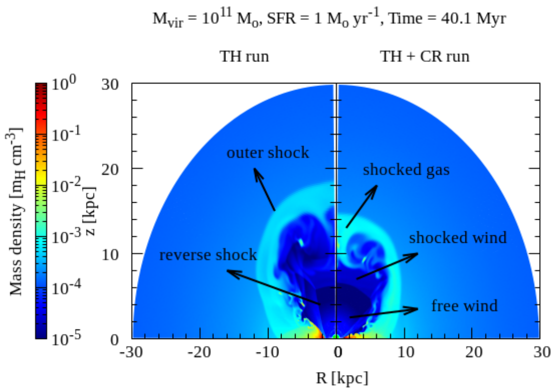

Figure 2: The gas density distribution in our fiducial galaxy after 40 Myr from the onset of star formation. The comparison between the case with (TH+CR) and without (TH) cosmic rays shows that in the early stages of galactic outflows, the dynamical role of cosmic rays is not important. See the time evolution here: https://youtu.be/3-JZAv7vwo8

The perks of doing an idealized simulation is that it allows us to distinguish the role of individual physical processes separately, which can be extended in a more realistic scenario. With the help of a simple *idealized hydrodynamical* simulation, we tried to understand how CRs play a role to launch the outflow and later how CRs impact its dynamics and morphology. To study the importance of various parameters, we performed simulations for three different galaxies of halo masses: 10^8, 10^{11} and $10^{12} M_\odot$, and three constant star formation rates (SFRs). We study the outer shock position, mass loading factor and density-temperature distribution of the outflowing gas. We suggest that at early stages of evolution, ($\lesssim$ 50 Myr, a typical lifetime over which a star of mass $> 8 M_\odot$ explode as type II supernova) when constant SFR is a justified assumption, the dynamical effects of CRs may not be as important as previously claimed, rather it can reduce the size of the outflow (as seen in Fig. 2) in most of the cases due to CR diffusion and the decrease in the effective adiabatic index.

Another crucial point to note that the gas is comparatively cold in the presence of cosmic rays which matches with earlier simulation works. However, the studies which implemented SFR coupled with the feedback, reported that inclusion of cosmic rays can increase the efficiency of the outflow as can be attested by an increase in mass loading and decrease in SFR which contradicts with our results from the early stage evolution of outflows. To see the effects in the long run we extended our simulation up to 210 Myr using a controlled time-dependent SFR and found that inclusion of cosmic rays can inhibit the formation of high-density and low-temperature gas clumps due to cosmic ray diffusion. The formation and infall of these clumps in the star forming region can increase the SFR which can potentially decrease the efficiency of purely thermally driven outflows.

Summary & Outlook

Cosmic rays play an important role in the galaxy-IGM interaction. We have studied the patchiness of cosmic ray heating of IGM around galaxies and found out the upper limit of diffusion coefficient for the heating to be inhomogeneous. We have shown that the cosmic ray heating of IGM around massive galaxies can act as a negative feedback to the star formation rate. At very high redshift, when the first stars exploded in dark matter mini-haloes, cosmic ray protons could increase the overall IGM temperature in the Universe. At the same time cosmic ray electrons interacting with the IGM magnetic field could produce a background radiation in the radio band. These two events can potentially change the characteristics of 21 cm global signal from the beginning of epoch of reionization. Cosmic rays also change the morphology and temperature of the large scale outflowing gas from the galaxies. This outflowing gas shape the multiphase structure of the CGM.

The importance of cosmic rays and other non-thermal components are studied extensively in the recent times. The contribution from non-thermal component is needed to explain the observed hot and cold phase gas density in the CGM. Particularly, cosmic rays can change the nature of thermal instability in the gaseous medium. They also play an important role in changing the ionization structure of the gaseous medium by modifying the density and temperature distributions. All these effects are being studied through analytical modeling and numerical simulations to explain the observed signatures of these very diffuse mediums. Our studies are important in the sense that it predicts the observational properties of IGM and CGM based on interactions that are inevitable. The analytical models for these interactions can be incorporated in realistic cosmological simulations and provide useful estimates for future observations.

Signature of Supervisor
Prof. Biman Nath
Professor, RRI

Signature of Candidate
Ranita Jana
Research Fellow, RRI

Astronomy & Astrophysics Group
Raman Research Institute (RRI)
Bengaluru 560080, Karnataka IN

List of Publications

Publications included in the thesis:

1. *Cosmic ray heating of intergalactic medium: patchy or uniform?*
   Ranita Jana, Biman B. Nath
   Monthly Notices of the Royal Astronomical Society, *479*(1), 153-161 (2018).
   DOI : 10.1093/mnras/sty1481, arXiv : 1806.01295

2. *Radio background and IGM heating due to Pop III supernovae explosions*
   Ranita Jana, Biman B. Nath, Peter. L. Biermann
   Monthly Notices of the Royal Astronomical Society, *483*(4), 5329-5333. (2019)
   DOI : 10.1093/mnras/sty3426, arXiv : 1812.07404

3. *Role of cosmic rays in the early stages of galactic outflows*
   Ranita Jana, Siddhartha Gupta, Biman B. Nath
   Monthly Notices of the Royal Astronomical Society, *497*(3), 2623–2640 (2020).
   DOI : 10.1093/mnras/staa2025, arXiv : 2007.00696

Other publication (not included in the thesis):

1. *Gamma-ray and radio background constraints on cosmic rays in Milky Way circumgalactic medium*
   Ranita Jana, Manami Roy, Biman B. Nath
   The Astrophysical Journal Letters, *903*(1) (2020)
   DOI : 10.3847/2041-8213/abbee4, arXiv : 2007.11015

List of Figures

List of Tables

1

Introduction

1.1 Galaxies now and then

Galaxies are the largest gravitationally bound structures in the Universe that can form stars. The exact time after the Big Bang when the galaxies started to form is a debatable topic, though it is evident that galaxy formation is an ongoing process. Galaxies, which are the building blocks of the Universe, evolve with time. The evolution of the galaxies manifests itself through the change in their morphology and star formation rate. The interaction between galaxies (i.e. merger events) as well as the interaction between galaxies and their surrounding medium both play a role in their evolution. The field of formation and evolution of galaxies has developed through observational surveys as well as theoretical and numerical modelings.

It was believed for a long time that the Milky Way was the entire Universe. All the stars and nebulae were thought to be the part of our galaxy. Hubble (1929) first confirmed that our Milky Way is not the only galaxy in the Universe. Subsequent improvement in resolution of the telescopes made it possible to find the light distributions (de Vaucouleurs 1948; Sérsic 1963) and to resolve different components (Kormendy, 1977) of the galaxies. A revolutionary change came in the study of galaxies with the advent of photometry, particularly with the use of charged coupled devices (CCDs). With the launch of Hubble Space Telescope (HST) in 1990 (still in operation), high resolution images of galaxies in ultra-violet, visible and infra-red bands became accessible. A large number of high redshift galaxies became observable in the late 1990s (Williams et al., 1996) with the Hubble Deep Field (HDF) surveys and Lyman-break techniques (Steidel et al., 1996). This allowed us to estimate the redshift of distant and faint galaxies using photometric techniques. Both photometric and spectroscopic techniques of measuring redshifts revealed that galaxies at redshift $z > 1$ are very different from present day galaxies (van den Bergh et al., 1996). Most of the galaxies at high redshift did not posses any particular shape, rather they resembled a deformed cloud like structure.

1.1.1 Formation of first galaxies

Theoretical framework : The ΛCDM model is the widely accepted cosmological model of structure formation. According to this model of cold dark matter (CDM, Λ being the cosmological constant) particles, small perturbations in the dark matter density distribution at early Universe gravitationally collapsed and formed stable dark matter halos. In the history of the Universe, the epoch of recombination (see Fig. 1.1) is the era when the

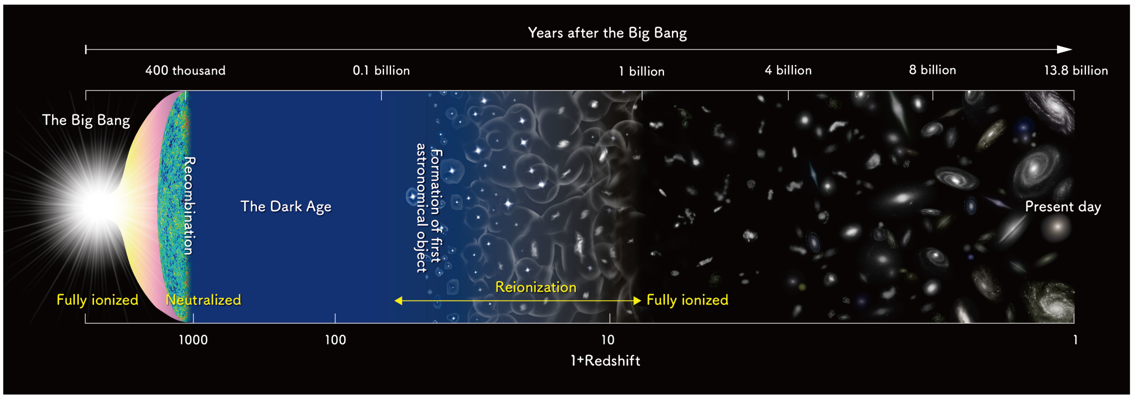

Figure 1.1: Timeline showing the important epochs of the Universe. Image credit: NAOJ

Universe became cold enough since Big Bang so that electrons and protons combined to form hydrogen (H) and helium (He). The baryonic matter, mostly H and He, was accreted by the gravitational potential wells of the dark matter halos. Thus the first sites for galaxy formation were prepared. As time progressed, small dark matter halos merged together to form larger halos and hence a hierarchical structure formation started.

Observation and Simulation : Before the epoch of recombination, matter and radiation were in thermal equilibrium and free electrons would scatter the photons, thus making the Universe opaque. Once the free electrons were captured in neutral atoms the photons could stream freely. This radiation from the epoch of recombination formed a background radiation at present in the microwave band which is known as the Cosmic Microwave Background (CMB) radiation (Penzias & Wilson, 1965). Since the radiation and matter were in thermal equilibrium, any matter density perturbation would be imprinted in the CMB. Hence this radiation from the last scattering surface helps us to constrain different cosmological parameters (Planck Collaboration et al., 2016) of the ΛCDM model. Using these Cosmological parameters, it is now possible to simulate the formation and evolution of galaxies through large scale hydrodynamical simulations. Illustris (Vogelsberger et al., 2014a), Eagle (Schaye et al., 2015), SIMBA (Davé et al., 2019) and NewHorizon (Dubois et al., 2020) (see Fig. 1.2) are some of the most well-known projects for performing cosmological zoom-in simulation. These simulations provide us the estimates for observables, such as the galaxy mass function, cosmic star formation rate, galaxy metallicities, stellar to halo mass ratio etc. The estimates from these simulations match very well with the existing observations. These successes form basic pillars of the theory of galaxy formation and evolution.

1.1.2 Properties of first galaxies and stars

The simple hierarchical structure formation was perturbed by the formation of first stars or the population III stars. It is understood that first stars appeared in dark matter halos of mass $\sim 10^{6-7}\,M_\odot$ which collapsed at redshift $\sim 20-30$ (Couchman & Rees 1986;

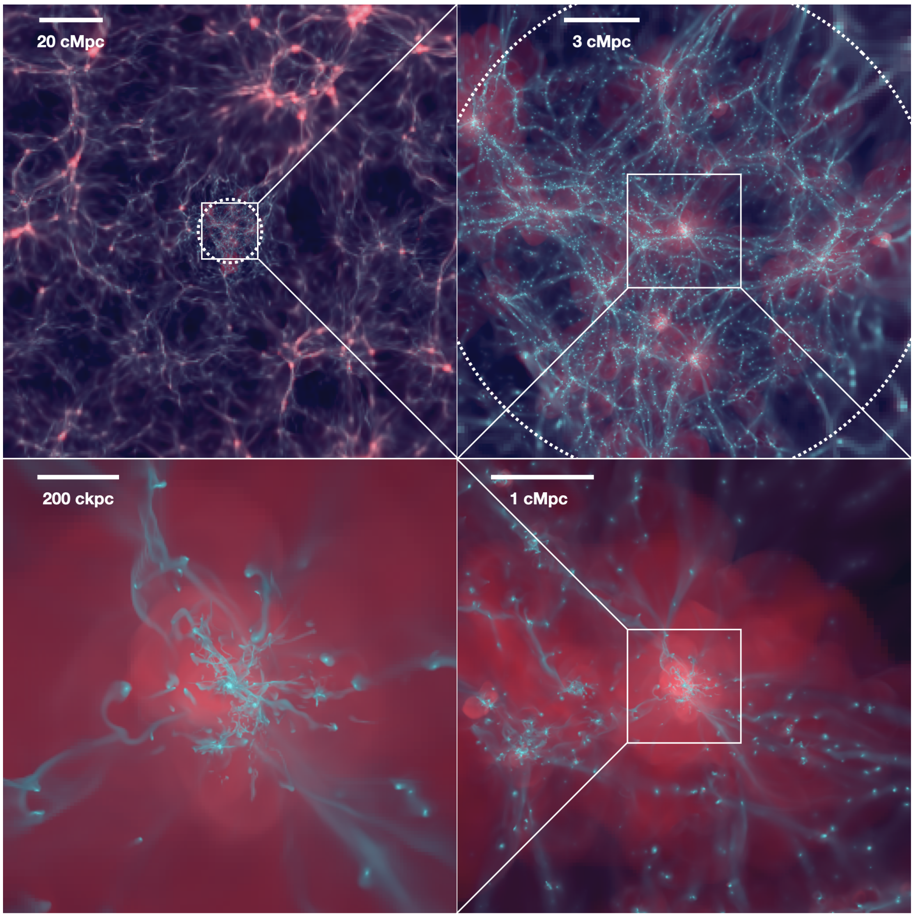

Figure 1.2: The sequential zoomed in region (clockwise from top left) of the NEWHORIZON simulation (Dubois et al., 2020) shows the projected density (silver blue) and projected temperature (red) at redshift $z \sim 2$. The plots gradually zoom over one of the most massive galaxies within the simulation box starting from a cosmic web structure. The scale of the plot is given in comoving Mpc or kpc unit.

Tegmark et al. 1997). It is useful to assign a temperature, $T_{\rm vir}$ [1] to the baryonic gas within dark matter halo, assuming the halo to be in virial equilibrium. The virial temperature of these low mass halos is,

$$T_{\rm vir} \approx 860\,\mathrm{K} \left(\frac{M_{\rm vir}}{10^7 M_\odot}\right)^{2/3} \left(\frac{1+z}{21}\right) \tag{1.1}$$

However, the threshold of efficient atomic line cooling of hydrogen (H) gas is 10^4 K. Hence the primordial gas accreted by these small halos can be cooled via molecular (H_2) rotational and vibrational transition lines. Yoshida et al. (2003) showed that the lowest mass halo that can host cold molecular gas which is essential for star formation has a mass $\approx 7 \times 10^5\, M_\odot$. This critical mass is weakly dependent on redshift of collapse for $z > 16$. These small halos are usually termed as mini-halos and they are very different from our

[1] In general, the gas within a virialized halo has a temperature profile and also has a multiphase structure. However, assigning a single temperature to the gas is useful to make order of magnitude estimates.

concept of galaxies. They certainly did not possess disks and were more likely a gaseous cloud residing in a dark matter halo.

The cooling of gas accreted in these mini-halos and their further fragmentation lead to the first star formation in the history of the Universe. These stars were formed from cold molecular primordial gas mainly consisting of hydrogen and helium, without any heavier metals (i.e. elements with atomic number higher than H and He). These first stars were massive with mass $\sim 100 - 1000\, M_{\odot}$. The dominant nuclear fusion reaction in population III star was the proton-proton (p-p) chain reaction in the absence of any heavier element. The reaction rate of p-p chain is proportional to T^4 where T is the core temperature. Due to the massive size of the population III stars, the reaction rate had to be large enough to balance the inward force of gravity and maintain the hydrostatic equilibrium. Hence these stars had a higher luminosity and as a result, a smaller lifetime, compared to stars with smaller mass. The massive population III stars exhausted their fuel supply within several million years. Depending on their mass either they exploded in powerful pair-instability supernovae (PIS) or they formed black holes. Each pair-instability supernova produced kinetic energy equivalent to $\sim 10^{52} - 10^{53}$ erg. On the other hand, the binding energy of a mini-halo was $E_{\mathrm{b}} \sim 10^{49} - 10^{51}$ erg. Hence the energy emitted by each supernova was at least an order of magnitude larger than the binding energy of the mini-halo (Heger & Woosley 2002; Tominaga et al. 2007; Heger & Woosley 2010). This implies that a single pair-instability supernova was capable to disrupt its host halo.

1.1.3 Present day galaxies

Galaxies which we observe today in our local Universe are very different from high redshift proto-galaxies described in Sec. 1.1.2. Most of the present day galaxies have either an elliptical or spiral structure while a few of them have an irregular structure which we often call dwarf irregular galaxies because of their smaller mass ($M_{\mathrm{vir}} \sim 10^{7-9}\, M_{\odot}$). Hubble first classified galaxies depending on their shape. Though this classification may not offer much physical insight of galaxies, it was phenomenal at a time when the celestial objects were identified based on their shape only. The galaxies can change their shape in the course of evolution or due to merger events.

- **Spiral galaxy:** Our Milky Way Galaxy is an example of a spiral galaxy. These galaxies consist of a central bulge, a spherical halo, disk, spiral arms and sometimes a bar-like structure at the center. The spiral arms in the galactic plane are the star-forming regions where new or population I stars form. The spiral galaxies host mainly young, massive, blue stars and emission nebulae. The comparatively old population II stars can be found only in the globular clusters found in the galactic halo of such galaxies. The available observational data suggests that the visible mass of a spiral galaxy remain in the range of 10^9 to $10^{12}\, M_{\odot}$ (Eufrasio et al., 2014).
- **Elliptical galaxy:** Elliptical galaxies have a structure that resembles an ellipsoid.

Figure 1.3: The left panel shows the face on view of the spiral galaxy M100. The middle panel shows a giant elliptical galaxy ESO 325-G004 and the right panel shows our nearest extragalactic candidate, Large Magellanic Cloud, an irregular galaxy. Image credit: NASA, ESA

The shape can vary over a wide range, starting from a spheroidal to a flattened disk like structure but without the presence of spiral arms. Generally, they do not have active star formation going on. The stars in these galaxies are mainly old and red (Holmberg, 1958) population II stars. The total mass of an elliptical galaxy can be as large as a few times $10^{13}\,M_{\odot}$ (for eg. ESO 146-IG 005 in the center of the Abell 3827 cluster). On the other hand, elliptical galaxies can also be so small (and luminosty similar to brightest globular clusters) that they are sometimes referred to as 'dwarf spheroidal' or 'dwarf elliptical' galaxies (for eg. M32 which is a companion of the Andromeda or M31 galaxy).

- **Irregular galaxy:** The galaxies which do not fall into any of the above two categories and have a disorganized shape are called irregular galaxies. Large Magellanic Cloud (LMC) and Small Magellanic Cloud (SMC) fall in this category. They are usually smaller than the spiral galaxies and they are often found in association with large spiral galaxies.

1.2 Surrounding medium of galaxies

Baryons constitute only $\sim 5\%$ of the total matter-energy density of the Universe. The collapsed objects including the galaxies and clusters of galaxies contribute only $\sim 10\%$ of the total baryon content (Fukugita & Peebles 2004; Shull et al. 2012) of the Universe. Rest of the baryons from Big Bang nucleosynthesis can be found in a diffuse form surrounding the isolated galaxies and inside and outside of the galaxy clusters. This diffuse medium is a mixture of pristine primordial gas that has not been collapsed gravitationally and the gas that is thrown out of the galaxies in different feedback channels.

The diffuse gaseous medium has been named depending on the baryon over-density, temperature and its location in the cosmic web of structure formation. The low density gas shock heated to the virial temperature residing outside the star forming region and

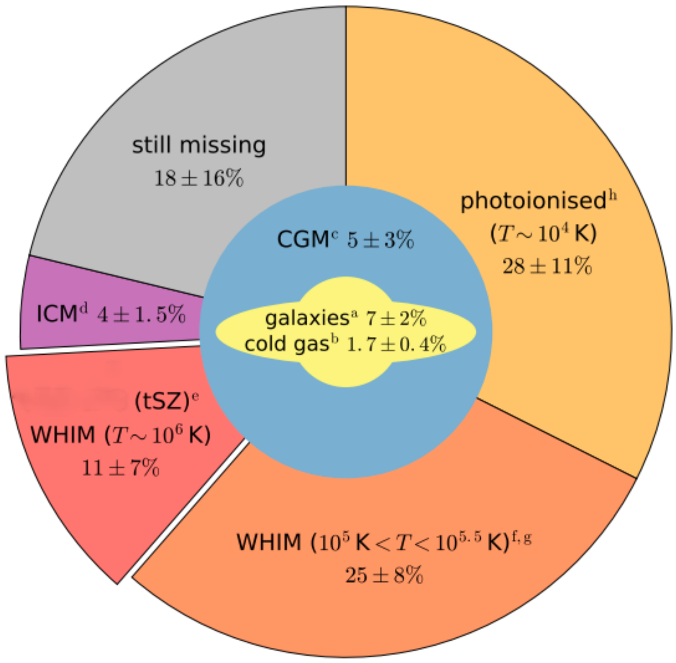

Figure 1.4: Baryon budget of the Universe at present. Galaxies together with the stellar and cold gas components constitute ~ 10% of the total baryon budget. The circumgalactic medium (CGM), intergalactic medium (photoionized and warm-hot IGM i.e. WHIM) and intracluster medium (ICM) constitute ~ 70% of the budget while the remaining ~ 20% is still missing. The figure is taken from de Graaff et al. (2019)

.

within the virial radius of the dark matter halo is known as the circumgalactic medium (CGM). The diffuse gas outside the virial radius of the halo and residing in the space between the galaxies is termed as the intergalactic medium (IGM). The superheated gas ($T \sim 10^7 - 10^8$ K) present in the galaxy clusters is known as the intracluster medium (ICM). ICM, IGM (photoionized and warm hot IGM i.e. WHIM) and CGM contributes to the ~ 70% of the cosmic baryon budget (as shown in Fig. 1.5). It is possible that remaining ~ 20% of the baryons are yet to be observed and this is referred as the *missing baryon* problem. We will focus mainly on the IGM and CGM here.

1.2.1 Intergalactic medium

The all-pervading medium in the Universe which fills the space between the galaxies is known as the intergalactic medium (IGM). This medium is a 'source' of material that gets accreted by the galaxies. This accreted gas then gets cooled, forms stars by thermonuclear reactions. The IGM also acts as a 'sink' for the matter (mainly metals) and radiation which are produced by the stars and expelled out of the galaxies by energetic supernova explosions. Hence, basically the gas in the intergalactic medium gets recycled by the galaxies continuously. As a result, the intergalactic gas carries the signature of the physical changes happening over the entire period of the evolution of the Universe.

The mean density of hydrogen in the intergalactic medium at redshift of z can be expressed (for eg. Madau 2000) in terms of Cosmological parameters

$$\begin{aligned}\bar{n}_{\rm H} &= (\rho_{\rm crit}/m_{\rm H})\,(1-Y)\,\Omega_{\rm b}\,(1+z)^3 \\ &= 1.6\times 10^{-7}{\rm cm}^{-3}\left(\frac{\Omega_{\rm b}h^2}{0.019}\right)(1+z)^3 \end{aligned} \tag{1.2}$$

where $\rho_{\rm crit} = 3H_0^2/(8\pi G)$ is the critical density, $m_{\rm H}$ is the mass of a Hydrogen atom, $Y \sim 0.247$ is the primordial Helium abundance by mass, $\Omega_{\rm b} = \rho_{\rm b}/\rho_{\rm crit}$ is the present baryonic density fraction and $H_0 = 100\,h$ km s^{-1} Mpc^{-1} is the present value of Hubble constant. The distribution of matter in the IGM is not uniform. Most of the information about the density and temperature distribution of IGM has been obtained through the absorption line study in the spectra of a distant quasar or a galaxy.

Observational signatures of IGM : The neutral hydrogen atoms in the intervening medium between the quasar and the observer undergoes Lyman-α transition. It gives rise to absorption lines in the quasar spectra. The equivalent width of the absorption lines help us to estimate the column density ($\int n_{\rm HI}\,dl$) of the neutral hydrogen atoms in the line of sight of the quasar. These narrow redshifted absorption lines arising due to the neutral hydrogen clouds present at different distances from the observer is known as Lyman-α forest (Gunn & Peterson 1965; Lynds 1971). Not only this, the absorption lines of heavy elements or metals (eg. CIV, OVI etc.) can be observed in higher resolution and higher signal to noise ratio quasar spectra. The heavy elements can only be produced inside the galaxies. Hence this is the observational proof that IGM gets contaminated by large scale galactic wind which are capable to carry metals with them. With the advent of high resolution radio telescopes like LOw Frequency ARray (LOFAR), the Murchison Widefield Array (MWA), the Precision Array to Probe the Epoch of Reionisation (PAPER) and Experiment to Detect the Global EoR Signature (EDGES) the 21 cm radiation from neutral hydrogen atom can also be used as a probe of the diffuse IGM. We will discuss it in detail in Section 1.4

1.2.2 Circumgalactic medium

The hot and tenuous gas present outside the galactic disk is known as the circumgalactic medium (CGM). The virial radius of the dark matter halo of the galaxy is considered to be the outer boundary of CGM. The CGM has a multiphase structure, the hot phase has a temperature which is equal to the virial temperature of the halo and the cold phase has a temperature $\sim 10^4 - 10^5$ K. The existence of CGM was first discovered in our Milky Way galaxy (Münch & Zirin, 1961) and later a similar gas distribution was observed in other galaxies (Putman et al., 2012) as well. The circumgalactic medium contains a significant fraction ($\sim 5\%$) of the total baryons of the Universe.

How gaseous halos are formed : The gas from the intergalactic medium gets accreted by the dark matter halo and gets heated due to accretion shock. The shock heated gas gets cooled by radiative cooling. If the cooling time ($t_{\rm cool}$) is very small compared to the free

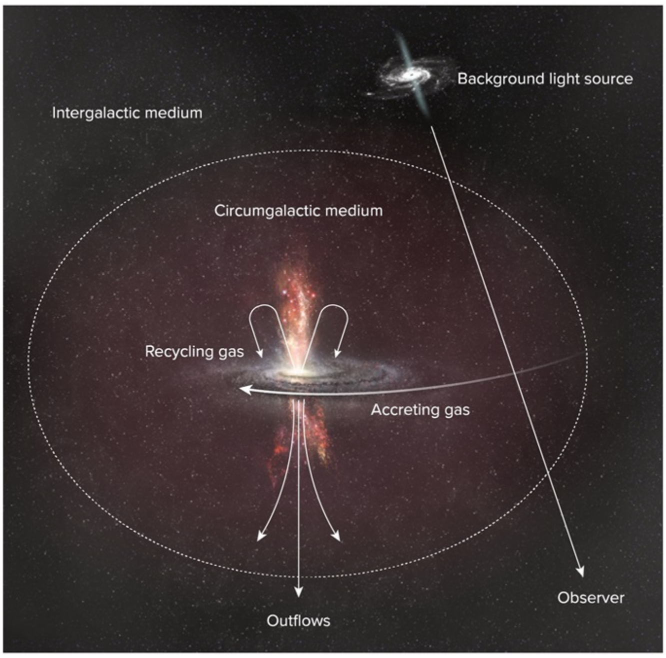

Figure 1.5: The schematic diagram shows how the diffuse gas in IGM and CGM recycle the gas within the galaxy. The figure also shows that the absorption spectra of distant quasars reveal the properties of the diffuse gaseous medium between the quasar and the observer. Image credit: ESO/M.Kornmesser

.

fall time of the accreted gas ($t_{\rm ff}$) the gas gets cooled very fast and it rains down on the galactic disk. This infalling cold gas acts as the fuel for the star formation. On the other hand if the ratio of cooling time to free fall time $t_{\rm cool}/t_{\rm ff} >> 1$ the gas gets compressed quasi-statically (Birnboim & Dekel, 2003) and the hot gas remains suspended above the galactic plane for a long enough time compared to the age of the galaxy. This process is known as 'virialization' of halo gas. The hot gas around the galactic disk forms a halo like structure which is sometimes called the 'galactic corona'. The CGM gas maintains a stable hydrostatic equilibrium balancing the inward pull of gravity by the thermal pressure. The cold phase of CGM gas is formed due to the thermal instabilities created by either the accretion shock or the shocks produced by the galactic outflow.

Observation and Simulations : Similar to IGM, the major observational probe of CGM is also the quasar absorption spectra. The advantage of this method is that i) it is sensitive to extremely low column density ($N \simeq 10^{12}\,{\rm cm}^{-2}$) and ii) the sensitivity does not depend neither on redshift nor on the luminosity of the host galaxy. Though most of the absorption line studies are done in UV and optical (for eg. *Sloan Digital Sky Survey* and *Cosmic Origins Spectrograph*), X-ray telescopes (*Chandra* and *XMM*) are also being used to constrain the hot gas component of CGM through X-ray emission. Emission line measurements are difficult for the diffuse medium since it scales as $\propto n^2$ and CGM density is $n_H \sim 10^{-2}\,{\rm cm}^{-2}$ or less. However, 21 cm emission has been used to trace the high velocity clouds (HVCs) in the Milky Way galaxy and the same technique has been used for external galaxies as well (Putman et al., 2012). Apart from the observational probes, numerical simulations are being used to build physically motivated models for CGM. Large scale cosmological zoom in simulations (Oppenheimer & Davé, 2006) are excellent probe to study the multiphase structure of CGM with gas in different temperature bins, the ionization structure and chemical composition of the gas. On the other hand, very small scale (<< parsec) simulations are performed to understand the stability of cold gas phase in the background of hot phase (Armillotta et al. 2017; Gronke & Oh 2020) and the formation and evolution of thermal instabilities (Butsky et al., 2020).

1.3 Modes of interaction with surroundings

Galaxies are not 'island universes' as used to be believed earlier. They interact with each other and also with their surrounding medium. The mode of interaction may be gravitational, through radiation and gaseous outflows or through high energy particles known as cosmic rays. Though the aim of the thesis is to focus on the interactions involving cosmic rays, we briefly summarize all modes of interaction. We also provide a brief introduction to the 21 cm signal from neutral hydrogen gas which is an important probe of IGM gas at high redshift. This will be helpful as we will discuss the observational impact of cosmic ray-IGM interaction in the next chapters.

1.3.1 Interaction through gaseous inflow

Observation of galaxies at different redshift suggest that there is continuous gas accretion from the intergalactic medium.

- *Gas depletion time « Hubble time :* Gas depletion time i.e. the ratio of gas content to the star formation rate of the galaxy is an indicator of how quickly the gas content of the galaxy gets depleted. The observation of galaxies (Genzel et al., 2010) at high redshift ($z > 1$) reveal that gas depletion time is less than a Gyr (≈ 0.5 Gyr) while the same for the galaxies at lower redshift ($z \sim 0$) is slightly higher (≈ 1.5 Gyr). However, the gas depletion time is very small compared to the Hubble time ($1/H_0 \sim 14$ Gyr, assuming $H_0 = 67.74$ km s^{-1} Mpc^{-1} (Planck Collaboration et al., 2016)) at all redshift. The Hubble time at a given redshift is the time required for the Universe to expand to the size at that redshift. This indicates that there must be some gas replenishment from the intergalactic medium otherwise there should not have been any star forming galaxies today.

- *SFR density increases steeper than expected :* Another observation that justifies the scenario of continuous gas accretion by galaxies is the absence of a direct correlation between the decline in HI mass density and the increase in stellar mass density over the cosmic time. Figure 1.6 shows that with decreasing redshift the stellar mass density (purple shaded area) increases with a steeper slope compared to what is

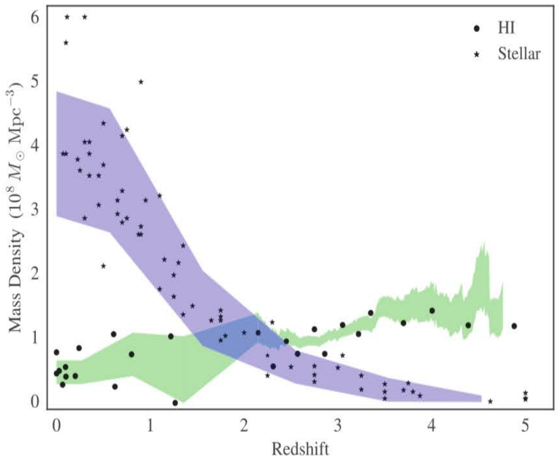

Figure 1.6: The figure shows the evolution of stellar mass density (purple shaded area) and HI mass density (green shaded area) with redshift. The figure is taken from Putman (2017)

expected from the decreasing trend in HI mass density (green shaded area). The steeper slope of stellar mass density justifies continuous gas accretion from IGM to fuel the star formation.

- *G-dwarf problem :* There is another indirect observation which can be explained by the accretion of low metallicity gas from IGM. It was noticed that in the solar neighbourhood, there is a deficiency of metal poor G-dwarf stars (van den Bergh 1962; Schmidt 1963; Tinsley 1980) compared to what is expected from simple closed box galaxy evolution models. The same is true for other class of stars, however, since the age of the G-dwarf stars are close to the age of the galaxy, they were selected to model the galactic chemical evolution. Not only in local Universe, where the metallicity of individual stars can be measured, but also in other galaxies, using integrated stellar light observations (Bressan et al. 1994; Henry & Worthey 1999) the same trend was discovered. If there is continuous infall of gas from the IGM to the disk, then higher metallicity stars will continue to form using the metal enriched ISM even at a later stage of evolution (Pagel & Patchett 1975; Tinsley 1980; Chiappini et al. 1997; Fenner & Gibson 2003; Chiappini 2009). This is the reason why the fraction of low metallicity stars formed using the pristine gas at the early phase will continuously decrease. Wakker et al. (1999) showed that an infall rate of 1 $M_\odot$ yr^{-1} integrated over the galactic disk can explain the so called G-dwarf problem of the Milky Way.

Hot and cold mode accretion : Recent smooth particle hydrodynamic simulations of galaxy formation have shown that the distribution of maximum attainable temperature of the accreted matter is clearly bimodal. Depending on the temperature, the mode of accretion is named as : i) 'hot mode accretion' where the gas gets accreted quasi-spherically and gets shock heated to the virial temperature of the halo ($T_{\text{vir}} \sim 10^6$ K for a Milky Way type galaxy) and ii) 'cold mode accretion' where the gas gets accreted through filament like structures and the maximum temperature of the accreted gas is less than 10^5 K. Apart from the hot and cold mode, the gas ejected from the galactic disk (i.e. galactic outflow, discussed in Sec 1.3.2) due to star forming activities can also cool down and fall into the galactic disk creating a galactic fountain.

The hot mode accretion was believed to be the only mode of accretion in the classical galaxy formation models developed in the late 1970s (Rees & Ostriker 1977; Silk 1977). Over the years these ideas have been updated through semi-analytical models and numerical simulations. Birnboim & Dekel (2003) and later Kereš et al. (2005) showed that the cold mode is the dominant mode of accretion in galaxies with halo mass less than $10^{11.4}\ M_{\odot}$. The dependence on halo mass also leads to redshift dependence. The cold mode is more dominant in galaxies at higher redshift and the hot mode is dominant in galaxies and clusters of galaxies at present. The existence of cold mode accretion in present day galaxies can potentially explain the observed diffuse X-ray emission from the galaxies which is well below the theoretical predictions by Benson et al. (2000). The gas accreted in cold mode gets heated only when it approaches the disk (and not near the virial radius as in hot mode) and $\approx 50\%$ of the gas (Fardal et al., 2001) cools down emitting cooling radiation in Lyman-α line (instead of X-ray, as in hot mode) which eventually gets absorbed by the disk gas.

The cooling time of the accreted gas depends on whether the gas is accreted in hot mode or cold mode. The cooling time scale is given by

$$t_{\text{cool}} \sim \frac{1.5nkT}{n^2\Lambda(T)} \tag{1.3}$$

where n is the density of the collapsed gas in the halo i.e. $n = 200\,\rho_c\,\Omega_b$, according to spherical collapse model. $\Lambda(T)$ is the radiative cooling function from Sutherland & Dopita (1993). For a Milky Way type galaxy the cooling time scale of the shock heated gas accreted in hot mode is ≈ 12.7 Gyr, close to the Hubble time. On the other hand, the cooling time of the gas in cold mode is ≈ 0.12 Gyr, very small compared to Hubble time. Hence the cold gas in the filaments cools down very fast and then condenses into the disk for further star formation, often giving rise to star burst episodes. The hot gas, however, cools down slowly and continuously replenish the gas in the galactic disk.

1.3.2 Interaction through gaseous outflow

The Λ-CDM Cosmology provides a remarkably good framework for the study of galaxy formation and evolution. However, there are a few observed properties of galaxies that cannot be explained by this theory, such as the observed galaxy luminosity function, the mass-metalicity relation and the regulated process of star formation in the galaxies.

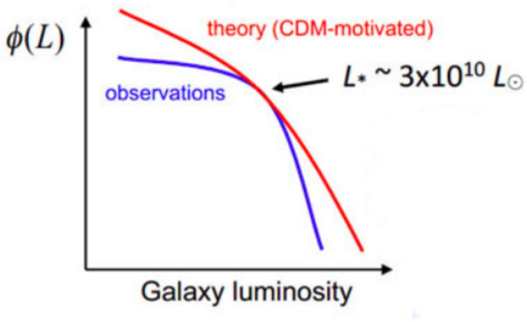

Figure 1.7: In the schematic diagram the red curve shows the halo mass function in terms of luminosity as predicted from ΛCDM cosmology model and the blue curve shows the observed galaxy luminosity relation.

- *Galaxy luminosity function :* The schematic diagram in Figure 1.7 shows that the observed galaxy luminosity function is flattened in the low mass end and steeper at the high mass end compared to what is predicted from the ΛCDM cosmology. It is believed that outflow from stellar feedback suppresses low mass galaxy formation by expelling gas out of the galaxies (Dekel & Silk 1986; Benson et al. 2003). This is the reason why the low mass (or luminosity) end of the observed curve is flattened. The steepening of the high mass end can be explained by AGN driven feedback from high mass galaxies (Benson et al. 2003; Bower et al. 2006; Vogelsberger et al. 2014b).

- *Mass-metallicity relation :* The gaseous outflow emanating from the inner region of the galaxies is enriched with metals. The metals are carried away by the outflowing gas to the CGM and even in the IGM. Massive galaxies have a higher ability to retain the ejecta compared to the low mass galaxies owing to their deeper gravtional potential well. This is the reason why the metallicity of galaxies increases with galaxy stellar mass (Davé et al., 2017). However, the mass metallicity relation gets flattened at the high mass end i.e. for galaxies with stellar mass $M_\star \gtrsim 10^{9.5}$ $M_\odot$ (Blanc et al., 2019). The metallicity gets saturated to a value when the ISM gas is depleted to the extent that the metallicty locked up in low mass stars and the metallicty ejected by the high mass stars becomes comparable (Tinsley 1980; Zahid et al. 2014).

- *Regulated star formation :* The empirical star formation law developed by Schmidt (1959) and Kennicutt (1989) established a correlation between the surface density of star formation rate ($\Sigma_{\rm SFR}$) and molecular gas ($\Sigma_{\rm g}$). The global Kennicutt-Schmidt (K-S) law ($\Sigma_{\rm SFR} \propto \Sigma_{\rm g}^s$, s being in the range 1-2) is consistent with observations when the quantities are averaged over $\sim$ 100 pc to few kpc. However, observations in local regions, typically less than 10 pc, with high densities (10^{2-4} cm^{-3}) suggest that the global K-S law is not applicable in small scale. Krumholz et al. (2012) pointed out that two regions with equal surface density can have very different volumetric density owing to the difference in their size and argued that a local volumetric star formation law can explain the observation in small scales. They estimated the star formation rate density as a ratio of gas density to the proper free fall time ($\rho_{\rm SFR} = \rho_g/t_{\rm ff}$) relevant for the star forming region. However, this is only comparable to the observed star formation rate if an efficiency factor $\epsilon_{\rm ff} \sim 0.01$ is considered or in other words, the star formation process appears to be suppressed. The suppression in star formation from the estimated value, in extreme case which is termed as 'galaxy quenching', can be explained by the ISM heating and gas expulsion by the galactic outflow.

1.3.3 Interaction through radiation from stars

Ionization by the radiation from stars : Radiation from the first stars and quasars (Venkatesan & Truran 2003; Johnson & Khochfar 2011) in the proto-galaxies played a pivotal role in reionizing the Universe. UV Photons with energy $E > 13.6$ eV emitted by the first sources ionized the neutral hydrogen in the surrounding medium. The HII regions surrounding the individual sources gradually merged together and by redshift of 6 the Universe was completely ionized, as has been inferred from the observation of Gunn-peterson trough in the spectra of high redshift ($z \gtrsim 6$) quasars .

As discussed in sec 1.1.2, proto-galaxies at high redshift were so small that even a single supernova could disrupt the entire galaxy and radiation and matter from the supernova remnant could have been ejected into the intergalactic medium. As time progressed, smaller dark matter halos merged together to form larger halos in which large spiral and elliptical galaxies formed. Most of the radiation in these galaxies were absorbed by the dense interstellar medium. Only a small fraction ($\sim 5\%$) of the UV light produced by the stars and supernova explosions could escape the galaxy. The escape fraction of the ionizing radiation increases in the presence of galactic outflow as it drives some of the gas from ISM and produce low density channels for the radiation to escape (Heckman et al., 2011).

Radiation pressure on ISM dust : In addition to this, stellar radiation can impart pressure on dust grains of the ISM and help in driving gaseous outflows in rapidly star-forming and starburst galaxies. The UV photons radiated by young and massive stars are absorbed and re-radiated by the dust grains as Infra-red (IR) photons. Since these dust particles are charged due to photo-ionization, they are coupled to the ISM gas through Coulomb interaction. Hence the momentum gained by the dust particles in this process is transferred to the ISM gas. In this way, ISM gas in the disk gains a momentum to drive the outflow.

For a gravitationally bound system, the theoretical upper limit of luminosity i.e. the classical Eddington luminosity is $L_{\rm Edd} = 4\pi G M_{enc} m_p c/\sigma_T$ where M_{enc} is the enclosed mass of the galaxy and σ_T is the Thompson cross-section. One can think of an Eddington like luminosity for radiation pressure on dust. Gas can be expelled out of the galaxy if the bolometric luminosity of the galaxy exceeds a limiting value. Considering the equilibrium between the momentum deposition rate of the radiation field to the inward pull of gravity, this limiting luminosity is given by $L_{\rm Edd,rad} = 4\pi GM(r)c/\kappa = \frac{8\pi c}{\kappa}\sigma^2 r$ where σ is the velocity dispersion of the halo (assuming the density profile to be that of an isothermal sphere) and κ is the mean opacity per unit mass of gas mixed with dust. For a MilkyWay-like galaxy, the star formation rate corresponding to the limiting luminosity is

$$\dot{m}_{\rm SF} = \frac{L_{\rm Edd,rad}}{\epsilon c^2} = 700 M_\odot\,{\rm yr}^{-1}\,(\sigma/200\,{\rm km\,s}^{-1})^2({\rm r}/10\,{\rm kpc})(\kappa/200\,{\rm cm}^2{\rm g}^{-1})^{-1} \tag{1.4}$$

with $\epsilon \sim 10^{-3}$ being the efficiency of energy production in nuclear fusion reactions and $\kappa \sim 200\,{\rm cm}^2\,{\rm g}^{-1}$ is the mean opacity in the U band for gas mixed with dust (Draine, 2011).

If the SFR is higher than this limiting value then radiation pressure alone can drive a galactic scale outflow. This is ~ 100 times higher than the present day Milky Way SFR ($2-3 M_\odot\,{\rm yr}^{-1}$), however such a star formation rate is common in starburst galaxies. For such a galaxy, Murray et al. (2005) showed that the radiation pressure on dust in the ISM can be equally powerful as the ram pressure to drive the cold gas clouds in the gaseous outflow. Sharma & Nath (2012) worked out the relative importance of ram pressure and radiation pressure and found that for high mass galaxies (rotation speed $v_c > 200$ kms^{-1}) and high SFR ($> 100\ M_\odot {\rm yr}^{-1}$) the radiation pressure becomes dominant over ram pressure in driving the galactic wind.

1.3.4 Interaction through cosmic rays

Cosmic ray (CR) or high energy particles constitute an intrinsic component of the interstellar medium (ISM). The CR energy density ($\sim 1\,{\rm eV\,cm}^{-3}$) in ISM is similar to those of thermal and magnetic field components. The existence of high energy particles coming from outer space was first established from balloon-borne experiments conducted by Victor Hess. He detected increasing number of charged particles with altitude with the help of an on-board electroscope and named this background radiation as 'cosmic radiation' (later known as cosmic rays) as he suspected the source of this radiation to be cosmic.

Composition and acceleration mechanism : Cosmic rays are charged elementary particles and nuclei with energies in the range $10^9 - 10^{20}$ eV. Almost 90 % of the cosmic ray population mostly comprises of protons with 9 % Helium nuclei and the rest 1 % is other heavier nuclei and leptons. It has been observed that cosmic ray spectrum follow a power law : $n(E) \propto E^{-p}$ where $p \approx 2.2 - 2.5$. The attempts to understand the origin and acceleration mechanism of these energetic particles has a long history. In 1949, Fermi (1949) suggested that particles can be accelerated by repeated reflections from ISM magnetic field in moving interstellar clouds. Bell (1978) showed that magnetic irregularities around a single supernova shock can accelerate the particles by reflecting them back and forth multiple times. However, by the diffusive shock acceleration mechanism a particle cannot be accelerated to arbitarily large energy. Cosmic ray protons with energy 10^{19} eV or larger have Larmor radius ($r_{\rm L} = E_{\rm PeV}/B_{\mu\rm G}$ parsec) comparable or greater than the size of the Galaxy ($\approx$ 10 kpc). The cosmic ray particles with energy greater than 10^{19} eV are considered to have an extra-galactic origin because, even if they are produced inside the Galaxy, it will be impossible to keep them bound to the Galaxy.

Cosmic ray pressure can drive galactic outflow : By a similar argument used for the radiation driven galactic wind one can think of an Eddington luminosity for cosmic rays by modifying the classical Eddington luminosity. In the classical case, the opacity is given by the Thompson scattering of radiation by free electrons. Similarly, in the case of cosmic rays the opacity is given by continuous scattering of the particles from magnetic irregularities, or in other words, 'diffusion' of cosmic rays. The CR diffusion timescale over a characteristic scale height $H \sim 1$ kpc in the leaky box model is $t_{diff,CR} \sim 10^7$ yr as inferred from the abundance ratio of ^{10}Be and ^{9}Be. The relative abundance of ^{10}Be, which is a radioactive isotope, is used to estimate the confinement time of CRs (Wiedenbeck & Greiner, 1980) within the characteristic scale height. Hence the characteristic cosmic ray mean free path $\lambda_{CR} \sim \frac{3H^2}{ct_{diff,CR}} \sim 10^{18}$ cm. On the other hand, assuming the density in Milky Way ISM to be $n \sim$1 particle cm^{-3}, the Thompson mean free path is $\lambda_T \sim 1/(n\, \sigma_{\rm T}) \sim 10^{24}$ cm, which is 6 orders of magnitude larger than the cosmic ray mean free path. Hence the CR Eddington luminosity is $L_{Edd,CR} = L_{Edd}\frac{\lambda_{CR}}{\lambda_T} = 10^{-6}L_{Edd}$. Assuming hydrostatic equilibrium between the CR pressure and inward pull of gravity (using the density profile of an isothermal sphere), one can obtain the required star formation rate to inhibit the inflow of gas. The limiting value of the SFR for a Milky Way like galaxy is

$$\dot{m}_{\rm SF} = 200 {\rm M_\odot yr^{-1}} (\tau_{\rm CR}/10^3)^{-1}(\epsilon/10^{-6})^{-1}({\rm f_g}/0.1)(\sigma/200{\rm km\,s^{-1}})^4 \tag{1.5}$$

where τ_{CR} is CR optical depth, f_g is the gas fraction and σ is the velocity dispersion of the halo. The SFR is much larger compared to the Milky Way SFR, but is quite common in starburst galaxies. Hence the CRs are potentially capable of driving large scale outflows in rapidly star forming galaxies. Socrates et al. (2008) showed that the momentum injection to the gas by the stellar radiation and cosmic rays are similar to that of supernova explosions (refer to section 1.3.3). The CRs, either being advected out of the galaxy with the outflowing gas or being diffused through the magnetic field can interact with the intergalactic medium in various ways. The next three chapters (chapters 2, 3 and 4) of the thesis will be devoted to discuss these interactions.

1.4 Implications on global 21 cm signal

The galaxy-IGM interaction has been justified by numerical simulations as well as observations as described in section 1.3.1 and 1.3.2, yet there is another observational probe which is relevant with repect to this thesis, which is the 21 cm signal from neutral hydrogen gas. The galaxy-IGM interaction can potentially change the IGM temperature and the imprints of these changes can be probed by a number of direct and indirect observations. Global 21 cm signal form the era when first stars formed is an important observable in this regard. The 21 cm radiation (frequency 1420 MHz) of neutral hydrogen arises due to the transition from the triplet to singlet hyperfine state of atomic Hydrogen. The hyperfine splitting of the energy levels arise due to the interaction between proton and electron spin. Though the transition has a very low value of Einstein A coefficient and as a result a very high lifetime in the triplet state (~ 10 Myr), this line is a powerful probe given the vast amount of hydrogen present in the intergalactic space. The intensity of 21 cm radiation is dependent on a parameter which is named the spin temperature, defined as:

$$\frac{n_1}{n_0} = 3\,exp(-T_\star/T_{\rm spin}) \tag{1.6}$$

where n_1 and n_0 are the number density of electrons in the triplet and singlet state and $T_\star$ is the temperature corresponding to the energy gap between the two hyperfine states. In terms of brightness temperature, which is the observable in the radio astronomy, the differential brightness temperature of the signal from the beginning of the epoch of reionization (Zaldarriaga et al., 2004) is given as

$$\Delta T_{21} \quad = \quad 28\,\text{mK}\,(1+\delta)x_{HI}\Big(1-\frac{T_{\rm CMB}}{T_{\rm spin}}\Big)\Big(\frac{\Omega_{\rm b}h^2}{0.0223}\Big)\sqrt{\Big(\frac{1+z}{10}\Big)\Big(\frac{0.24}{\Omega_{\rm m}}\Big)} \tag{1.7}$$

where x_{HI} is the neutral fraction of the hydrogen, δ is the over density, $\Omega_{\rm m}$ and $\Omega_{\rm b}$ are the mass and baryon density fraction of the critical density and $T_{\rm CMB}$ is the CMB temperature which acts as a background radiation.

The spin temperature is dependent on the gas temperature, CMB temperature and the Lyman alpha flux at a particular redshift. After the matter-radiation equilibrium era the radiation temperature or the CMB temperature falls as $(1+z)$ whereas the gas kinetic temperature falls as $(1+z)^2$ until the first objects formed. The spin temperature is coupled to the gas temperature at redshift $z > 100$ due to collisional coupling which occurred by the residual electrons from the era of recombination. At redshift $z \simeq 100$, the efficiency of collisional coupling decreases due to Hubble expansion and the spin temperature slowly becomes coupled to the CMB temperature. When the first objects formed around $z \sim 17-20$ the spin temperature again coupled to the gas temperature through Lyman-α coupling. At that point the CMB temperature was higher than the gas or spin temperature, hence we expect an absorption trough in the global 21 cm signal.

The depth of the absorption trough depends on the IGM gas temperature. Hence if the IGM temperature prior to reionization changes due to the interaction with the cosmic rays then the depth of the absorption trough will be different from what is expected from the standard Cosmological models. Again the presence of an exta background radiation apart from the CMB radiation can change the depth. Hence the predictions from the studies of interaction of galaxies and the IGM can be verified by the global 21 cm radiation from the beginning of the epoch of reionization.

1.5 Thesis Objectives

In the previous section it has been discussed that galaxies interact with their surrounding medium in numerous ways. The gravitational field of the galaxies help them to accrete matter from the intergalactic medium whereas the supernova and AGN activities stir up the interstellar medium by injecting mass, momentum and energy and eventually drive a large scale outflow of gas. These interactions between galaxies and their surroundings shape the course of galactic evolution. The interactions are mostly studied through simulations and observations of multiphase gas (i.e. gas at different temperature range) in the outskirts of the visible portion of galaxies, where the gas is supposedly influenced by galactic inflow and outflow. Apart from the thermal gas, interactions involving non-thermal component, like radiation and cosmic rays are also being investigated in the recent times.

1.5.1 Motivation of the thesis

More than 50 years ago Ginzburg & Ozernoi (1966) first pointed out that the cosmic rays accelerated in supernova explosions could raise the IGM temperature to $\sim 10^5$ K. They argued that low energy CRs lose a large fraction of their energy through Coulomb interactions while they diffuse through the IGM. Subsequently, numerous efforts have been made to understand the nature of this heating mechanism. Some of the related questions are as follows: Is the heating of IGM only concentrated around the galaxies? Or the cosmic rays diffuse throughout the IGM and increase the global IGM temperature? Do the IGM heating at very high redshift have any effect on the signature of 21 cm radiation coming from the high redshift Universe? Do cosmic rays also play a role in reionizing the Universe? These questions motivated us to study the non-uniform heating of the IGM, and calculate the temperature profile of IGM gas around high redshift galaxies depending on various parameters, such as the diffusion coefficient of CR.

Cosmic rays while diffusing through the IGM, not only interact with the gas but also with the IGM magnetic field. The cosmic ray electrons interacting with the IGM magnetic field emit synchrotron radiation and form a background radiation field. This excess background radiation at high redshift can change the signature of the redshifted global 21 cm signal from the epoch of reionization. The depth of the absorption trough in the first ever detected 21 cm signal from EOR (Bowman et al., 2018) by the EDGES group was, however, twice the expected depth from the $\Lambda - CDM$ cosmology. Several attempts have been made to explain this unexpected result by dark-mater baryonic interaction, the excess radio background and many other exotic physical processes. Instead of advocating any new physics, we were eager to know if the background radiation created by high redshift population III supernova explosions, which is an inevitable event, can explain the observation.

Focusing on the processes suffered by cosmic rays before they escape into the IGM, they get scattered multiple times and diffuse through the ISM and then CGM before coming out of the galaxy. During this process, the CRs get coupled with thermal gas and can potentially drive a bulk motion of the gas out of the galactic disk. The importance of CR driven galactic wind has being studied in the recent times, together with the thermal pressure driven wind. However, there remains many unanswered questions regarding the relative importance of different driving mechanisms of galactic scale outflows. The outflow simulations with time-dependent star formation rate (SFR coupled with the feedback) argue that CR driven winds are more efficient in suppressing the star formation rate of the galaxies by increasing the mass loading, compared to the thermal pressure driven winds. The simulations which accommodate intricate details of different physical processes make it complicated to understand the actual reason behind different simulation results. That was the motivation behind doing an *idealized* simulation of galactic outflows, in which different parameters could be changed independently of one another, in order to compare the dynamical impacts of thermal and CR driven galactic wind.

1.5.2 Structure of the thesis

The thesis is arranged as follows :

- **Chapter 2:** The second chapter of the thesis attempts to understand how CR heating is distributed throughout the IGM with the help of a simple analytical model. Considering diffusion as the main transport mechanism of the particles, we calculate both the spatial and temporal temperature profile around galaxies at different redshift. Depending on the star formation rate and the redshift of the galaxies, the surrounding medium may be ionized or neutral. We determined the temperature profiles for both these cases. Since there is an uncertainty regarding the high redshift IGM magnetic field, we considered the diffusion coefficient as a free parameter and estimated the upper limit on the diffusion coefficient below which the heating would be inhomogeneous or patchy around the galaxies. We also find that CR heating of IGM around galaxies can suppress the infall of gas in the galaxies in certain cases, which can have important implications for galactic evolution.

- **Chapter 3:** The third chapter of the thesis aims at studying the effect of excess radio background at high redshift on the 21 cm global signal. We have not only studied the effect of synchrotron emission by the CR electrons, but also the effect of CR heating. There are admittedly some uncertainties regarding the magnitude of high redshift IGM magnetic field and the magnetic field amplification near astrophysical shocks. There are also uncertainties regarding the energy output of high redshift Pop III supernovae. We have taken into account these uncertainties in terms of a few parameters and did a detailed study in the whole parameter space. The calculation revealed that although the background radiation alone can explain the observed trough in the 21 cm signal, the combined effect of background radiation *and* CR heating do not allow the 21 cm absorption trough to be greater than ~ 0.25 K.

- **Chapter 4:** The purpose of the fourth chapter of the thesis is to understand the role of cosmic rays in driving galactic outflows in the early stages of evolution. We performed two sets of idealized hydrodynamic simulations, one in which the outflow is purely thermally driven, and another, in which the outflow is driven by both thermal and CR pressure. We assumed isotropic diffusion to be the leading transport mechanism. With the simulation of three galaxy masses ($10^8, 10^{11}$ and $10^{12} M_\odot$) and using three different star formation rates for each galaxy types, we concluded that the dynamical impact of cosmic rays on the galactic outflow is not important. We also infer that cosmic ray diffusion may eventually inhibit cold clump formation if we run the simulation for a long enough time with periodic star formation rate. As a result, the feedback efficiency of CR driven galactic wind increases which manifests itself with an increase in mass loading and decrease in star formation. This idealized simulation can potentially solve the discrepancy in results between the simulations with time-independent and time-dependent star formation rate.

2

Cosmic Ray Heating of Intergalactic Medium

We study the heating of the intergalactic medium (IGM) surrounding high redshift star forming galaxies due to cosmic rays (CR). We take into account the diffusion of cosmic rays and study the inhomogeneity in the resulting temperature of the IGM. We discuss the case of IGM heating around a high redshift minihalo ($z \sim 10$–20, $M \sim 10^5$–10^7 $M_\odot$). We also discuss two other cases with continuous star formation, one in which the star formation rate (SFR) of a galaxy is large enough to make the IGM in the vicinity photo-ionized, and another in which the SFR is low enough to keep it neutral but high enough to cause significant heating by cosmic ray protons.

Key results :

- We put an upper limit on the diffusion coefficient $D \leq 1 \times 10^{26}$ cm^2 s^{-1} for the heating to be inhomogeneous at $z \sim 10$ and $D \leq 5$–6×10^{26} cm^2 s^{-1} at $z \sim 20$.
- For typical values of D, our results suggest uniform heating by CR at high redshift, although there are uncertainties in magnetic field and other CR parameters.
- For the case of continuous (low) SFR and neutral IGM, we find that the heating can make the gas hotter than the cosmic microwave background (CMB) radiation for $D < 10^{30}$ cm^2 s^{-1}, within a few kpc of the galaxy, and unlikely to be probed by near future radio observations.
- For the case of continuous (high) SFR and photo-ionized IGM, the heating of the gas in the vicinity of high redshift ($z \sim 4$) galaxies of mass $\geq 10^{12}$ M$_\odot$ can suppress gas infall into the galaxy. At lower redshifts ($z \sim 0$), an SFR of ~ 1 M$_\odot$ yr^{-1} can suppress the infall into galaxies of mass $\leq 10^{10}$ M$_\odot$.

Based on:

"Cosmic ray heating of intergalactic medium: patchy or uniform?" by **Ranita Jana**, Biman B. Nath, *MNRAS*, *479*(1), 153-161, (Jana and Nath 2018)

2.1 Introduction

Galaxies interact with the surrounding gas in various ways, through gravitational and mechanical means, as well as through radiation. The gravitational field of collapsed structures help them to accrete matter from surrounding regions, setting up an inflow of gas and dark matter. The radiation emanating from stars and possible active galactic nuclei (AGN) also affect the intergalactic medium (IGM), by ionizing and heating. The process of star formation and AGN activities stir up the interstellar medium (ISM) of the galaxies, often setting up galactic outflows which interact with the IGM gas through fluid dynamical interactions. There is yet another type of interaction that has been discussed in the literature, through high energy particles, which may be produced during the star formation or AGN activity in galaxies.

Ginzburg & Ozernoi (1966) pointed out that cosmic rays (CR) accelerated in supernovae (SNe) and radio galaxies could raise the temperature of the IGM gas to $\geq 10^5$ K. Their argument was based on the fact that low energy CRs lose a large fraction of their energy through Coulomb interactions. Nath & Biermann (1993) addressed the question of possible reionization of the Universe through such processes, and concluded that it would require a very large star formation rate (SFR) density. According to Lacki (2015), CRs would contribute towards a significant non-thermal pressure of the IGM gas. Another possible effect of CRs in the IGM discussed in the literature is the production of ^6Li by CR α particles. Nath et al. (2006) showed the observed abundance ratio of $^6Li/H$ can be related to the observed entropy of the intracluster medium, through Coulomb heating.

Recently, Sazonov & Sunyaev (2015) suggested that low energy CRs (with kinetic energy $\leq$ 30 MeV per nucleon) could have heated the neutral IGM at high redshift and change the HI emission characteristics of the gas. Such a feature can be potentially detected in planned experiments that will detect redshifted 21 cm emission. Following this argument, Leite et al. (2017) calculated in detail the heating of the IGM by CRs, and found that the IGM temperature could have been increased by $\Delta T \sim 100$ K at $z \sim 10$.

However, as Leite et al. (2017) and others have pointed out, the propagation of the CRs crucially depend on the diffusion coefficient. Diffusion of CRs can heat the surrounding gas in a non-uniform manner. In this chapter, we discuss the heating of intergalactic medium by CRs produced by star forming galaxies, as a function of diffusion coefficient,gas density, SFR and other relevant parameters, and discuss the implication of this kind of heating.

2.2 Preliminaries

We consider the heating effect of CR protons in this chapter on the IGM gas surrounding a galaxy. The energy deposition by protons depends on several parameters, and below we list our assumptions regarding them.

2.2.1 CR spectrum

The CR luminosity of a galaxy is determined by its SFR, assuming a Salpeter IMF (with 0.1 $M_\odot$ and 30 $M_\odot$ as the lower and upper limits), with a total mechanical energy output of 10^{51} erg per SNe and an efficiency of η for CR acceleration. There is a significant uncertainty in this parameter (from less than 0.1 to ~ 0.5). We assume a value of $\eta = 0.1$, which is supported by the simulation results of Caprioli & Spitkovsky (2014). This gives us,

$$L_{\rm cr} = 2 \times 10^{40}\,{\rm erg\,s^{-1}} \left(\frac{\eta}{0.1}\right) \left(\frac{\rm SFR}{1\,{\rm M_\odot\,yr^{-1}}}\right). \tag{2.1}$$

We assume that the CR protons leave the galactic virial radius R_{vir}, with a spectrum $n_{cr}(p_0) \propto p_0^{\alpha}$, where $p_0(\equiv p(r = R_{vir}))$ denotes the momentum of protons as they leave the galaxy at $r = R_{vir}$, and $n_{cr}(p_0)$ is the rate of CRs (number of CR per second) coming out of the galaxy with momentum p_0. In our calculation, we assume $\alpha = -2.5$, and discuss the effect of changing its value later in this chapter.

The spectrum is normalized such that the total energy flux corresponds to the above mentioned CR luminosity, or,

$$L_{cr} = \int_{p_{0,min}}^{p_{0,max}} E_k n_{cr}(p_0) dp_0\,, \tag{2.2}$$

where $p_{0,min}$ and $p_{0,max}$ are the lower and upper limits of CR momenta, with kinetic energy $E_k = \sqrt{p^2c^2 + m_p^2c^4} - m_pc^2$. By denoting $x_0 = p_0/(m_pc)$, CR spectrum can be written (in terms of number of particles per unit time) as,

$$n_{cr}(p_0)dp_0 = \left(\frac{L_{\rm cr}}{(m_pc^2)(m_pc)^{\alpha+1}\int[\sqrt{1+x_0^2}-1]x_0^{\alpha}dx_0}\right)p_0^{\alpha}dp_0\,, \tag{2.3}$$

where the integration is carried out between $x_{0,min} = \frac{p_{0,min}}{m_pc}$ and $x_{0,max} = \frac{p_{0,max}}{m_pc}$. We will find it more convenient to describe the spectrum in terms of $\beta(\equiv v/c)$, and in the rest of the chapter, we will write the emergent spectrum from the galaxy in equation 2.3 as $n_{cr}(\beta_0)d\beta_0$, where $p_0 = \frac{m_p\beta_0 c}{\sqrt{1-\beta_0^2}}$.

The heating effect of CRs is insensitive to the upper limit of energy, but depends strongly on the lower limit, since the energy loss rate increases with decreasing CR energy. Previous works by Sazonov & Sunyaev (2015) and Leite et al. (2017) considered heating by protons of $\leq$ 10–30 MeV. However, protons with very low energy, with ≤ 1 MeV, are unlikely to survive the interactions with the interstellar medium (ISM) of the parent galaxy for the following reasons. The loss of (kinetic) energy by a proton through interaction with ionized gas of electron density n_e cm^{-3} and temperature T_e K is given by (Mannheim & Schlickeiser, 1994) (their equation 4.22)

$$-\frac{dE_k}{dt} \approx 5 \times 10^{-19}\,\frac{\rm erg}{\rm s}\left(\frac{n_e}{\rm cm^{-3}}\right)\frac{\beta^2}{x_m^3 + \beta^3}\,, \tag{2.4}$$

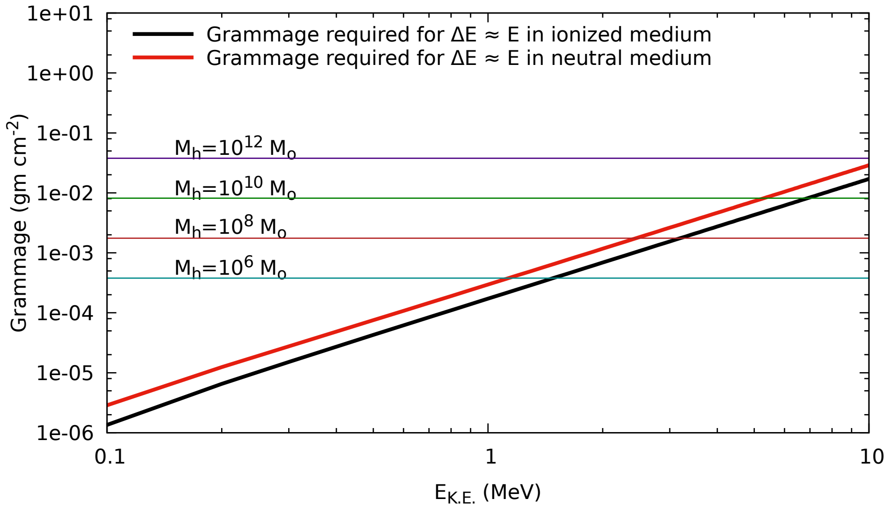

Figure 2.1: Grammage to deplete the total energy of a proton is shown against the proton kinetic energy for ionized and neutral media. Corresponding line-of-sight grammages for galaxies with $\mathrm{M_h} = 10^6, 10^8, 10^{10}, 10^{12}\ \mathrm{M_\odot}$ are shown for $z = 10$.

where $x_m = 0.0286(T_e/2\times10^6\ \mathrm{K})^{1/2}$.

For a CR proton in a neutral medium with particle density n_{HI}, the energy loss rate is given by equation (4.32) of Mannheim & Schlickeiser (1994),

$$-\Big(\frac{dE_k}{dt}\Big) = 3\times10^{-19}\,\frac{\mathrm{erg}}{\mathrm{s}}\Big(\frac{n_{\mathrm{HI}}}{cm^{-3}}\Big) \times(1+0.0185\,\ln\beta\,H[\beta-\beta_c])\frac{2\beta^2}{\beta_c^3+2\beta^3}\,, \tag{2.5}$$

where $\beta_c \approx 0.01$, corresponding to the orbital speed of electrons in a hydrogen atom. For analytical simplicity we neglect the term $(1+0.0185\,\ln\beta\,H[\beta-\beta_c])$ in the above expression, since it does not significantly affect the result.

This can be used to estimate the grammage ($\int n_e m_p \beta c dt$) required to drain a proton of its kinetic energy (when $E_k \approx dE_k$). We show this value of grammage as a function of proton kinetic energy in Figure 2.1. We also superimpose several relevant values of line-of-sight grammage as horizontal lines, corresponding to different galaxy masses at redshift 10, estimated as $\frac{M_h f_b}{R_{vir}(z)^2}$, where M_h is the total halo mass of a galaxy, $f_b \approx 0.15$ is the cosmic baryon fraction and $R_{vir}(z)$ is the virial radius at redshift z.

The curves in the figure show that protons of energy less than 0.1–1 MeV are likely to lose all their energy if they were to travel through the ISM of the parent galaxy in a straight path. Therefore, this value should indicate the lower limit of energy, E_{min}, corresponding to the lower limit of momentum $p_{0,min}$ mentioned above.

However, there are two possibilities that can change the lower limit. CRs may *diffuse* through the ISM and the corresponding grammage is likely to be much higher than depicted as horizontal lines here. For example, in the case of Milky Way, the inferred grammage of ~ 10 g cm^{-2} is much larger than the total column density of the disk, and the corresponding $E_{\rm min} \sim 50$ MeV, where a break in CR spectrum is expected and is indeed observed (Nath et al., 2012).

On the other hand, CRs in star forming galaxies may be *advected* by gas in the ensuing galactic outflow. In this case, the lower limit of energy may decrease because of adiabatic loss. Since the adiabatic loss of CR energy scales as $\Delta E \propto R^{-1}$, the factor by which the lower limit of energy will decrease is $\epsilon_{\rm adv}$ roughly the ratio of the size of a galaxy halo and the region of CR production, *i.e.*, the disk of a star forming galaxy (Nath & Biermann, 1993). This ratio is roughly of order ~ 0.1, and we adopt this value for $\epsilon_{\rm adv}$.

Therefore, we assume two values of the lower limit of energy, 0.1 and 1 MeV to encapsulate the uncertainties in the processes of CR propagation until it reaches the IGM.

2.2.2 CR diffusion

For heating of the gas in which CRs propagate, it is the low energy CRs that play an important role, since the amount of energy lost by a CR increases with decreasing energy. In our context, the energy range of interest is ≤ 100 MeV, as has been pointed out by previous workers (Sazonov & Sunyaev, 2015; Leite et al., 2017).

The diffusion coefficient of CRs is believed to depend on energy, and this dependence in the Milky Way is estimated from a comparison of the observed CR spectrum with what is believed to be the source spectrum. There is, however, considerable uncertainty in the interpretation. Phenomenologically, a few prescriptions for the diffusion coefficient are used in the literature and in models such as GALPROP (see, eg, Ptuskin (2012)). In the 'plain diffusion model', the diffusion coefficient for low energy cosmic rays is thought to be, $D = 2.2 \times 10^{28} \beta^{-2}$ cm^2/s. As has been pointed out by Ptuskin (2012), the increase in the diffusion coefficient with decreasing energy has no physical explanation and is purely a phenomenological inference. The other common model of diffusion coefficient is that of 'distributed reacceleration', which scales as $p^{1/3}$, and therefore decreases with decreasing energy (see Figure 1 of Ptuskin et al. (2006)). Therefore, it is not clear from phenomenological studies if the diffusion coefficient should increase or decrease with decreasing energy at low energies. For simplicity we assume the diffusion coefficient to be constant for low energy CR protons.

The diffusion coefficient also depends on the magnetic field, because the diffusion of CRs depend on particle scattering by magnetohydrodynamic (MHD) waves and irregularities. For Kolmogorov-type spectrum of turbulence, the diffusion coefficient for scattering of protons off magnetic irregularities scales as $D \propto r_g^{2-5/3} \propto B^{-1/3}$, where r_g is the gyroradius (Ptuskin, 2012).

In light of the above discussion, we assume the diffusion coefficient of low energy CRs to be constant, to be 2×10^{28} cm^2 s^{-1}, for a 5μG magnetic field in the Milky Way ISM. The present day IGM magnetic field strength is estimated to be of order $\sim 10^{-9}$ G (Subramanian, 2016). Using the expected scaling of $D \propto B^{-1/3}$ for Kolmogorov spectrum of magnetic irreguarities, we estimate the diffusion coefficient at present epoch to be $D \sim 3 \times 10^{29}$ cm^2 s^{-1}. The magnetic field strength scales with redshift as $B \propto (1+z)^2$ since the magnetic energy density scales as $(1+z)^4$. This implies a value of the diffusion coefficient at $z \sim 10$ to be $D \sim 10^{29}$ cm^2 s^{-1}. We use this as the fiducial value in our calculation for heating of the IGM gas at high redshift ($z \sim 10$–20). However, we discuss the effect of changing the diffusion coefficient on our results.

2.2.3 Physical property of IGM near the galaxy

We assume for simplicity a static and uniform density gas around the galaxy, with number density $n_{\rm IGM}$ cm^{-3}. The IGM density near a galaxy is likely to be larger than the critical matter density, and we assume that it is a factor $\Delta \approx 10$ times the critical density at a given epoch. In other words,

$$\begin{aligned} \rho_{\rm IGM}(z) &= 10 \times f_b \rho_{cr} \Omega_m(z) \\ &= 5.6 \times 10^{-27}\,{\rm cm}^{-3} \left(\frac{\Delta}{10}\right)\left(\frac{1+z}{11}\right)^3 . \end{aligned} \tag{2.6}$$

The cosmological parameters used are determined by Planck Collaboration et al. (2014). Therefore our assumed number density of gas ($n_{\rm IGM} = \frac{\rho_{\rm IGM}}{\mu m_p}$) is 2.8×10^{-3}cm^{-3} in neutral medium ($\mu = 1.2$) and 5.6×10^{-3}cm^{-3} in ionized medium ($\mu = 0.6$) at redshift 10 whereas the number density of electron is 2.9×10^{-3}cm^{-3} since $\mu_e = 1.14$.

We shall justify our assumption in §4.3 by showing that a uniform density with $\Delta = 10$ approximately gives the same results as in the case of a density profile that is more realistic outside the halo, within the relevant distance.

The IGM near a galaxy is also likely to be photoionized, owing to the ionizing radiation from massive stars, even before the first SNe begin to produce CR. This can be demonstrated by estimating the Strömgren sphere radius for different values of SFR and Δ. Using STARBURST99 we find that for a continuous star formation scenario, the number of ionizing photons radiated per second is $\approx 2 \times 10^{54}({\rm SFR}/10\,{\rm M}_\odot\,{\rm yr}^{-1})$ at 10 Myr after the onset of star formation. This gives a Strömgren sphere radius as,

$$\begin{aligned} R_s &\approx 193.8\ {\rm kpc} \left(\frac{\rm SFR}{10\,{\rm M}_\odot\,{\rm yr}^{-1}}\right)^{1/3} \left(\frac{\Delta}{10}\right)^{-2/3} \left(\frac{f_b}{0.157}\right)^{-2/3} \\ &\quad \times \left(\frac{h}{0.677}\right)^{-4/3} \left(\frac{\Omega_{m,0}}{0.309}\right)^{-2/3} \left(\frac{1+z}{11}\right)^{-2} \end{aligned} \tag{2.7}$$

For $z = 10$, the corresponding radius is ~ 194 kpc $({\rm SFR}/10\,{\rm M}_\odot\,{\rm yr}^{-1})^{1/3}$. This length scale is much larger than the diffusion length of CR particles with $D \sim 10^{29}$ cm^2 s^{-1}, for a time scale of 100 Myr, the typical duration of a burst of star formation. In other words, the heating effect of CRs is limited to an ionized region, for galaxies with SFR ~ 10 M$_\odot$ yr^{-1}. For a smaller SFR, one may have to consider a neutral IGM.

In order to ascertain whether or not the IGM in the vicinity of the galaxy is neutral or ionized, the size of the ionized region can also be compared with the virial radius of a

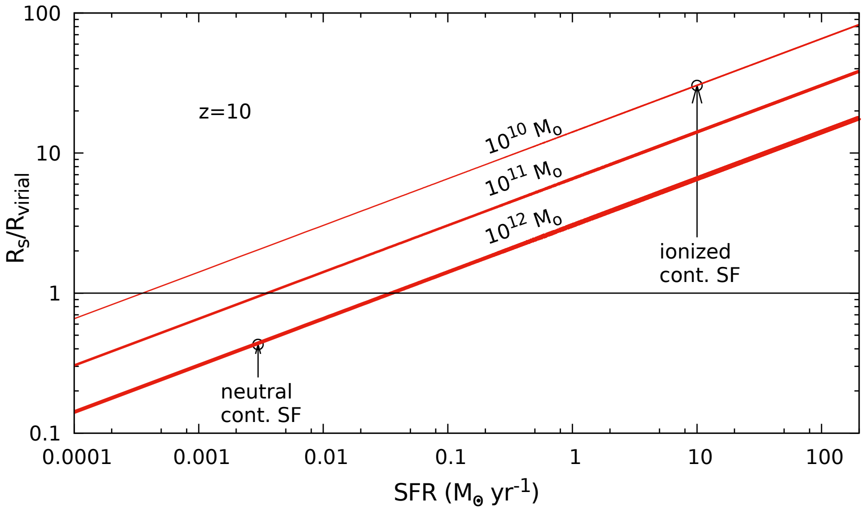

Figure 2.2: Ratio of Strömgren Sphere radii and virial radii of galaxies of $M_h = 10^{10}, 10^{11}, 10^{12}$ $M_\odot$ are shown as a function of SFR at $z = 10$. Arrow marks show the fiducial SFR chosen for the cases of neutral and ionized IGM.

galaxy. We plot in Figure 2.2 the ratio of Strömgren radius to virial radius, as a function of SFR, for three different galaxy masses $M_h = 10^{10}, 10^{11}, 10^{12}$ $M_\odot$ at $z = 10$. The lower half region of the figure, with $R_s/R_{\rm vir} \leq 1$ refers to the case of neutral IGM gas in the vicinity of a galaxy. For example, for a galaxy with mass $M_h = 10^{10}$ $M_\odot$ at $z = 10$, SFR has to be $\leq 10^{-3}$ $M_\odot$ yr^{-1} for the gas to be neutral.

Therefore we consider two cases, one in which the surrounding gas is neutral and another in which it is photoionized. In the neutral case, we assume the gas temperature to be $T = 2.73 \times 151 \times [(1+z)/151]^2 = 2.19[(1+z)/11]^2$ K, since the matter and radiation temperature decouples at $z \sim 150$ and matter temperature drops as $(1+z)^{-2}$ afterwards. In the photoionized case, we assume the gas to be at a temperature 10^4 K, appropriate for a photoionzed gas with primordial abundance.

In addition, we consider a third case, of that of a primordial supernova in a high redshift minihalo ($z = 10$–20, $M_h = 10^5$–10^7 $M_\odot$), which was discussed by Sazonov & Sunyaev (2015).

Gas cooling

In the case of a photoionized IGM with primordial composition, we use the cooling due to bremsstrahlung and recombination cooling (Efstathiou, 1992), using the rates given in Appendix A by Hui & Gnedin (1997).

For the case of neutral gas, the resulting temperature is small ($\leq$ 1000 K) and the cooling time exceeds the Hubble time. Therefore gas cooling can be neglected in this case.

2.3 Evolution of CR spectrum

The calculation of the evolution of CR spectrum and resulting heating of the gas is described below for two different cases.

2.3.1 Neutral IGM

In case of neutral medium, we write 2.5 in terms of β of the proton,

$$-\frac{d\beta}{dt} = 3.9 \times 10^{-16} \Big(\frac{n_{\rm HI}}{cm^{-3}}\Big) \frac{\beta(1-\beta^2)^{\frac{3}{2}}}{\beta_c^3 + 2\beta^3} \tag{2.8}$$

Furthermore, for a proton with diffusion coefficient D, the rms speed is given by

$$\frac{dr}{dt} = \frac{3D}{r} \, . \tag{2.9}$$

Combining these two equations, we have,

$$\frac{d\beta}{dr_{\rm kpc}} = 1.2 \times 10^{-2} \frac{(n_{\rm HI}/{\rm cm}^{-3}) \, r_{kpc}}{(D/10^{29}{\rm cm}^2 \, {\rm s}^{-1})} \frac{\beta(1-\beta^2)^{\frac{3}{2}}}{\beta_c^3 + 2\beta^3} \, , \tag{2.10}$$

where $r_{\rm kpc}$ is the distance from the virial radius of the galaxy in kpc unit. This equation can be analytically solved to give β as a function of r given an initial value β_0. This is given by,

$$\begin{aligned}
&\tan(\arcsin\beta) - (\arcsin\beta) + (\beta_c^3/2) \ln\tan\Big(\frac{\arcsin\beta}{2}\Big) + \\
&\frac{(\beta_c^3/2)}{\cos(\arcsin\beta)} \\
&= \tan(\arcsin\beta_0) - (\arcsin\beta_0) + (\beta_c^3/2) \ln\tan\Big(\frac{\arcsin\beta_0}{2}\Big) \\
&+ \frac{\beta_c^3/2}{\cos(\arcsin\beta_0)} - \frac{3.1 \times 10^{-3} (n_{\rm HI}/{\rm cm}^{-3}) \, r_{\rm kpc}^2}{(D/10^{29} \, {\rm cm}^2 \, {\rm s}^{-1})} \, .
\end{aligned} \tag{2.11}$$

This relation can be used to trace the evolution of the CR spectrum as a function of distance r, given a density of the medium.

A useful parameter to define in this context is the distance through which the minimum energy CR proton loses all its energy, which is calculated from equation 2.11, by using a value of β_0 corresponding to $E_{0,min}$. This distance scale will be important in describing the results of temperature profile later in this chapter. We have found that this length scale r_0 can be approximately determined by,

$$r_0 \approx 0.1 \, {\rm kpc} \Big(\frac{E_{0,min}}{1 \, {\rm MeV}}\Big)^{0.73} \Big(\frac{n_{\rm HI}}{1 \, {\rm cm}^{-3}}\Big)^{-0.54} \Big(\frac{D}{10^{29}{\rm cm}^2{\rm s}^{-1}}\Big)^{\frac{1}{2}} \tag{2.12}$$

In the case of $z = 10$ and $\Delta = 10$, the corresponding particle density is $n_{\rm HI} \approx 0.003 \, {\rm cm}^{-3}$, and a 1 MeV proton loses all its energy within a distance ≈ 2.2 kpc from the virial radius. We will refer to these values when we discuss the effect of IGM heating.

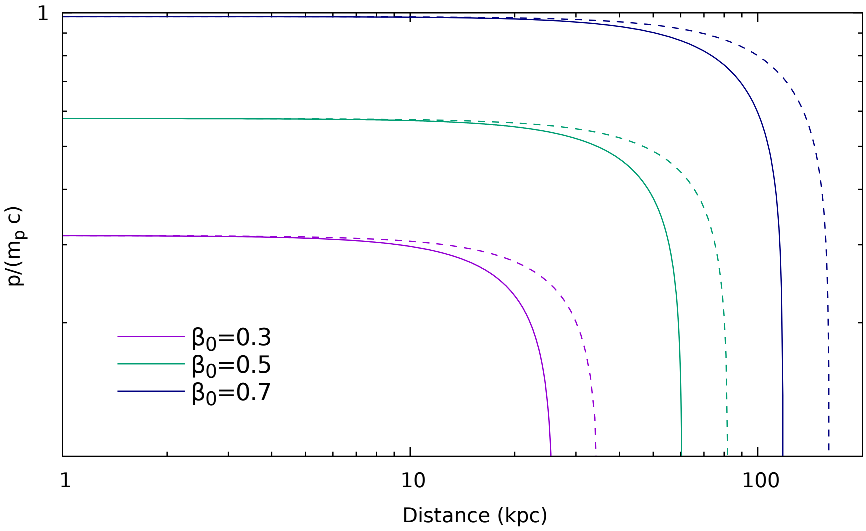

Figure 2.3: Change in the dimensionless momentum $p/(m_p c)$ of a proton with distance for different initial values of p (whose corresponding β_0 values are shown as labels), for $z = 10$ and $\Delta = 10$. Solid lines show the case of ionized IGM and dashed lines show the case of neutral IGM.

2.3.2 Photoionized IGM

In the case of photoionized gas, we can write equation 2.4 in terms of β, as,

$$-\frac{d\beta}{dt} = 3.3 \times 10^{-16}\,\mathrm{s}^{-1} \left(\frac{n_e}{\mathrm{cm}^{-3}}\right) \frac{\beta(1-\beta^2)^{\frac{3}{2}}}{\beta^3 + x_m^3} \,. \tag{2.13}$$

For analytical simplicity, we assume x_m to be a constant and fix its value appropriate for $T = 10^4$ K. As in the case of neutral medium, we have for the evolution of β with distance,

$$-\frac{d\beta}{dr_{\mathrm{kpc}}} = 0.01 \times \frac{(n_e/\mathrm{cm}^{-3})\, r_{\mathrm{kpc}}}{(D/10^{29}\,\mathrm{cm}^2\,\mathrm{s}^{-1})} \frac{\beta(1-\beta^2)^{\frac{3}{2}}}{\beta^3 + x_m^3} \,. \tag{2.14}$$

The resulting relation between β and r for a given β_0 is given by,

$$\begin{aligned} &\tan(\arcsin\beta) - (\arcsin\beta) + x_m^3 \ln\tan\left(\frac{\arcsin\beta}{2}\right) + \\ &\quad \frac{x_m^3}{\cos(\arcsin\beta)} \\ &= \tan(\arcsin\beta_0) - (\arcsin\beta_0) + x_m^3 \ln\tan\left(\frac{\arcsin\beta_0}{2}\right) \\ &+ \frac{x_m^3}{\cos(\arcsin\beta_0)} - 5\times 10^{-3} \frac{(n_e/\mathrm{cm}^{-3})\, r_{\mathrm{kpc}}^2}{(D/10^{29}\,\mathrm{cm}^2\,\mathrm{s}^{-1})} \,. \end{aligned} \tag{2.15}$$

The corresponding change in momentum as a function of distance is shown in Figure 2.3 for the case of $\Delta = 10$ and $z = 10$.

2.3.3 Change in spectrum

The loss of energy in protons changes the CR proton spectrum as they diffuse outwards from the virial radius of the parent galaxy. The CR proton spectrum at a given distance r is

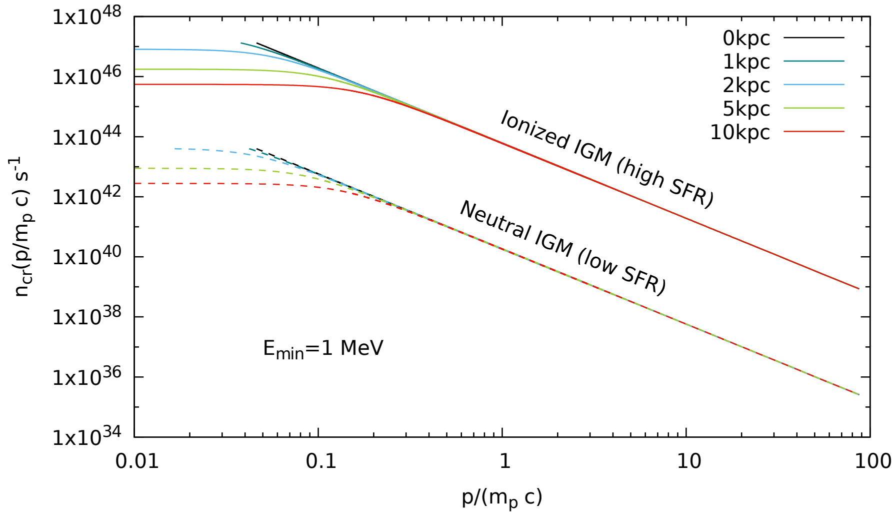

Figure 2.4: The spectrum of CR protons is shown at different distances by solid lines for ionized (z = 10 and SFR = $10\mathrm{M}_\odot$/yr) and by dashed lines for neutral (z = 10 and SFR = $0.003\mathrm{M}_\odot$/yr) medium. Both curves assume $\Delta = 10$.

calculated by using $n_{cr}(\beta(r))d\beta = n_{cr}(\beta_0)d\beta_0$, which follows from the conservation of the number of CRs. In order to evaluate it, we use the relation between β, β_0, r from equation 2.11 and 2.15. Note that $n_{cr}(\beta)$ is related to the SFR according to the normalisation equation 2.1 and has dimensions of time^{-1}.

We show in Figure 2.4 two examples of how the CR spectrum changes at different distances from the galaxy, for the case of SFR=10 $\mathrm{M}_\odot$ yr^{-1}, ionized IGM, (solid curves), and SFR=0.003 $\mathrm{M}_\odot$ yr^{-1}, neutral IGM, (dashed curves) both at z = 10 and assuming $\Delta = 10$. As expected, we find that more and more low energy CR protons are depleted as they diffuse outward.

2.4 Gas heating

In the case of ionized IGM, the total energy lost by CR protons goes into heating the IGM gas. However, in the case of neutral IGM, only a fraction $f_{\rm heat}$ of the energy lost by protons is used for the heating of the IGM gas, and the rest is spent in partially ionizing the neutral gas and excitation of neutral atoms.

This fraction depends not only on the CR proton energy but also on secondary ionization process (by the ejected electrons). Effectively, it depends on the fractional ionization x_e of the gas. As discussed in Sazonov & Sunyaev (2015), this fraction $f_{\rm heat} \sim 0.25$ for $x_e \sim 0.01$. As a conservative estimate, we use a fraction of $f_{\rm heat} = 0.25$ for the case of neutral IGM and $f_{\rm heat} = 1$ for ionized IGM in our calculations. The rate of increase of energy density ϵ in a spherical shell of IGM gas at distance r and width Δr due to interaction of ionized gas with a CR proton of velocity βc for a time interval of Δt can be

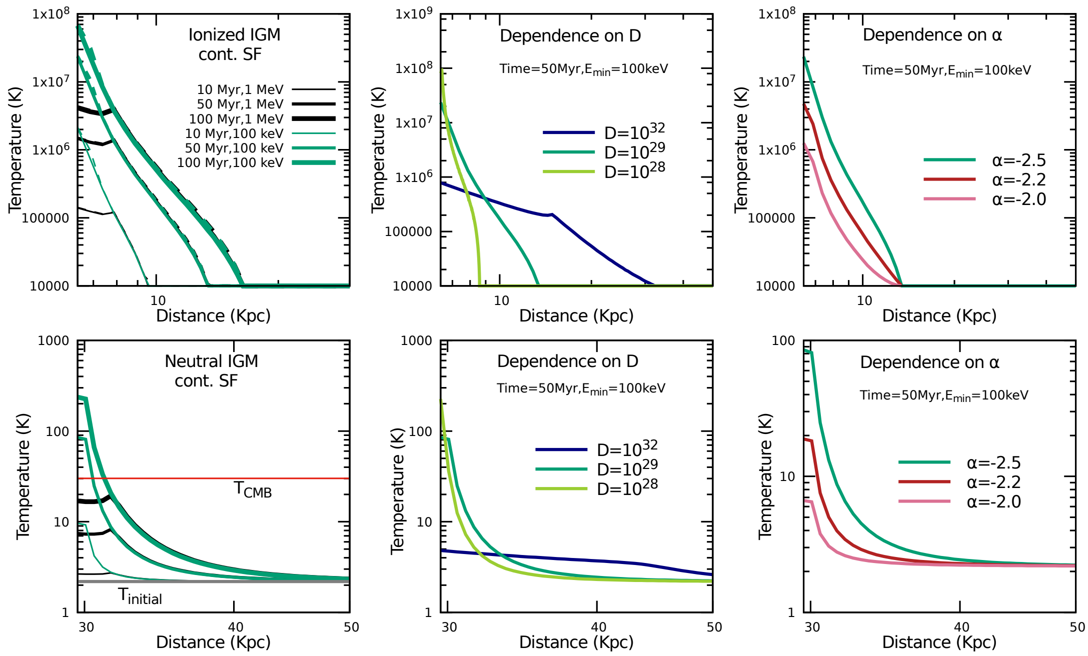

Figure 2.5: The temperature profile for SFR=10M$_\odot$/yr, M$_\mathrm{h}$ = 10^{10}M$_\odot$ (upper panel) and SFR=0.003M$_\odot$/yr, M$_\mathrm{h}$ = 10^{12}M$_\odot$ (lower panel) is shown for 10, 50, 100 Myr at $z = 10$ using $D = 10^{29}\mathrm{cm^2s^{-1}}$ and $\Delta = 10$. The left panels shows the case of heating of photoionized gas (upper left) and neutral IGM gas (lower left). Dashed lines show the profiles without cooling and solid lines show the profiles with cooling. In the lower panels, the horizontal red line corresponds to the CMB temperature. The middle panels show the variation of the result with diffusion coefficient and the right panels show the variation with CR spectral index α.

written as,

$$\frac{d\epsilon}{dt} = f_\mathrm{heat}\,\frac{dE(\beta)}{dt}\,\frac{1}{4\pi r^2 \Delta r}\,\Delta t\,. \tag{2.16}$$

Here Δt is the residence time of a proton in this particular shell during its outward diffusion. We write this as,

$$\frac{d\epsilon}{dt} = f_\mathrm{heat}\,\frac{dE(\beta)}{dt}\,\frac{1}{4\pi r^2 \frac{dr}{dt}}\,H[t - r^2/(6D)]\,, \tag{2.17}$$

where $\frac{dr}{dt}$ refers to the diffusion equation 2.9, and the Heavyside step function uses the arrival time ($= r^2/(6D)$) of protons at the particular shell at distance r. For an ensemble of CR protons, we integrate this over the CR spectrum at this shell, $n_{cr}(\beta)d\beta$. We finally arrive at,

$$\begin{aligned}\frac{d\epsilon}{dt} &= 5\times 10^{-19}\,\frac{\mathrm{erg}}{\mathrm{s}}\,f_\mathrm{heat}\left(\frac{n_e}{\mathrm{cm}^{-3}}\right)\frac{1}{4\pi r^2}\sqrt{\frac{2t}{3D}} \\ &\quad\times H[t - r^2/(6D)]\int_{\beta_{0min}}^{\beta_{0max}}\frac{\beta^2 n_{cr}(\beta_0)}{\beta^3 + x_m^3}d\beta_0\,. \end{aligned} \tag{2.18}$$

Here we have written the CR spectrum in terms of the initial spectrum $n_{cr}(\beta_0)d\beta_0(\equiv n_{cr}(\beta)d\beta)$ in order to explicitly show the limits in terms of the initial values, whose constraints have been discussed in §1.

In the approximation of static gas, the energy deposited by CR protons into the gas results in the change in temperature as, $d\epsilon = \frac{3}{2}n_{\rm IGM}k\,dT$. However, we also take gas cooling into account in order to calculate the change in temperature with time.

2.4.1 Continuous SF case

We first discuss the case of continuous star formation. The process of star formation is likely to last for as long as there is gas available. The typical star formation time scale is the inverse of the specific SFR (sSFR), and it decreases from ~ 10 Gyr at $z = 0$ to ~ 0.3 Gyr at $z \geq 2$ (Lehnert et al., 2015). For a conservative estimate it is reasonable to assume that CR heating continues for a time period of ~ 0.1 Gyr.

The resulting temperature profiles are shown in Figure 2.5 for $z = 10$ for two cases: high SFR (10 $M_\odot$ yr^{-1} in a $10^{10}M_\odot$ galaxy) with photoionized IGM in the upper left panel, and low SFR (0.003 $M_\odot$ yr^{-1} in a $10^{12}M_\odot$ galaxy) with neutral IGM in the lower left panel. Dashed lines show the temperature profile without cooling and solid curves show the profile with cooling, for three different epochs, at $10, 50, 100$ Myr after the onset of star formation. Black curves show the result of heating with initial energy lower limit of protons at 1 MeV, and green curves show the profiles when the lower limit is 100 keV. The profiles show a discontinuity, which stems from the assumption of the initial spectrum being a power law down to a certain minimum energy and zero below it. The discontinuity in the temperature profile occurs at r_0 (which is given by equation 2.12)from the virial radius ($R_{\rm vir} = 6.4$ kpc for $10^{10}M_\odot$ galaxy and $R_{\rm vir} = 29.6$ kpc for $10^{12}M_\odot$ galaxy) of the source galaxy where the minimum energy proton loses all its energy, as defined earlier. In reality, the spectrum will have a smooth change of slope below the minimum energy assumed here, and the temperature profile will consequently be more continuous than shown here. However, it is useful to define the distance r_0, as we have done here, which indicates a change of shape in the temperature profile.

In the limit of static gas the change in temperature is independent of the density, since $d\epsilon(= 1.5n_{\rm IGM}k\,dT) \propto n_e$, in equation 2.18. However the profile strongly depends on Δ since r_0 depends on gas density.

As expected from the value of the diffusion coefficient, the heating effect is noticeable only within a few kpc. This is further reduced to when gas cooling is considered. We also show the variation of the result with diffusion coefficient in the middle panels, for three values of D. As expected from previous discussion,the local heating decreases with increasing value of D. We also show the variation of the results with the CR spectral index α, and find that a flatter energy spectrum decreases the heating effect.

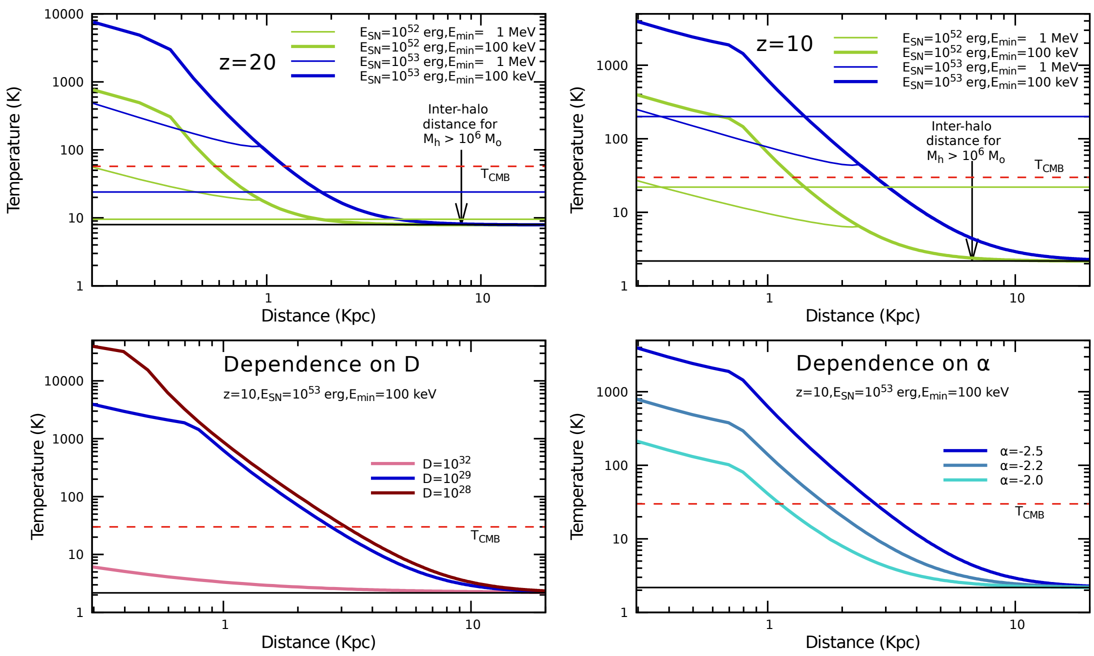

Figure 2.6: The temperature profile for a primordial SN in a mini-halo of $M_h = 10^6$ $M_\odot$ at $z = 20$ (left-most panel) and $z = 10$ (second from left panel). The green curves in both panels show the case for $E_{\rm SN} = 10^{52}$ erg and the blue curves, for $E_{\rm SN} = 10^{53}$ erg; upper curves are for $E_{\rm min} = 100$ keV and lower curves are for $E_{\rm min} = 1$ MeV. The horizontal green and blue lines correspond to the increased global mean temperature in each case. The horizontal red dashed lines correspond to the CMB temperature. Vertical arrows mark the inter-minihalo distance for a minimum mass of 10^6 $M_\odot$. The two panels on the bottom show the variation of the result with diffusion coefficient (bottom left) and CR spectral index α (bottom right), as in Figure 2.5.

2.4.2 Minihalo-SF burst case

Next we discuss the case of a burst of star formation in high redshift minihalos, as considered by Sazonov & Sunyaev (2015). As representative cases, we consider a minihalo of total halo mass $M_h = 10^6$ $M_\odot$ at two redshifts $z = 10$, and $z = 20$. The corresponding virial radii of the galaxy at these redshifts are $r_{\rm vir} = 0.29, 0.15$ kpc. Following Sazonov & Sunyaev (2015), we assume that the average supernova (SN) explosion energy is $E_{\rm SN} = 10^{52}$–10^{53} erg and the average number of SNe per minihalo is $f_{\rm SN} = 1$. As in the previous section, we assume that a fraction $\eta = 0.1$ of the total SNe energy is converted into accelerating CR particles.

We can adopt the gas heating equation 2.18 to the case of a burst of CR particles, by writing $n_{cr}(\beta_0) = N_{\rm cr}(\beta_0)\delta(t - [r^2/(6D)])$ within the integral. The distribution function of CR particles produced in the burst is normalised by,

$$\int E_k \, N_{\rm cr}(p_0)\, dp_0 = \eta f_{\rm SN} E_{\rm SN} \,, \tag{2.19}$$

which is similar to equation 2.2.

In the absence of cooling in the neutral IGM (since the resulting temperature change is shown to be small below), the CR particles heat up the surrounding as they diffuse and sweep past the IGM gas. The change in the energy density of gas at distance r at time t due to CR protons with initial β_0 is given by,

$$\begin{aligned}\Delta\epsilon(r) &= \int_0^t n_{cr}(\beta_0) f_{\rm heat}\frac{dE}{dt}\frac{1}{4\pi r^2}\sqrt{\frac{2t}{3D}}\,dt \\ &= \frac{1}{4\pi r^2}\int_0^t N_{\rm cr}(\beta_0)\delta[t-\frac{r^2}{6D}]\, f_{\rm heat}\frac{dE}{dt}\sqrt{\frac{2t}{3D}}\,dt \\ &= \frac{2.9\times10^{-19}}{12\pi D\, r}\Big(\frac{n_{\rm HI}}{\rm cm^{-3}}\Big) f_{\rm heat}\frac{2\beta^2}{\beta_c^3+2\beta^3}\,N_{\rm cr}(\beta_0)\,. \qquad (2.20)\end{aligned}$$

Here $\frac{dE}{dt}$ refers to energy loss of a CR proton in neutral medium (equation 2.5).

The resulting temperature difference at distance r from the minihalo is found by a simple integration over the energy spectrum of CR to be,

$$\Delta T = \frac{7.4\times10^{-5} f_{\rm heat}}{D\times r}\times\frac{n_{\rm HI}}{n_{\rm IGM}}\int_{\beta_{0min}}^{\beta_{0max}}\frac{\beta^2 N_{\rm cr}(\beta_0)}{2\beta^3+\beta_c^3}\,d\beta_0\,. \qquad (2.21)$$

Again, the temperature profile is dependent on the assumption of Δ through the relation between β_0 and β by equation 2.11.We show the results in Figure 2.6 for the case of $E_{\rm SN}=10^{52}$ erg for PopIII stars and $f_{\rm SN}=1$, at two redshifts $z=10,20$. The more optimistic case of a pair instability SN with $E_{\rm SN}=10^{53}$ erg is shown by the upper curve, for which the value of ΔT is an order of magnitude larger than the fiducial case, and the IGM temperature exceeds the CMB temperature near the virial radii.

The integral in the above equation is roughly constant up to a distance of r_0 from the virial radius, and decreases as $r^{0.7\alpha}$ beyond that, roughly up to $\sim 2r_0$. Therefore the temperature profile for 0.1MeV $<$ $\rm E_{min}$ $<$ 1MeV can be written as,

$$\begin{aligned}\Delta T &\approx 25\,{\rm K}\Big(\frac{f_{\rm heat}}{0.25}\Big)\Big(\frac{\eta\, f_{\rm SN}\,E_{\rm SN}}{0.1\times10^{52}\,{\rm erg}}\Big)\Big(\frac{E_{0,min}}{1\,{\rm MeV}}\Big)^{-1.2}\times \\ &\quad \Big(\frac{|\alpha|}{2.5}\Big)^{10.8\times\left(\frac{E_{0,min}}{1{\rm MeV}}\right)^{-0.1}}\times(r_{\rm kpc}+R_{\rm vir})^{-1}\times \\ &\quad \Big(\frac{D}{10^{29}\,{\rm cm^2\,s^{-1}}}\Big)^{-1} \qquad ,R_{\rm vir}<r<(r_0+R_{\rm vir}) \\ \Delta T &\approx \Delta T(r_0+R_{\rm vir})\Big(\frac{r_{\rm kpc}+R_{\rm vir}}{r_0+R_{\rm vir}}\Big)^{[0.7\alpha-1]} \\ &\qquad ,(r_0+R_{\rm vir})<r<(2r_0+R_{\rm vir}) \qquad (2.22)\end{aligned}$$

If the diffusion coefficient increases beyond the fiducial value at high redshift, because of a lower magnitude of magnetic field in the IGM, then the temperature profile extends to larger distances but with a lower magnitude.

Figure 2.6 also shows the typical distances between mini-halos ($R_{\rm interhalo}$), assuming a minimum halo mass of 10^6 $M_\odot$ with vertical arrows. We can then use our calculated temperature profile to determine the average increase in temperature within this length-scale, given by,

$$\Delta T_{\rm avg} = \frac{\int \Delta T 4\pi r^2 dr}{(4/3)\pi (R^3_{\rm interhalo} - R^3_{\rm vir})} \,. \tag{2.23}$$

This value should be compared with the global temperature increase calculated by Sazonov & Sunyaev (2015). Following them, if we define a fraction $\eta_{\rm LECR}$ as the product of CR acceleration efficiency (η) and the energy fraction carried by low energy CRs (which deposit their energy into the IGM within the Hubble time), and $n_h(z)$ as the number density of mini-halos, then according to their equation 11, the global increase in temperature is given by,

$$\Delta T_{\rm IGM} = \frac{f_{\rm heat}\eta_{\rm LECR} f_{\rm SN} E_{\rm SN}}{(3/2)k\, n_{\rm IGM}(z)} n_h(z) \tag{2.24}$$

We have calculated this value using the appropriate $n_h(z)$, for $M_{\rm min} = 10^6$ $M_\odot$, $M_{\rm max} = 10^7$ $M_\odot$, by using the *CAMB* transfer function calculator and the fitting function of Reed et al. (2007). The calculation has been done by the HMF calculator given by Murray et al. (2005).

The fraction $\eta_{\rm LECR}$ depends on the assumed CR spectrum, and we use the appropriate values in our calculation. For $\alpha = -2.5$, the energy fraction in low energy cosmic rays (≤ 30 MeV) is 0.17, and for $\alpha = -2.2$, it is 0.05. Since we have used a cosmic ray acceleration efficiency(η) of 10%, we have $\eta_{\rm LECR} = 0.017$ and 0.005 for $\alpha = -2.5$ and -2.2, respectively.

If the local average as calculated using equation 2.23 exceeds the global average increase in temperature, then it would imply that the heating by CR is patchy, and the temperature profiles presented here are representative of the effect of CR heating. On the other hand, if the local average is less than the global average increase in temperature, then it would mean that CR heating is rather uniform and the temperature profile calculated by us would be subsumed under the global increase in temperature.

We find from equation 2.24 that for $E_{\rm SN} = 10^{53}$erg, the global temperature increase is 198 K at redshift 10 and 16 K at redshift 20, whereas the local average temperature increase from equation 2.23 is 16 K and 2 K at redshift 10 and 20 respectively. Therefore we can put upper bounds on the diffusion coefficient D at high redshift, for which CR heating would be inhomogeneous (larger D would imply a more uniform heating). We have found that at $z = 10$, the limit is $D \leq 1 \times 10^{26}$ cm^2 s^{-1}.

Therefore for our fiducial value (see §2.2) of $D \sim 10^{29}$ cm^2 s^{-1}, the heating is likely to be uniform. At $z \sim 20$, the corresponding limit is $D \leq 5$–6×10^{26} cm^2 s^{-1}, which also implies uniform heating since D is likely to be above this limit. However, one should remember there are uncertainties in the evolution of magnetic field with redshift and the dependence of D on the magnetic field.

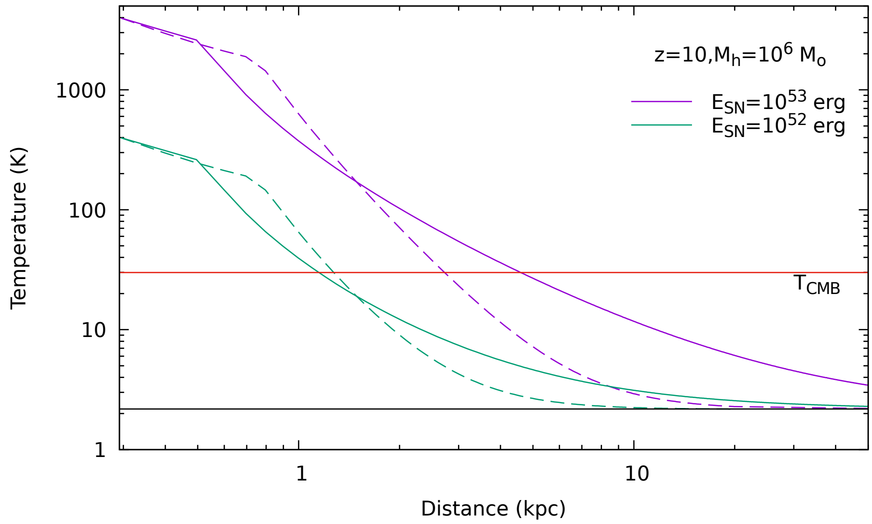

Figure 2.7: The temperature profile for a primordial SN in a mini-halo of mass $10^6 M_\odot$ and at $z = 10$ assuming $E_{min} = 0.1$MeV. The dashed curves show the temperature profiles when the gas density outside the halo is 10 times the baryonic matter density at that epoch and the solid curves are obtained using a density profile of gas around the halo.

2.4.3 Effect of a density profile

Having calculated the temperature profile using a constant IGM density, we now show the effect of a density profile, by assuming a simple power-law relation. Simulations of accretion of mass around massive halos have shown that the density profile around the virial radius of haloes is steeper than r^{-2}, but becomes flatter than r^{-2} beyond the virial radius (up to a distance of $\sim 5R_{\rm vir}$) (Prada et al., 2006). Moreover, the overdensity at $\sim R_{\rm vir}$ is $\Delta \sim 100$. The overall profile from $R_{\rm vir}$ to $\sim 5R_{\rm vir}$ can therefore be approximated by,

$$n(r) = 100 \frac{\rho_{\rm cr}(z)\Omega_m(z) f_b}{\mu m_p} \left(\frac{r}{R_{\rm vir}}\right)^{-2}. \tag{2.25}$$

This profile would change the r-dependence in the equations relating β and β_0 (equations 2.11 and 2.15) that can be analytically calculated.

We show the change in the temperature profile for the mini-halo case in Figure 2.7, for $z = 10$, and $M_h = 10^6$ M$_\odot$, for two values of $E_{\rm SN}$ and $E_{\rm min} = 0.1$ MeV. The dashed profiles correspond to a uniform density with $\Delta = 10$ as assumed earlier (see Figure 2.6). The solid lines show the case of the above mentioned density profile. The approximate concurrence of these two curves justifies our assumption of $\Delta = 10$ for the uniform density case.

The case of a continuously star forming galaxy with a density profile outside $R_{\rm vir}$ is shown in Figure 2.8. Here, although the temperature near the virial radius is similar to the case of uniform density (again justifiying the assumption of $\Delta = 10$), the temperature profile is steeper than the uniform density case, because of the change in the relation between β with distance.

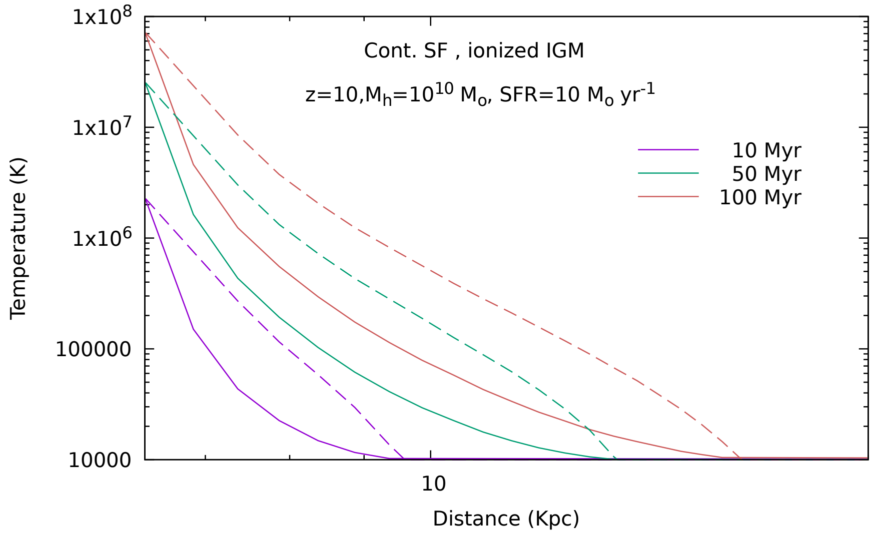

Figure 2.8: The temperature profile for continuous star formation in a galaxy of $M_h = 10^{10} M_\odot$ at $z = 10$ assuming $E_{min} = 0.1$ MeV. The dashed curves show the temperature profiles when the gas density outside the halo is uniform and 10 times the baryonic matter density at that epoch and the solid curves are obtained using a density profile of gas around the halo as in equation 2.25.

2.5 Discussion

The temperature profile in the neutral case shows that if the SFR is to be low enough to keep the surrounding gas neutral and high enough to cause substantial heating, as in the case portrayed in the lower panel of Figure 2.5, the gas temperature can exceed the CMB temperature (shown by a horizontal red line) within a few kpc of the galaxy, if the lower limit of CR proton energy is 100 keV. This was the scenario sketched by Sazonov & Sunyaev (2015), which we have quantified here, and shown the dependencies on various parameters. However, even if such a case of heating arises, it is unlikely to be probed in the near future by observations as the corresponding angular scale is very small, of the order of a few arc seconds.

The temperature profiles in Figure 2.5 show that gas temperature in the ionized case can increase to 10^7 (10^6) K for $E_{0,min} = 0.1(1)$ MeV in a time period of ~ 50 Myr, for SFR of 10 $M_\odot$ yr^{-1}. This implies that the gas in the outskirts of the galaxy likely to be heated up to a high temperature, which would set up an outward motion. This will affect the gas infall into the parent galaxy and in turn influence the evolution of the star formation process in it.

It is reasonable to argue that if the sound speed of the gas heated by CR exceeds the infall velocity near a galaxy, then CR heating will tend to suppress the further gas infall. The infall velocity is roughly estimated as $\sqrt{GM_h/R_{vir}}$, and independent of the distance from the galaxy, up to $\sim 1.5 \times R_{\rm vir}$ (Goerdt & Ceverino, 2015). Therefore we can determine

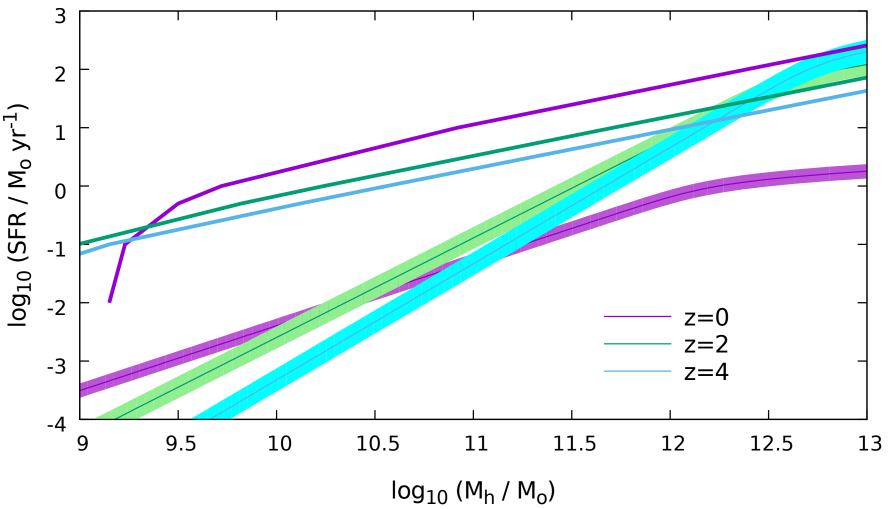

Figure 2.9: SFR for different galaxies masses are shown for $z = 0, 2, 4$. Shaded lines show the star formation rates of main sequence of galaxies, and the solid lines show the lower limits of SFR from the condition that sound speed of the heated gas near the virial radius should exceed the infall speed, $E_{0,min} = 100$ keV.

the minimum SFR needed to inhibit gas infall around a galaxy of a given mass at a certain redshift. We can then compare it to the SFR of main sequence of galaxies appropriate for galaxies of the same mass at that redshift.

We show in Figure 2.9 the SFR of main sequence of galaxies as a function of halo mass at $z = 0, 2, 4$ by shaded lines. We have used the fit to SFR as a function of stellar mass and cosmic time as given by Speagle et al. (2014), and the analytical fit for the relation between stellar mass and halo mass, as given by Behroozi et al. (2010), and the shaded region show $1 - \sigma$ error bars. Superposed in the same figure are lines that show the lower limits on SFR needed to suppress gas infall by CR heating near the virial radius, for $E_{0,min} = 100$ keV (solid lines). For the calculation at these low redshifts, we have used a fiducial value $D = 10^{29} \mathrm{cm}^2 \mathrm{s}^{-1}$ as discussed in §2.2.

We find that, if the lower limit of CR protons is 100 keV when they escape from galaxy, then CR heating affects the infall of gas around galaxies of $\mathrm{M}_h \sim 10^{10}$ $\mathrm{M}_\odot$ for SFR of order ~ 1 $\mathrm{M}_\odot$ yr^{-1}. For more massive galaxies, CR heating can be important for suppression of infall if the SFR ≥ 100 times the SFR of main sequence of galaxies. at $z = 0$. This gap (between required SFR and SFR of main sequence of galaxies) narrows with increasing redshift. At $z \sim 4$, infall around galaxies with $M_h \sim 10^{12}$ $\mathrm{M}_\odot$ can be affected for the SFR of main sequence of galaxies. Therefore CR heating can be an important feedback mechanism for regulating gas infall around massive galaxies at high redshift.

2.6 Summary

We have calculated the radial temperature profile of the IGM around galaxies due to heating by CR protons after taking into account the effect of diffusion of CRs. We assumed a simple power-law CR spectrum with a low energy cutoff, and a constant diffusion coefficient for low energy CRs. We considered three cases: (1) heating of neutral IGM at high redshift around galaxies with low enough SFR so that the IGM is not photoionized, (2) heating of photoionized IGM around high SFR galaxies and (3) heating of neutral IGM at high redshift around a minihalo on account of primordial supernovae. Our main results are:

- It is not easy for low energy CRs to escape relatively massive galaxy (Figure 2.1).
- The surrounding medium of galaxies at high redshift is likely to be ionized on account of star formation in the galaxy. Therefore, the heating by CRs will proceed in a different manner than previously considered case of neutral IGM heating.
- In the case of CRs from mini-halos at $z \sim 10$–20, we put an upper bound on the diffusion coefficient ($D \leq 1 \times 10^{26}$ cm^2 s^{-1} for $z \sim 10$ and $D \leq 5$–6×10^{26} cm^2 s^{-1} for $z \sim 20$) for which the heating is inhomogeneous, after comparing our temperature profiles with the estimate of global temperature increase. Given the expected scaling of the diffusion coefficient with redshift, this bound suggests uniform heating, both at $z \sim 10$ and 20. But the uncertainties in CR parameters (spectrum, lower energy limit of emerging CRs, diffusion coefficient and its dependence on magnetic field) and magnetic field at high redshift precludes any firm conclusion.
- In the case of continuous star formation and neutral IGM in the vicinity of galaxies with low SFR, the temperature exceeds the CMB temperature for $D < 10^{30}$ cm^2 s^{-1}, and in this case the profile is too peaked to be detectable.
- Furthermore, we found that the heated gas near the virial radii of galaxies can provide a feedback mechanism by inhibiting the infall of gas, especially for massive galaxies at high redshift ($z \sim 4$), and low mass star forming galaxies at low redshifts for sufficiently high SFR.

3

Radio Background and IGM heating from Pop III supernova explosions

We consider the synchrotron emission from high energy electrons accelerated in supernova explosions of massive Population III stars in high redshift minihaloes of mass $10^{5-7}M_{\odot}$*. We also take into account the heating of intergalactic medium (IGM) by cosmic ray protons accelerated in the same sites. We study the combined effect of these two interactions on the global 21 cm radiation from the beginning of the epoch of reionization.*

Key results :

- The radio background created by the synchrotron emission of CR electrons increase the depth of the absorption trough in 21 cm signal from the cosmic dawn. The resulting intensity of the radio background is substantial to explain the recently reported *EDGES* result.
- The associated heating of the IGM by CR protons decrease the depth of the trough.

The two competing processes — production of radio background and heating of IGM by Pop III supernovae — determine the depth of the absorption trough in the resulting 21 cm signal from the beginning of the epoch of reionization. The trade-off between these two processes is such that the 21 cm brightness temperature cannot be larger than $|\Delta T_{21}| \sim 0.25$ K which can be probed in future experiments and used as a test of this scenario.

Based on:

"Radio background and IGM heating due to Pop III supernovae explosions" by **Ranita Jana**, Biman B. Nath, Peter. L. Biermann, *MNRAS*, *483*(4), 5329-5333. (2019), (Jana et al. 2019)

3.1 Introduction

The epoch in the history of the Universe when the first luminous objects formed has long been a topic of interest. It has been estimated that the Population III (Pop III) stars formed inside dark matter haloes (the so-called minihaloes) with virial temperature ~ 1000 K and mass $\sim 10^6$ $M_\odot$ at $z \sim 20 - 30$ (Haiman et al., 1996; Tegmark et al., 1997; Bromm et al., 2009). They fundamentally transformed the Universe not only by producing the first sources of light but also in other aspects. The ionizing radiation from these luminous objects (perhaps aided by those from early quasars usually interpreted as activity of supermassive black holes (Puchwein et al., 2019); for the activity of early stellar mass black holes, see e.g., (Mirabel et al., 2011)) ultimately led to the reionization of the Universe. This ionizing radiation could have come from either the Pop III stars themselves (Venkatesan & Truran, 2003) or from the Pop III supernovae explosions (Johnson & Khochfar, 2011). The supernovae explosions likely accelerated cosmic rays (CR), which would have heated the intergalactic medium (IGM) (Sazonov & Sunyaev, 2015). These CRs could have also produced a neutrino background, as has been estimated by Berezinsky & Blasi (2012).

A powerful probe of these early epoch is the redshifted 21 cm radiation from neutral hydrogen atoms (Barkana & Loeb, 2001). The properties of this radio signal strongly depend on the deviation of the HI spin temperature from the cosmic microwave background (CMB) temperature ($\Delta T_{21} \propto (T_S - T_{CMB})$). The kinetic temperature of the inter-galactic medium was coupled to the HI spin temperature by $z \sim 15$ due to the resonant scattering of Lyα photons. This gives rise to a prominent absorption feature in the global 21 cm signal. None of the existing reionization models can explain the observed absorption trough of the first detected redshifted global 21 cm spectrum at $z \sim 17$, (Bowman et al., 2018) the depth of which is almost twice than expected. The shape of the absorption trough with its sharp edges is also rather difficult to understand in the context of standard models. It should be noted that the detection of first redshifted global 21 cm signal is yet to be confirmed. Hills et al. (2018) expressed concerns about the cosmological origin of this signal.

There have been suggestions (e.g., (Barkana, 2018; Barkana et al., 2018; Berlin et al., 2018); see also Biermann & Kusenko (2006)) that there might be baryonic-dark matter interaction which would have caused excess cooling of the cosmic gas, leading to a deep absorption trough. Another possibility is that of a global radio background which would also explain the observations (Feng & Holder, 2018). Indeed, such a radio background at $z \sim 20$ was predicted by Biermann et al. (2014), arising from explosions concomitant with the formation of first supermassive black holes, motivated by the excess radio background observations at the present epoch (Fixsen et al., 2011), which has been independently confirmed recently by Dowell & Taylor (2018). Recently, Ewall-Wice et al. (2018) considered the radio background from growth of seed black holes at high redshift, and determined the required black hole seed function. However, the physics of the formation of these seed black holes remain highly uncertain.

In this chapter, instead of invoking early black holes, we consider another, and perhaps more abundant, source of radio background, namely, the effect of supernovae (SNe) explosions of Pop III stars in dark matter minihaloes which were abundant at these redshifts. We have estimated the brightness temperature of the radio background generated by high energy CR electrons interacting with magnetic fields in the shocked inter-galactic medium, and shown how this radio background could have been important vis-a-vis the 21 cm absorption experiment.

3.2 Pop III supernovae and cosmic rays

It is believed that Pop III stars appeared at $z \sim 20 - 30$ in dark matter minihaloes of mass $10^{5-7}\mathrm{M}_{\odot}$. Although there are significant uncertainties in the initial mass function of these stars, it is thought that the mass function was dominated by massive stars in the range of $\sim 10 - 10^3\mathrm{M}_{\odot}$. They lived for several million years (e.g. Schaerer (2002)) and a significant fraction (or most) of them likely exploded as powerful pair-instability SNe, with energies much larger than that of present day SNe, of the order of $\sim 10^{53}$ erg (Sazonov & Sunyaev (2015),Hirano et al. (2014),Heger & Woosley (2010)). It has also been shown that the UV radiation from Pop III stars forms HII regions, and the supersonic shock waves associated with R-type ionization front sweeps away most of the gas in the minihaloes (e.g.Yoshida et al. (2007)). This decrease in gas density reduces the radiation loss of subsequent SN remnants (SNR), which are able to travel beyond the virial radius of the minihaloes. They would suffer radiation loss when they encounter the shell of gas previously blown away by the ionization front. However, it has been found that these primordial SNRs would travel to a few times the virial radius before mixing with the IGM, and thereby destroying the minihaloes of mass $\leq 10^7$ $\mathrm{M}_{\odot}$, the range we are interested in here (Kitayama & Yoshida, 2005; Vasiliev et al., 2008). We note that these explosions would leave no stellar remnants and therefore the scenario under consideration here does not involve black holes of any mass range.

Consider the SNRs from Pop III stars around minihaloes at $z \approx 17$. The minimum mass of halos that can efficiently cool with molecular hydrogen is $\approx 5 \times 10^5$ $\mathrm{M}_{\odot}$ (for $h = 0.7$) Tegmark et al. 1997; Yoshida et al. 2003. If we consider minihaloes in the mass range $5 \times 10^5 - 10^7$ $\mathrm{M}_{\odot}$, then at $z = 17$, their comoving number density is $n_h \approx 338(h/0.6774)^3$ Mpc^{-3}, using the *CAMB* transfer function calculator and the fitting function of Reed et al. (2007). This has been calculated using the HMF calculator given by Murray et al. (2013) and the cosmological parameters used are determined by Planck Collaboration et al. (2016). Suppose that each minihalo gives rise to $f_{\mathrm{SN}} \sim 1$ SN with energy $E_{\mathrm{SN}} \sim 10^{53} E_{53}$ erg. The baryonic mass density of the IGM is $\rho_{\mathrm{IGM}}(z) \approx 2.4 \times 10^{-27} \left(\frac{f_b}{0.157}\right)\left(\frac{\Omega_{m0}}{0.3089}\right)\left(\frac{1+z}{18}\right)^3$ g cm^{-3}, for a cosmic baryon fraction of ~ 0.157 and the matter density fraction at present epoch $\Omega_{m0} \sim 0.3089$. There are three distinct stages of SNR evolution. At first the ejecta freely expands until the swept out mass is comparable to the ejecta mass. It is followed by an adiabatic expansion of the shocked gas which is known as Sedov-Taylor(S-T) phase. The (physical) radius in the S-T phase is,

$$R_{ST} \sim 1.2\,\mathrm{kpc}\, E_{53}^{1/5}\, t_{14}^{2/5}\, \rho_{\mathrm{IGM}}(z)^{-1/5}\,, \tag{3.1}$$

where t_{14} is time after the explosion in the unit of 10^{14} s $\approx$ 3 Myr. In comparison, the virial radii of minihaloes of the considered masses are in the range $\sim 143 - 389$ pc. These SNRs lose energy through inverse Compton scattering off CMB photons, with a cooling time $t_{\mathrm{IC}} \sim 7 \times 10^{14}$ s at $z \approx 17$ for Lorentz factor $\gamma_e = 1$. However, the radiative phase begins at $t \sim 10^{14}$ s, somewhat earlier, when the cooling of the shocked gas reaches a maximum rate (Sutherland & Dopita, 1993). This happens when the post shock temperature of the ionised shell is ≈ 1–2×10^5 K, corresponding to the shell speed of order $v \sim 90$–$120\, E_{53}^{1/5} \rho_{\mathrm{IGM}}(z)^{-1/5} t_{14}^{-3/5}$ km s^{-1}. This is therefore the epoch of beginning of the radiative phase. Thereafter the SNRs rapidly decelerate and disperse into the IGM. The spacing between minihaloes, from the above mentioned number density, is estimated as ~ 4.9 kpc. In other words, the SNRs lose steam by the time they reach a distance $\sim 25\%$ of the inter-halo distance. The volume filling fraction is ≈ 0.02.

Like Galactic SNRs, these primordial SNRs in all likelihood accelerate CRs by diffusive shock acceleration (DSA). The prerequisite for this method to work are magnetic irregularities and the formation of shocks. The magnetic field in the IGM at these epochs is likely to be scaled up from the present day value by a factor of $(1+z)^2$. Observations suggest that $B \le 10^{-9}$ G at present epoch (although this is valid for a coherence length of ~ 1 Mpc; Kronberg 1994; Subramanian 2016). Therefore one expects an intergalactic magnetic field of order $B_{\mathrm{IGM}} \sim 0.32\,\mu$G at $z \approx 17$. One possible origin of this magnetic field could be stellar winds and SNe of Pop III stars themselves (Bisnovatyi-Kogan et al., 1973). These seed magnetic fields can be amplified by small-scale dynamo in the cores of minihaloes (Sur et al., 2010).

Recall that the surroundings of minihaloes are expected to be ionised by the UV radiation of Pop III stars. Simulations of the ion Weibel instability even in the absence of pre-existing magnetic fields have shown that a shock front can form in this case (Weibel, 1959; Spitkovsky, 2008). Although these simulations have been carried out for relativistic plasmas, it is likely that the result will hold for non-relativistic motions of Pop III SNRs since the general physical principles that lead to the formation of shock fronts remain unchanged (Berezinsky & Blasi, 2012).

The next requirement for DSA is the existence of magnetic irregularities upstream and downstream of the shock. It is thought that cosmic ray streaming instability can cause magnetic turbulence upstream. It is a non-linear process, and accelerated particles excite the instability while DSA occurs in the presence of turbulent magnetic field (Lucek & Bell 2000; Bell & Lucek 2001). Berezinsky & Blasi (2012) estimated that magnetic field in the vicinity of Pop III SNRs would reach up to $\delta B \sim 4.7\, V_9^{1/2}\,\mu$G, using an ambient magnetic field of 0.32μG, IGM particle density $n_{\rm IGM} \sim 2.4 \times 10^{-3}$ cm^{-3} and an efficiency of CR acceleration (see below) of 0.15 in their equation 3 when the non-linearity proceeds in a resonant way. Here V_9 is shock speed in the units of 10^4 km s^{-1}. This implies an amplification $\delta B/B \sim 14.7\, V_9^{1/2}$. In the non-resonant case, their equation 4 leads to an amplification factor of $\delta B/B \sim 35\, V_9^{3/2}$. For downstream magnetic fields, observations indicate that the magnetic field in young SNRs (in our Galaxy (Bell, 2013), or in other galaxies, e.g, in M82 (Biermann, 1986) can be as large as $\sim 10 - 100$ times the ISM value, or even more (see Table 1 of some individual radio SNRs in Biermann et al. (2018)). We will assume a fiducial value of $\delta B/B \sim 100$ and characterise the factor by which magnetic field is increased from the IGM value by $\zeta_B \sim 100\, \zeta_{B,100}$.

The efficiency with which the shock kinetic energy is converted into CR energy is another uncertainty. Simulations of DSA in non-relativistic shocks show that a fraction $\eta_{\rm CR} \sim 0.1 - 0.2$ of the shock kinetic energy is spent in accelerating CRs (Caprioli & Spitkovsky, 2014). As a fiducial value we will assume $\eta_{\rm CR} \sim 0.15$. Since most of the CR energy is in protons, we need another parameter to characterise the spectrum of CR electrons, namely, the ratio of CR electrons to protons energy. We assume that this ratio is given by $(m_e/m_p)^{(3-p)/2}$, where p is the power-law index of the energy spectrum of CRs (see equation 10 in Persic & Rephaeli (2014); also Merten et al. (2017)). We will assume $p \approx 2.2$, (Berezinsky & Blasi, 2012) for which this ratio is $\eta_e \approx 0.05$. Together with the efficiency parameter $\eta_{\rm CR}$, the number density of minihaloes n_h and the energy of Pop III SNe, $E_{\rm SN}$, the energy density of CR electrons (in physical units) is therefore,

$$\begin{aligned} \epsilon_{\rm CR,e} &= \eta_e \eta_{\rm CR} f_{\rm SN} E_{\rm SN} n_h \\ &= 0.05 \times 0.15 \times 1 \times 10^{53} {\rm erg} \times \frac{338\,(1+17)^3}{\rm Mpc^3} \\ &\approx 5 \times 10^{-17} {\rm erg\, cm^{-3}}\,. \end{aligned} \tag{3.2}$$

Now if $n(\gamma_e)d\gamma_e$ denotes the number density of electrons with Lorentz factor γ_e in the range γ_e to $\gamma_e + d\gamma_e$ then this allows us to write the CR electron energy spectrum as $n(\gamma_e)d\gamma_e = A\gamma_e^{-p} d\gamma_e$, with the normalization,

$$A = \frac{(p-2)\epsilon_{\rm CR,e}}{m_e c^2} = 6.1 \times 10^{-11}\,(p-2)\,E_{53}\,{\rm cm}^{-3}\,. \tag{3.3}$$

Here the units are physical, and we have used the fiducial values for η_e, $\eta_{\rm CR}$, $f_{\rm SN}$ mentioned above.

The synchrotron emissivity of these CR electrons in magnetic field B averaged over all electron pitch angles is given by Rybicki & Lightman (1986), (with Γ denoting gamma

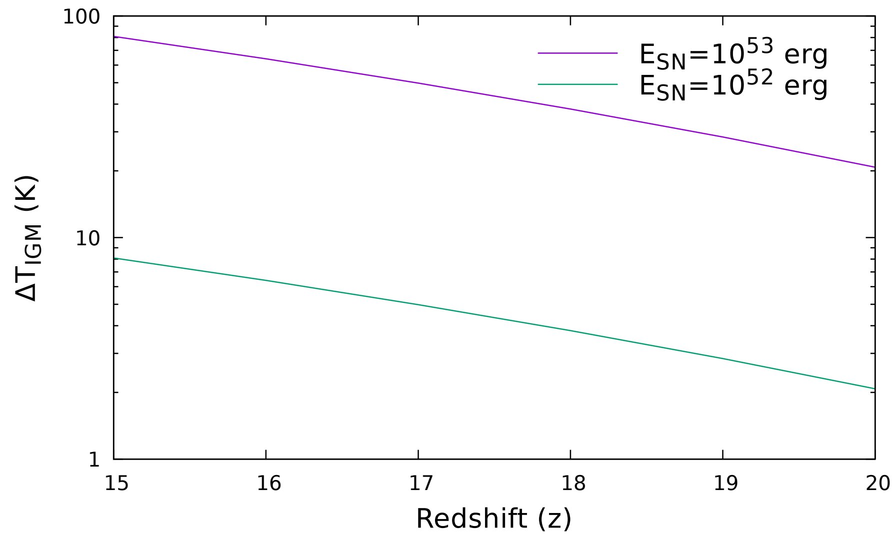

Figure 3.1: Global increase in IGM temperature by CR protons for $E_{\rm SN} = 10^{52}, 10^{53}$ erg as a function of redshift, without considering diffusion of CR.

functions)

$$\begin{aligned} j_\nu &= \frac{\sqrt{3}e^3 AB}{8\sqrt{\pi} m_e c^2 (p+1)} \Gamma\Big(\frac{p}{4} + \frac{19}{12}\Big)\Gamma\Big(\frac{p}{4} - \frac{1}{12}\Big) \frac{\Gamma(\frac{p+5}{4})}{\Gamma(\frac{p+7}{4})} \\ &\quad \times \Big(\frac{2\pi m_e c \nu}{3eB}\Big)^{-(p-1)/2} \\ &\approx 3.1\times 10^{-43}\,{\rm erg\,s^{-1}\,Hz^{-1}\,cm^{-3}\,sr^{-1}}\,\zeta_{B,100}^{1.6}\,E_{53}\,. \end{aligned} \tag{3.4}$$

The specific intensity is given by $I_\nu = j_\nu \times (c/H(z))$. We have $c/H(z) \approx 104$ Mpc at $z = 17$. Therefore we have,

$$I_\nu \approx 10^{-16}\,\zeta_{B,100}^{1.6}\,E_{53}\,\frac{\rm erg\ s^{-1}}{\rm cm^2\ sr\ Hz} \tag{3.5}$$

The corresponding brightness temperature is

$$T_B(z=17) = \frac{I_\nu c^2}{2k\nu^2} = 160\,\zeta_{B,100}^{1.6} E_{53}\,{\rm K}\,. \tag{3.6}$$

This increases the depth of the absorption trough by a substantial factor $= \frac{(T_B + T_{\rm CMB})}{T_{\rm CMB}}$ from the standard value. Therefore, given the uncertainties and the dependence on B, a radio background that can explain the observed absorption trough is tenable.

This radio background is weakly dependent on the redshift of the occurrence of Pop III supernovae. If we use the corresponding comoving number density of minihaloes at $z = 20$ ($141\,(h/0.6774)^3\,{\rm Mpc}^{-3}$), the redshift at which the observed absorption trough begins, then the emissivity is $\approx 3.4\times 10^{-43}\,{\rm erg\,s^{-1}\,Hz^{-1}\,cm^{-3}\,sr^{-1}}\zeta_{B,100}^{1.6}\,E_{53}$. Using the value of $c/H(z)$ at $z = 20$ ($83\,(h/0.6774)$ Mpc), one gets a brightness temperature,

$$T_B(z=20) \approx 138\,\zeta_{B,100}^{1.6} E_{53}\,{\rm K} \tag{3.7}$$

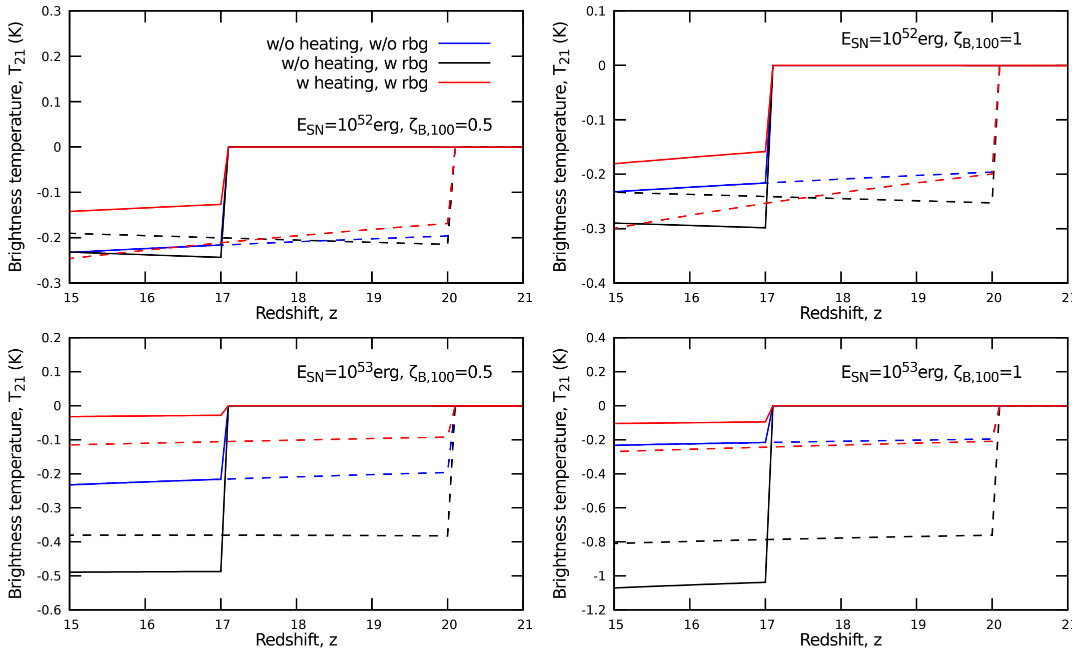

Figure 3.2: Brightness temperature of 21 cm signal as a function of redshift, assuming a sudden coupling of spin temperature with gas temperature at $z = 20$ (dashed lines), 17 (solid lines), for three cases: (1) one in the standard case, without any additional radio background and associated heating (blue lines), (2) with an additional radio background but with heating suppressed (black lines), and (3) with a radio background and the associated heating (red lines). The four panels show the cases with $E_{SN} = 10^{52}$ and 10^{53} erg, and $\zeta_{B,100} = 1$ and 0.5.

The duration over which this radio background is produced will depend on the time distribution of Pop III supernovae, which is uncertain. In the simplest scenario, if one considers these supernovae to go off within a short time (shorter than the corresponding Hubble time), then the radio background will amount to the magnitude we have estimated above. At lower redshifts, this background will suffer cosmological dilution, and one can calculate the evolution of the factor $\frac{T_B+T_{CMB}}{T_{CMB}}$ with redshift, for different values of the initial redshift. We note that the constraints on cooling timescales as mentioned by Sharma (2018) is not relevant in our case because the radio background is not a sustained one.

3.3 Heating of IGM

Another important implication of the present scenario is the heating of the IGM gas by CR protons, which would accompany the CR electrons responsible for a radio background. Sazonov & Sunyaev (2015) calculated the heating in this particular scenario, and we can use their result to discuss the fraction of energy of Pop III supernovae that could go into CR protons. According to their estimate, protons with energy ≤ 30 MeV would lose their energy within a Hubble time at $z \sim 20$. Suppose the fraction of energy contained in these low energy protons is η_{LECR}, then according to their estimate, the temperature of the IGM gas would increase by (where $f_{\rm heat} = 0.25$ is the fraction of CR proton kinetic energy deposited as heat through Coulomb interactions),

$$\Delta T_{\rm IGM} = \frac{2 f_{\rm heat} \eta_{LECR} \eta_{CR} E_{SN}}{3\,k\,(\rho_{\rm IGM}/1.2 m_p)} n_h \,. \tag{3.8}$$

We show this temperature increase in Figure 4.8 for $E_{\rm SN} = 10^{53}$ erg, $\eta_{CR} = 0.15$, as used for the radio background calculation, and $\eta_{LECR} = 0.05$ that is appropriate for $p = 2.2$. The typical IGM gas temperature at $z \sim 20$ is $T \approx 2.725 \times 151[(1+z)/151]^2$ K$\approx$ 8 K. The figure shows that the temperature increase due to CR protons can be substantial and would go against deepening the absorption trough. However it is possible to obtain the same radio background as in equation 6 with $E_{53} < 1$ as long as $\zeta_{B,100}$ is suitably larger than unity. This would also decrease the concomitant heating effect, as shown by the variation of heating with $E_{\rm SN}$ in Figure 4.8.

In order to assess the important heating vis-a-vis the effect of the radio background due to Pop III SN explosions, we need to calculate the brightness temperature of the global 21 cm signal after the redshift of explosions. In the standard scenario, the spin temperature of neutral IGM gets decoupled from the CMB temperature at $z \sim 150$ as the gas decouples from CMB, and then gets coupled to it again at a lower redshift, due to lack of electrons. At a still lower temperature, due to the surge of Lyman-α photons coming from Pop III stars, the spin temperature gets coupled to the gas temperature again. For simplicity (and to describe our model in terms of the least number of free parameters), let us assume that the spin temperature T_s becomes equal to T_g, the gas temperature at a certain redshift $z \sim 20$. Then the differential brightness temperature of 21 cm radiation is given by the standard expression (assuming the neutral fraction to be unity) (Zaldarriaga et al., 2004).

$$\Delta T_{21}(z) \approx 0.023\, K \Big[\Big(\frac{0.15}{\Omega_m h^2}\Big)\Big(\frac{1+z}{10}\Big)\Big]^{\frac{1}{2}} \Big(\frac{\Omega_b h^2}{0.02}\Big)\Big[1 - \frac{T_R(z)}{T_S(z)}\Big] \,. \tag{3.9}$$

Here $T_R = T_B + T_{\rm CMB}$. We show the resulting absorption feature in Figure 3.2, without the effect of X-ray heating, but including the effect of heating due to protons from Pop III SNe. We show three curves: (1) one in the standard case, without any additional radio background and associated heating, (2) with an additional radio background but with heating suppressed, and (3) with a radio background and the associated heating, for various combination of parameters, for two cases in which the coupling of spin temperature with gas temperature occurs at $z = 20$ and 17.

The curves in Figure 3.2 show that it is difficult to achieve the brightness temperature as observed by *EDGES* if the heating due to protons is taken into account. The heating is decreased when E_{SN} is low, but then the radio background is also low, and the brightness temperature remains the same. Changing the cosmic ray efficiency parameter $\eta_{\rm CR}$ also does not make any difference. Decreasing $\zeta_{B,100}$ reduces the brightness temperature because of the decrease in the radio background intensity. However, one could argue that the ratio of CR electrons to protons, which we have taken to be $(m_e/m_p)^{(3-p)/2} \approx 0.05$ could be different and it would change the radio background intensity without altering the heating effect. If this ratio is ≈ 0.25 at $z = 17$ (and 0.13 at $z = 20$) then one could get an absorption trough of depth ≈ 0.5 K. The trade-off between these two effects is an important testable prediction of the two-sided effect of Pop III SNe for future experiments.

3.4 Discussions

We can calculate the brightness temperature of the redshifted radio background at the present epoch, and compare with the observations by *ARCADE-2* experiment (Fixsen et al., 2011) (independently confirmed by Dowell & Taylor (2018)). The 1.4 GHz signal when redshifted to present epoch, yields a brightness temperature of $160/18 = 8.9$ K at 78.89 MHz, whereas the radio background observed at the same frequency by *ARCADE-2* is ≈ 845 K, two orders of magnitude higher than the background considered by us. This conclusion is consistent with that of Feng & Holder (2018) who noted that a background with intensity even 1% of the *ARCADE-2* result would have an observable effect at high redshift 21 cm observations. We note that one can increase the radio background intensity by increasing $f_{\rm SN}$, the number of SN per minihalo, and bring it to agreement with the *ARCADE-2* (although $f_{\rm SN} \sim 100$ would be rather unrealistic), but then the IGM heating would scale up by a similar factor.

Another important prediction from the present model is the number of sources in the radio sky. The number of shells (before they are rapidly decelerated and stop accelerating CRs) per solid angle is (where $r(z) = d_L(z)/(1+z)$ is the coordinate distance to redshift z and d_L is the luminosity distance),

$$\frac{c r(z)^2 \Delta z \times n_h}{H(z)} = c r(z)^2 n_h \, \Delta t \, (1+z) \approx 7 \times 10^{11} \, t_{14} \, . \tag{3.10}$$

Within the uncertainties of the estimate, this matches the limit of $\geq 6 \times 10^{11}$ sources per sr put by Condon et al. (2012). We note here that Condon et al. (2012) derived the limit on source density using a beam size of a few arc seconds, the limit can also be explained if the sources are extended.

The relativistic electrons that radiate at 1.4 GHz at $z = 17$ have a typical Lorentz factor of $4 \times 10^3 \, \zeta_{B,100}^{-1/2}$. These electrons will also inverse Compton scatter the CMB photons (with $T_{\rm CMB} = 49$ K at $z = 17$) to ~ 66 keV X-ray photons. The energy density of these X-ray photons in the range $\sim 1 - 100$ keV is roughly 0.05 eV cm^{-3}, which is a fraction $\sim 2 \times 10^{-6}$ of the CMB energy density at that redshift. Therefore the diffuse X-ray background produced by the CR electrons (responsible for the proposed radio background) will not pose any problem with observed X-ray background radiation (which is a fraction $\sim 10^{-3}$ of the CMB).

The corresponding γ-ray background produced by hadronic interactions of CRs with IGM protons is much below the observed background today. The CR proton energy density is $\epsilon_{\rm CR} \approx 10^{-15}$ erg cm^{-3} at $z = 17$. Using a cross-section of $\sigma_{\rm pp} \sim 2.5 \times 10^{-26}$ cm^2, and IGM proton density $\sim 2.4 \times 10^{-3}$ cm^{-3} at that redshift, one gets an energy density of γ-rays,

$$\frac{1}{3}\frac{c\sigma_{\rm pp}\, n_{IGM}\, \epsilon_{\rm CR}}{H(z)} \approx 6.4 \times 10^{-18}\, {\rm erg\, cm^{-3}}\,. \tag{3.11}$$

When redshifted to present epoch, this amounts to an energy density of $\sim 6.1 \times 10^{-23}$ erg cm^{-3}, much below the observed diffuse γ-ray background energy density of $\sim 10^{-18}$ erg cm^{-3} (Ackermann et al., 2015).

3.5 Summary

We have considered the effect of CRs accelerated during Pop III supernovae, which are an inevitable consequence of the emergence of the first stars in the Universe. Various effects of these CRs have been earlier considered in the literature, including the heating of IGM and the neutrino background. We have shown that the radio background arising from CR electrons can be large enough to explain the recently observed depth of absorption trough by *EDGES* but then the associated heating due to CR protons would tend to decrease the brightness temperature. Our model provides a testable prediction of this important process, and it is hoped that future experiments will shed more light on this era.

4

Role of Cosmic Rays in the early stages of galactic outflows

The star formation and supernova activities in the galactic disk can give rise to large scale ($\sim$ several kpc) galactic outflow. This outflowing gas plays a major role in the galactic evolution. They regulate the star formation in the galaxy as well as enrich the intergalactic medium with metals. However, the driving mechanism of this outflowing gas is not yet clear. The thermal pressure of the outflowing gas has been treated in the literature as the dominant driving force, although the contribution from non-thermal pressure components is also being studied in recent times. Using an idealized set-up, we investigate the dynamical role of cosmic rays (CRs) in the early stages of galactic outflows for galaxies of halo masses 10^8, 10^{11} *and* 10^{12} $M_\odot$. *The outflow is launched from a central region in the galactic disk where we consider three different constant star formation rates* (0.1, 1, *and* 10 $M_\odot\ yr^{-1}$) *over a dynamical timescale of* 50 *Myr.*

Key results :

- CRs can reduce the temperature of the shocked gas, which is consistent with previous results.
- CRs do not have any noticeable effect on the mass loading by the outflow.
- CRs can *reduce* the size of the outflow, which contradicts previous claims of efficient dynamical impact of CRs; however, it is consistent with earlier theoretical models of cosmic ray driven blastwave as well as stellar wind.
- In the early stages of galactic outflows the dynamical role of CRs is not important.

Based on :
"Role of cosmic rays in the early stages of galactic outflows" by **Ranita Jana**, Siddhartha Gupta, Biman B. Nath, *MNRAS*, *497*(3), 2623–2640 (Jana et al. 2020)

4.1 Introduction

Galaxies form as a consequence of gravitational collapse of large gas clouds into dark matter halos. With the onset of star formation, a substantial amount of gas is expelled from the galaxies as the form of biconical outflow, as attested by observations of starburst galaxies (see e.g., Veilleux et al. 2005 for review). These galactic scale outflows play an important role in the dynamical and chemical evolution of galaxies. Theoretical studies that do not include such feedback mechanism overproduce the star formation rate (SFR) and baryon fraction in galaxies. Outflows are therefore believed to regulate the star formation process, and consequently influence galactic evolution. These outflows also enrich the inter-galactic matter with metals which mostly form in the star forming regions. Although outflows are a crucial aspect of galactic evolution, their driving mechanism and modes of propagation are still poorly understood.

Thermal pressure due to shock heating of the inter-stellar medium (ISM) by supernovae and stellar winds in star formation sites have been the focus of most previous studies (Efstathiou 2000; Girichidis et al. 2016; Martizzi et al. 2016). Non-thermal pressure, such as pressure due to radiation from young stars (Murray et al. 2005; Hopkins et al. 2012; Krumholz & Thompson 2012; Agertz et al. 2013; Skinner & Ostriker 2015; Rosdahl et al. 2015) and/or cosmic rays (CRs) (Ipavich 1975; Drury & Voelk 1981; Breitschwerdt et al. 1991; Zirakashvili et al. 1996; Hanasz & Lesch 2003; Samui et al. 2010; Recchia et al. 2016; Gupta et al. 2018a) have also been suggested as important driving mechanism as thermal pressure. Preliminary analytical works assumed ideal coupling between CRs and thermal gas mediated by damped Alfvén waves and without diffusion. Ipavich (1975) considered a spherical outflow emanating from a point mass galaxy of $10^{11}\ M_{\odot}$ and found that CRs escaping from a galaxy are able to carry thermal gas with them and produce a galactic wind with mass loss rate 1–10 $M_{\odot}$ yr^{-1}. Breitschwerdt et al. (1991) improved this model by considering a disk galaxy and a 'mushroom'-type geometry of the outflow. Everett et al. (2008) used these ideas for a possible outflow from Milky Way and reported that galactic wind models incorporating thermal pressure as well as CR pressure produce the best fit to the observed Galactic diffuse soft X-ray emission. Recently, Samui et al. (2018) used a spherically symmetric thin shell model to study the effect of CR pressure on the dynamics of outflow. They suggested that for the low mass galaxies where thermal pressure alone cannot sustain a large scale galactic outflow (because of radiative cooling, which peaks at $\sim 10^5$ K), the inclusion of CRs may drive a steady outflow.

In addition to analytical models, hydrodynamical (HD) and magnetohydrodynamical (MHD) simulations have also been used. Uhlig et al. (2012) performed the first HD simulations to investigate the effects of CR heating due to streaming instability (see eg. Kulsrud & Pearce (1969) for review). However, CR diffusion was not included in their simulations and CRs were assumed to heat the gas above the disk scale height, which can affect the outflow. For a better understanding, Booth et al. (2013) and Salem & Bryan (2014) used a more realistic set-up by considering advection as well as isotropic diffusion of cosmic rays seft-consistently. They found that the large-scale pressure gradient established by CR diffusion helps to drive the wind. Ruszkowski et al. (2017) performed global three dimensional MHD simulation of an isolated Milky Way sized galaxy to investigate the role of two different CR transport mechanisms, namely streaming and anisotropic diffusion. Similar to Booth et al. (2013) they found that SFR is significantly decreased when CRs are included in their simulations. They also found that in the presence of moderately super-Alfvenic CR streaming, the mass loading factor ranges between ~ 0.25 to ~ 0.6. Recently, these models have been further improved by Butsky & Quinn (2018) where CR streaming, isotropic and anisotropic diffusion of cosmic rays have been investigated. They reported that all three transport mechanisms result in strong metal rich outflows which largely differ from the models without CRs in terms of the temperature and ionization structure of circumgalactic medium (CGM).

The effects of CRs are primarily quantified using the parameters such as mass loading factor and the presence of multiphase gas in the outflow and in the CGM. The mass loading factor (usually denoted by η), which is defined as the ratio of gas outflow rate to the SFR, and is indicative of the efficiency of outflows in ejecting mass from the host galaxy. For example, Booth et al. (2013) found that $\eta \sim 0.5$ in the case of Milky Way-sized galaxies (virial mass of $10^{12}\ M_{\odot}$), with or without CRs, while in the case of low mass galaxies, such as the Small Magellanic Cloud (SMC) ($2 \times 10^{9}\ M_{\odot}$), it can be ~ 10 with CR and ~ 1 without CRs. A multiphase structure of galactic winds and the existence of cold gas ($T \sim 10^{4} K$) in the wind was noticed by Booth et al. (2013), Salem & Bryan (2014) and Butsky & Quinn (2018). This owes to the fact that while thermal pressure driven winds are accelerated in the disk, the CR driven winds are accelerated smoothly into the halo. The pressure gradient in the halo is 3–10 times higher in the case of CR driven wind, compared to pure thermal pressure driven wind. They have shown that the CR-driven winds have a lower speed and support 'cold' gas, which the authors have used to explain the existence of multiphase gas in the CGM. CR driven winds in massive galaxies have been recently studied by Fujita & Mac Low (2018), for a galaxy of mass $5 \times 10^{12}\ M_{\odot}$, with a continuous mechanical power of 10^{43} erg s^{-1}, that corresponds to a SFR of ~ 100–$500\ M_{\odot}$ yr^{-1}. They found it is difficult for CRs to drive a wind from massive galaxies, even with a large SFR, and found that $\eta \lesssim 0.006$–0.03. In addition to this, Jacob et al. (2018) performed simulations of galaxies of mass range between 10^{10} and $10^{13}\ M_{\odot}$ and concluded that mass loading factor drops rapidly with virial mass with an approximate relation $\eta \sim M_{\rm vir}^{\alpha}$ where α is between -1 and -2. This relation is slightly steeper than the previously reported results. Their simulations also reveal that CRs cannot drive a steady mass-loaded outflow if the virial mass of the galaxy is more than $10^{12}\ M_{\odot}$ which supports the results by Fujita & Mac Low (2018).

Most of the previous works, with the notable exception of Fujita & Mac Low (2018), assume a feedback mechanism by which the SFR is regulated, and the star formation activity changes with time during the simulation runs. The resulting effects of CR is therefore entangled with various factors and it is not clear how (a) galactic mass, (b) star formation rate, (c) CR injection sites and (d) different assumptions of diffusion contribute towards the propagation of outflows. It is no wonder that the results of these studies have remained inconclusive.

In this chapter, we study with the help of idealized simulations, the outflow properties for three galactic masses (10^{12}, 10^{11} and 10^{8} $M_{\odot}$, hereafter M12, M11 and M8 respectively) using constant star formation rates for $\sim$ few Myr. Our primary focus is to investigate the outflow dynamics in the early stages (until 50 Myr) of galaxy evolution, where the constant star formation rate is a reasonable assumption. For the fiducial case, we also investigate long term evolution (until 210 Myr) with time-dependent star formation rate, however, without including feedback from the outflowing gas on the star formation. These assumptions allow us to distinguish the role of the individual physical process separately, which can be extended in a more realistic scenario.

We find that although the presence of CRs increases the cold gas mass in the outflow, the dynamical impact of CRs is not important in the early stages of galaxy evolution. We present our simulation set up and results in Sections 4.2 and 4.3. We discuss the results of our long-duration simulations with periodic star formation in Section 4.4. Implications of our work and comparisons with previous studies are discussed in Section 4.5 and summarised in Section 4.6.

4.2 Simulation set-up

We solve the following two-fluid CR hydrodynamical equations using PLUTO code (Mignone et al. 2007; Gupta et al. 2019)

$$\frac{\partial \rho}{\partial t} + \nabla \cdot (\rho \boldsymbol{v}) = S_{\rho} \tag{4.1}$$

$$\frac{\partial (\rho \boldsymbol{v})}{\partial t} + \nabla \cdot (\rho \boldsymbol{v} \otimes \boldsymbol{v} + p_{\rm t} \mathbf{I}) + \rho \nabla \Phi_{\rm t} - \frac{\rho v_{\phi}^2}{R} \hat{\mathbf{R}} = 0 \tag{4.2}$$

$$\frac{\partial}{\partial t}(\rho v^2/2 + e_{\rm th} + e_{\rm cr}) + \nabla \cdot [(\rho v^2/2 + e_{\rm th} + e_{\rm cr} + p_{\rm t})\boldsymbol{v}] = -q_{\rm cool} + S_{\rm th} \tag{4.3}$$

$$\frac{\partial e_{\rm cr}}{\partial t} + \nabla \cdot (e_{\rm cr} \boldsymbol{v} + \mathbf{F}_{\rm crdiff}) = -p_{\rm cr} \nabla \cdot \boldsymbol{v} + S_{\rm cr} \tag{4.4}$$

Here ρ is the mass density and v is the velocity of the gas. The total pressure, $p_{\rm t}$, is the sum of thermal pressure ($p_{\rm th}$) and CR pressure ($p_{\rm cr}$). Here $\rho v^2/2$ is the kinetic energy density, $e_{\rm th} = p_{\rm th}/(\gamma_{\rm th} - 1)$ is the thermal energy density and $e_{\rm cr} = p_{\rm cr}/(\gamma_{\rm cr} - 1)$ is the CR energy density , where $\gamma_{\rm th} = 5/3$ and $\gamma_{\rm cr} = 4/3$ are the adiabatic constants of the gas and CRs respectively. The term $v_{\phi}^2/R\hat{\mathbf{R}}$ in the momentum equation represents the centrifugal force that acts on the gas due to rotation of the disk. $\Phi_{\rm t}$ is the total gravitational potential (cf.

Section 4.2.1). S_ρ, $S_{\rm th}$ and $S_{\rm cr}$ are the injected mass and energy source terms. The term, $q_{\rm cool}$, denotes the energy lost due to radiative cooling of thermal gas. $\mathbf{F}_{\rm crdiff}$ represents the flux term associated with isotropic CR diffusion.

4.2.1 Gravitational Potential

The total gravitational potential denoted by $\Phi_{\rm t}$ in equations 4.2 is the superposition of gravitational potential exerted by a stellar disk and dark matter halo. For the stellar disk, we use the Miyamoto & Nagai potential (Miyamoto & Nagai, 1975). In cylindrical coordinate (R, z), it is given by

$$\Phi_{\rm disk}(R,z) = -\frac{GM^{\star}_{\rm disk}}{\sqrt{R^2 + (a+\sqrt{z^2+b^2})^2)}}, \quad (a, b \geq 0), \tag{4.5}$$

Here $R = r\sin\theta$ and $z = r\cos\theta$. $M^{\star}_{\rm disk}$ is the mass of the stellar disk. The two parameters a and b represent the scale length and scale height of the disk respectively.

For the dark matter (DM) halo, we use a modified Navarro-Frenk-White Model (Navarro et al., 1997). The potential is given as

$$\Phi_{\rm DM} = -\frac{GM_{\rm vir}}{\sqrt{R^2+z^2+d^2}}\left[\frac{\ln(1+\sqrt{R^2+z^2+d^2}/r_s)}{f(c)}\right] \quad (d \geq 0), \tag{4.6}$$

where $f(c) = \ln(1+c) - \frac{c}{(1+c)}$ with $c = r_{\rm vir}/r_s$, the concentration parameter. $M_{\rm vir}$ is the total mass of the galaxy (including DM) within virial radius ($r_{\rm vir}$). r_s and d are the scale radius and core radius of the DM distribution respectively. These parameters are listed in Table 4.1.

4.2.2 Initial density and pressure distribution

The initial gas distribution in the galaxy is assumed to have two components: (i) a warm ionized gas (few times 10^4 K) in the disk and (ii) a hot gas ($\sim T_{\rm vir}$). In order to set the initial gas distribution, we use the steady state solution of the Euler's equation by solving

$$-\frac{\nabla p}{\rho} - \nabla\Phi_{\rm t} + \frac{v_\phi^2}{R}\hat{R} = 0\,, \tag{4.7}$$

for each component. The disk and halo gas mass distributions are found to be

$$\begin{aligned}\rho_{\rm d}(R,z) &= \rho_{\rm d0}\exp\Big[-\frac{1}{a_{\rm sd}^2}\{\Phi_{\rm t}(R,z) - \Phi_{\rm t}(0,0) - \\ &\qquad f^2(\Phi_{\rm t}(R,0) - \Phi_{\rm t}(0,0))\}\Big]\end{aligned} \tag{4.8}$$

and

$$\rho_{\rm h}(R,z) = \rho_{\rm h0}\exp\left[-\frac{1}{a_{\rm sh}^2}\{\Phi_{\rm t}(R,z) - \Phi_{\rm t}(0,0)\}\right] \tag{4.9}$$

respectively. Here $\rho_{\rm d0}$ and $\rho_{\rm h0}$ are the central density, and $a_{\rm sd}$ and $a_{\rm sh}$ are isothermal sound speed of the warm disk gas and hot halo gas respectively. The two components of

Table 4.1: The values of parameters used in our simulations

Parameters (Units)	Values (M12)	Values (M11)	Values (M8)
$M_{\rm vir}$ ($M_\odot$)	10^{12}	10^{11}	10^{8}
$M^\star_{\rm disk}$ ($M_\odot$)	5×10^{10}	5×10^{9}	––
$T_{\rm vir}$ (K)	3×10^{6}	6×10^{5}	10^{4}
$T_{\rm disk}$ (K)	4×10^{4}	2×10^{4}	––
$r_{\rm vir}$ (kpc)	258	120	12
$r_{\rm s}$ (kpc)	21.5	10.0	1.0
a (kpc)	4.0	2.0	––
b (kpc)	0.4	0.2	––
d (kpc)	6.0	2.0	1.0
c	12	12	12
f	0.95	0.9	––
$Z_{\rm disk}$ ($Z_\odot$)	1.0	1.0	––
$Z_{\rm halo}$ ($Z_\odot$)	0.1	0.1	0.1
$\rho_{\rm d0}$ ($m_{\rm H}{\rm cm}^{-3}$)	3.0	1.0	––
$\rho_{\rm h0}$ ($m_{\rm H}{\rm cm}^{-3}$)	1.1×10^{-3}	1.5×10^{-3}	2×10^{-4}

the thermal gas (i.e., the warm and hot ionized gas) in the simulation have been treated as a single fluid. Therefore, the total density of the thermal gas is given by $\rho = \rho_{\rm d} + \rho_{\rm h}$.

The term, f in Eq. 4.8 determines the centrifugal force on the gas due to the rotation of stellar disk, i.e.,

$$v_\phi = f\left[\frac{\rho_d}{\rho}\mathrm{R}\left(\frac{\partial\Phi_{\rm t}}{\partial R}\right)_{z=0}\right]^{1/2} \tag{4.10}$$

In the thermally driven outflow models, initially, total pressure of the gas is the sum of pressure due to the disk gas and the halo gas. In the models, where CRs are included, assuming equipartition of energy in the disk, we divide the total thermal pressure in the disk such that $p_{\rm th} = 2\,p_{\rm cr}$. We assume that initially halo gas has a very low CR pressure.

The set-up discussed above is similar to (Sarkar et al., 2015), except that here we have CRs as an additional fluid. We find that for all model parameters listed in Table 4.1, the gas distribution is reasonably stable until $t \gg 100$ Myr. The timescale we are interested in is much smaller than this. The initial density and temperature profiles of the three cases are shown in Figure 4.1.

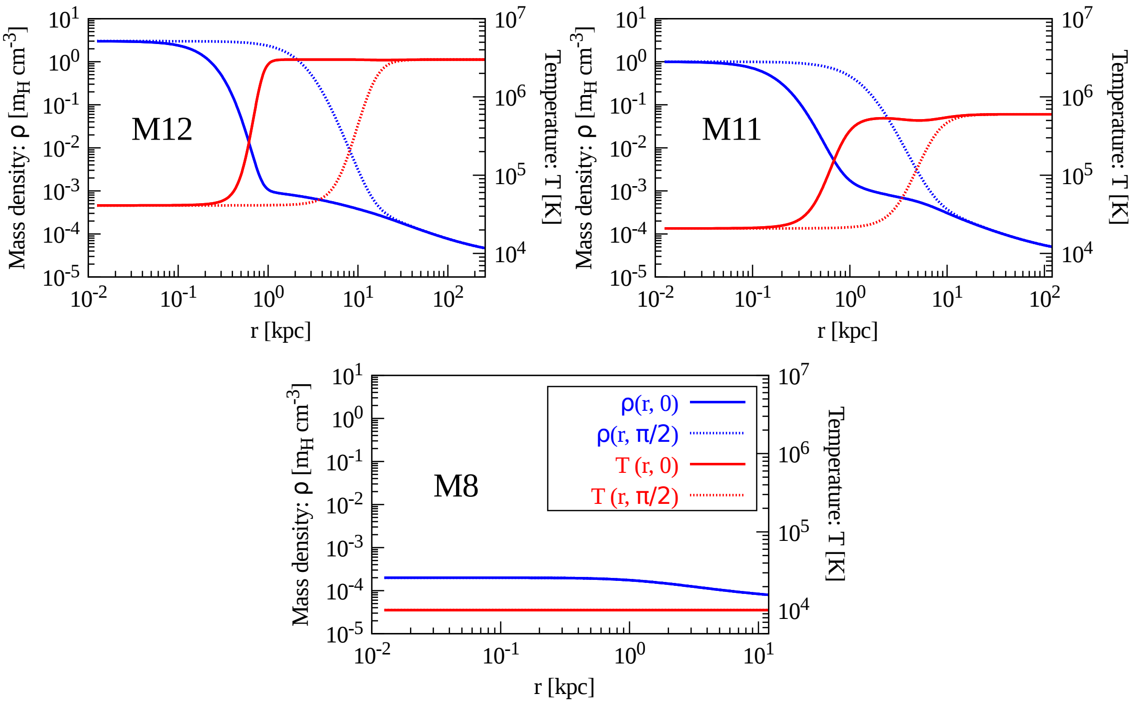

Figure 4.1: Initial density and temperature distributions for three galaxies with halo mass (from top) $10^{12}M_{\odot}$, $10^{11}M_{\odot}$ and $10^{8}M_{\odot}$ respectively. Density (blue) and temperature (red) profiles are shown along $\theta = 0$ and $\theta = \pi/2$. For $M_{\rm vir} = 10^{8}\,M_{\odot}$ (rightmost panel), the profiles are isotropic, because any disk in such a galaxy is expected to be very small compared to the outflow length scale of interest and have not been considered in our simulation.

4.2.3 Solver, grid distribution and boundary

We perform our simulations in 2D spherical geometry with three velocity components. To solve the two-fluid hydrodynamical equations, we use the HLL Riemann solver and take piecewise linear spatial reconstruction for all variables. Time has been evolved using Runge-Kutta 2nd order scheme. We define the computational box from 0.01 kpc to 30 kpc in the r direction and from 0.01 to $\pi/2$ in the θ direction. In the r direction, we take a uniform grid up to 110 pc (20 grid points) and a logarithmic grid thereafter such that total grid along r is 512. Along the θ direction, we take 256 uniform grid distribution. For the extended run, we choose a larger box (70 kpc) with 1024 grid points in the r direction. The inner and outer boundaries for r are set to be outflow, and for θ, both inner/outer boundaries are reflective.

4.2.4 Cooling

We have considered radiative cooling of the warm disk gas and hot halo gas using the tabulated cooling function from Sutherland & Dopita (1993). The dependence of cooling functions on metallicity is taken into account using linear interpolation of the cooling curves between two metallicities. We have assumed that the metallicity of disk gas is solar ($Z = Z_{\odot}$) and the halo gas metallicity is $Z = 0.1\,Z_{\odot}$.

In the simulation, the disk gas rapidly loses its thermal energy due to high metallicity and high density when cooling is considered. However, in reality the disk gas is maintained at $\sim 10^4$ K by stellar radiation. Since we do not include radiation in our simulation, we use a box size of R×z = 15×2 kpc^2 for the $10^{12}\,M_{\odot}$ galaxy and a box size of R×z = 10×4 kpc^2 for the $10^{11}\,M_{\odot}$ galaxy within which we do not allow the disk gas (initially kept at a few times 10^4 K) to cool. However, we allow the injected material to cool, but not below a radiative cooling floor of 10^4 K. (see Appendix 4.A for details of this cooling constraint.)

4.2.5 Mass and energy injections

We assume that multiple supernovae explosions in the central region of the galaxy give rise to continuous energy input in the form of a constant mechanical luminosity. The central region within which thermal energy is deposited is fixed by the condition proposed by Sharma et al. (2014) so that the cooling rate is smaller than the energy deposition rate. The injection region is of radius, $r_{\rm inj}$ = 30 pc in all our models. We perform simulations with three different star formation rates for each galaxy. For Salpeter IMF, assuming the lower and upper limits of stellar mass as 0.1 and 100 $M_{\odot}$ and because each supernova gives rise to $\sim 10^{51}$ erg energy, the relation between mechanical luminosity and SFR (Salpeter 1955; Strickland & Heckman 2007) is given by

$$L = 7 \times 10^{40} \mathrm{erg\,s^{-1}} \left(\frac{\mathrm{SFR}}{1\,M_{\odot}\mathrm{yr}^{-1}} \right) \tag{4.11}$$

On an average 10% of the SFR is the rate of mass injection into the interstellar matter i.e. $\dot{M}_{\rm inj} = 0.1 \times \mathrm{SFR}$.

CRs are injected in the form of pressure wherever a shock is detected (see Fig. 4.2) since shocks are the acceleration sites for CRs. The following conditions (Gupta et al., 2018b) have been used to detect whether a particular region within the simulation box is shocked or not

1. $\nabla \cdot \boldsymbol{v} < 0$
2. $\Delta x |\nabla p|/p > \delta_{\rm tolerance}$
3. $\nabla T . \nabla \rho > 0$

For all our simulations we have used $\delta_{\rm tolerance} = 0.5$. Wherever a shock is detected we redistribute the total pressure between thermal and CR component following the CR pressure component fraction $w = p_{\rm cr}/(p_{\rm th} + p_{\rm cr})$. In all our models we have used $w = 0.2$.

4.3 Results

To understand the properties of outflowing gas between the models with and without CRs, we investigate (i) the morphology of the outflowing gas, (ii) outer shock position,

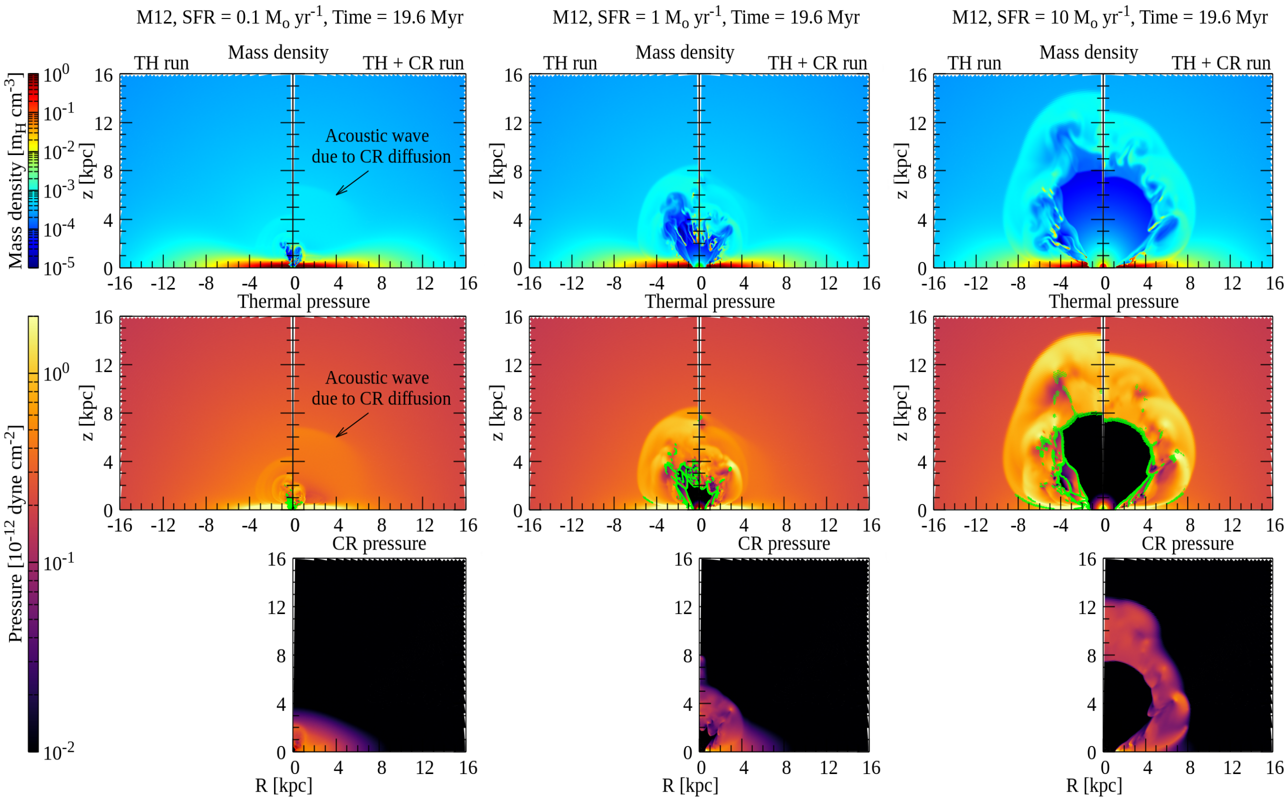

Figure 4.2: Comparison of density and thermal pressure between TH and TH+CR runs for M12 galaxy at ≈ 20 Myr simulation time. The three set of plots (from left) are for SFR = 0.1, 1 and 10 $M_\odot$ yr^{-1}. We also show the CR pressure in a separate plot. Green dots show the shock locations. In the TH+CR runs, these are the locations where CR energy is injected.

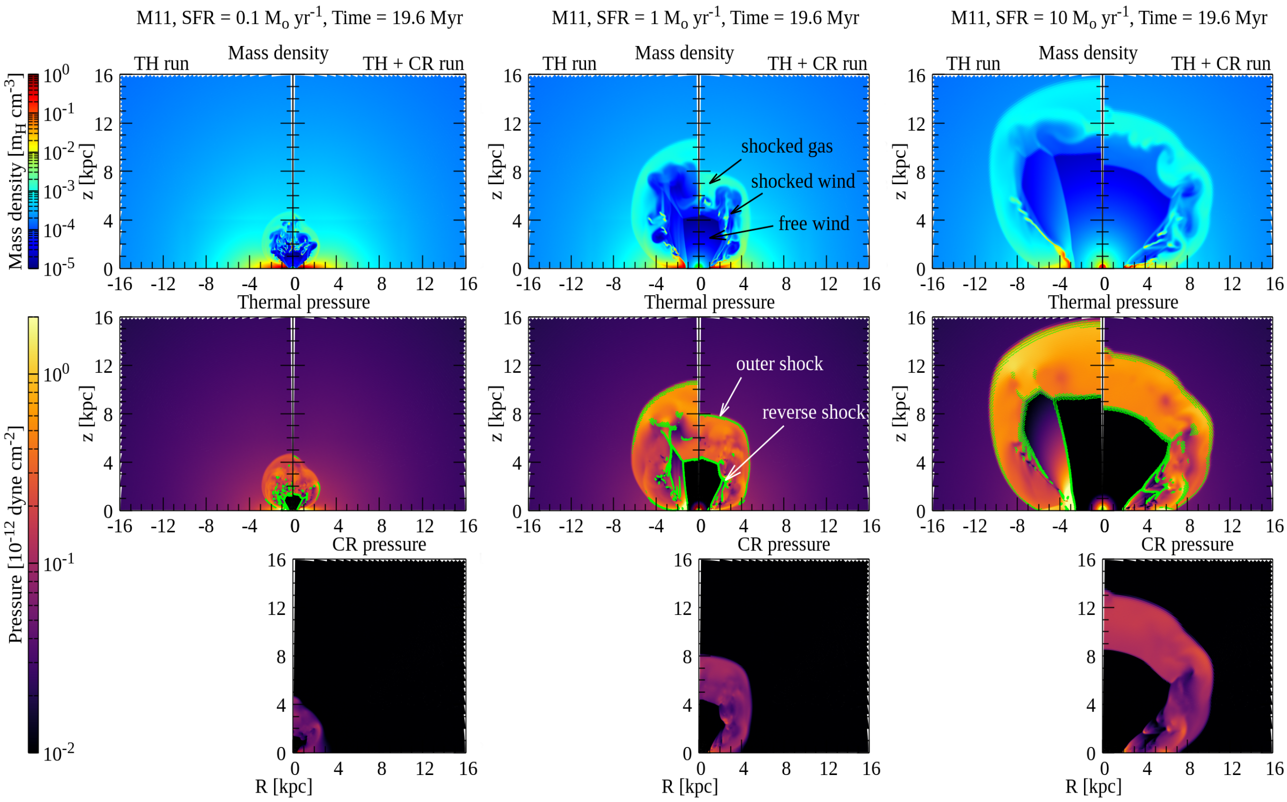

Figure 4.3: Same as Fig. 4.2, for $M_{\rm vir} = 10^{11} M_\odot$

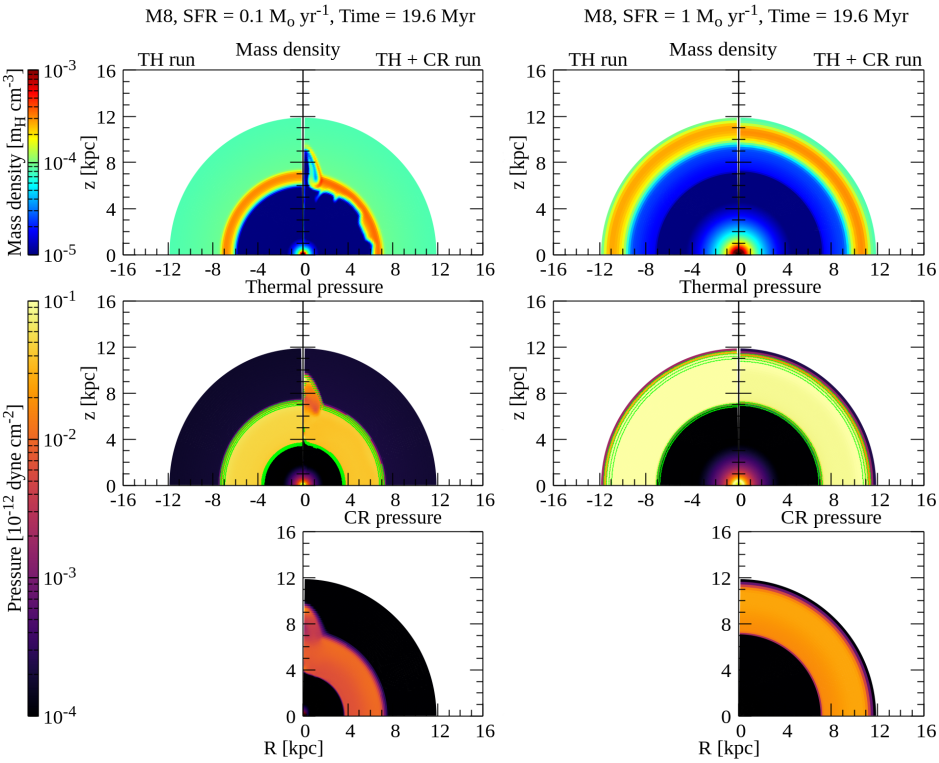

Figure 4.4: Same as Fig. 4.2, for $M_{\rm vir}$ = $10^8 M_\odot$

(iii) mass-loading factor, and (iv) temperature distribution of the gas. These quantities have been used in previous studies to quantify the dynamical impact of CRs. Here we present the results from our simulations of three different galaxies with halo masses $M_{\rm vir}$ = 10^8 , 10^{11} and 10^{12} $M_\odot$ using three different constant star formation rates (SFRs)[1]: 0.1, 1 and 10 $M_\odot$ yr^{-1}. To represent runs with and without CRs, we have used two different labels: 'TH+CR' and 'TH' respectively. Note that we have used our simulation for M11 galaxy as the fiducial run. The used parameters are given in Table 4.1.

4.3.1 Outflow morphology

In Fig. 4.2, 4.3 and 4.4, we show the morphology of outflowing gas for three different halo masses for TH and TH+CR runs. For all runs, we find that the shape of the outflow is nearly spherical in nature. For M8, the shape is expected to be more spherical because, in this case, the galactic disk is much smaller than the outflow length scale and the disk is not included in our simulation. For all cases, the forward and reverse shocks are prominently distinguishable, except for SFR =0.1 $M_\odot$ yr^{-1} in M12 galaxy. In this case the outflow has an irregular shape and does not show a prominent reverse shock; the locations of shocks are rather distributed inside the bubble. This can be seen from the shock locations, as displayed by green dots in the second rows of Figs. 4.2, 4.3 and 4.4.

For SFR = 0.1 $M_\odot$ yr^{-1} (first column of Figs. 4.2, 4.3, and 4.4), a comparison of different

[1]It is to be noted that for 10^8 $M_\odot$ galaxy, SFRs 0.1 and 1 $M_\odot$ yr^{-1} are considered since 10 $M_\odot$ yr^{-1} is unlikely in such a small galaxy.

snapshots among three halos shows that for M12 galaxy, before the outflow breaks out of the central region, an accoustic wave propagates from the central region. This can be understood as follows.

In our set-up, CRs are initially confined in the galactic disk and the halo has very low CR pressure. Due to the pressure gradient, the CRs start to diffuse out of the disk and give rise to the acoustic wave. This feature is not prominent for SFR = 1 and 10 $M_\odot$ yr^{-1} because the velocity of the outflow is greater than this acoustic wave generated due to diffusion of CRs, hence the outflow overtakes it. In other words, such waves can be noticed if the diffusion timescale is smaller than the dynamical timescale of the outflowing gas. The diffusion time scale to reach the disk scale height b is given by

$$\tau_{\rm diff,CR} \approx \frac{b^2}{6\,D_{\rm cr}} \sim 1\,{\rm Myr}\left(\frac{b}{0.4\,{\rm kpc}}\right)^2 D_{\rm cr,28}^{-1} \tag{4.12}$$

where $D_{\rm cr} = 10^{28} D_{\rm cr,28}$ cm^2 s^{-1} is the diffusion coefficient. In case of M11 this acoustic wave initiated by diffusion is not visible because M11 has a puffed up disk compared to M12 (due to the weaker gravity and less steep temperature gradient from the disk to the halo, see Fig. 4.A.1 in Appendix A). Therefore, in this case the acoustic wave is initiated at a later time (due to longer diffusion timescale of CRs) and by that time, it is overtaken by the outflow.

4.3.2 Outer shock position

We show the positions of the forward shocks[2] at $\theta = 20°$ for three different halo masses in Fig. 4.5. In all panels, purple dots represent TH runs and green dots represent TH+CR runs. The positions of the forward shocks for M12 galaxy with low SFRs are difficult to determine, since they do not have a distinct shock structure w.r.t. CGM gas. From the figure, it can be noticed that for higher SFRs, the forward shock distance is *decreased* by the inclusion of CRs (green dots are located below purple dots). The reasons are illustrated as follows:

Injections of CRs at the shocks develop non-thermal pressure in the downstream region, namely, the shocked-wind and the shocked-CGM gas. The effective adiabatic index γ of the composite gas in these regions is determined by the CR injection fraction at the shock. For a non-zero w, the effective γ is reduced from 5/3 to $(5+3w)/[3(1+w)]$ (Chevalier, 1983). Consider two extreme cases, of same amount of energy being either channeled to thermal gas or to CRs. From energy conservation, we then have $3\,p_{\rm cr}V_{\rm cr} = \frac{3}{2}p_{\rm th}V_{\rm th}$, where V denotes volume, with subscripts referring to either the case of CR or thermal gas. The pressure in the shocked region is a certain fraction of the ram pressure ($\rho_{\rm ambient}v_{\rm shock}^2$), and at a given time, they are nearly same (Weaver et al. 1977) in two cases. Therefore $V_{\rm cr} < V_{\rm th}$. In other words, the volume occupied by shocked gas is expected to

[2]One can also choose $\theta = 0°$ to show the positions of the forward shocks, however we notice that it may show some artifacts due to boundary effects.

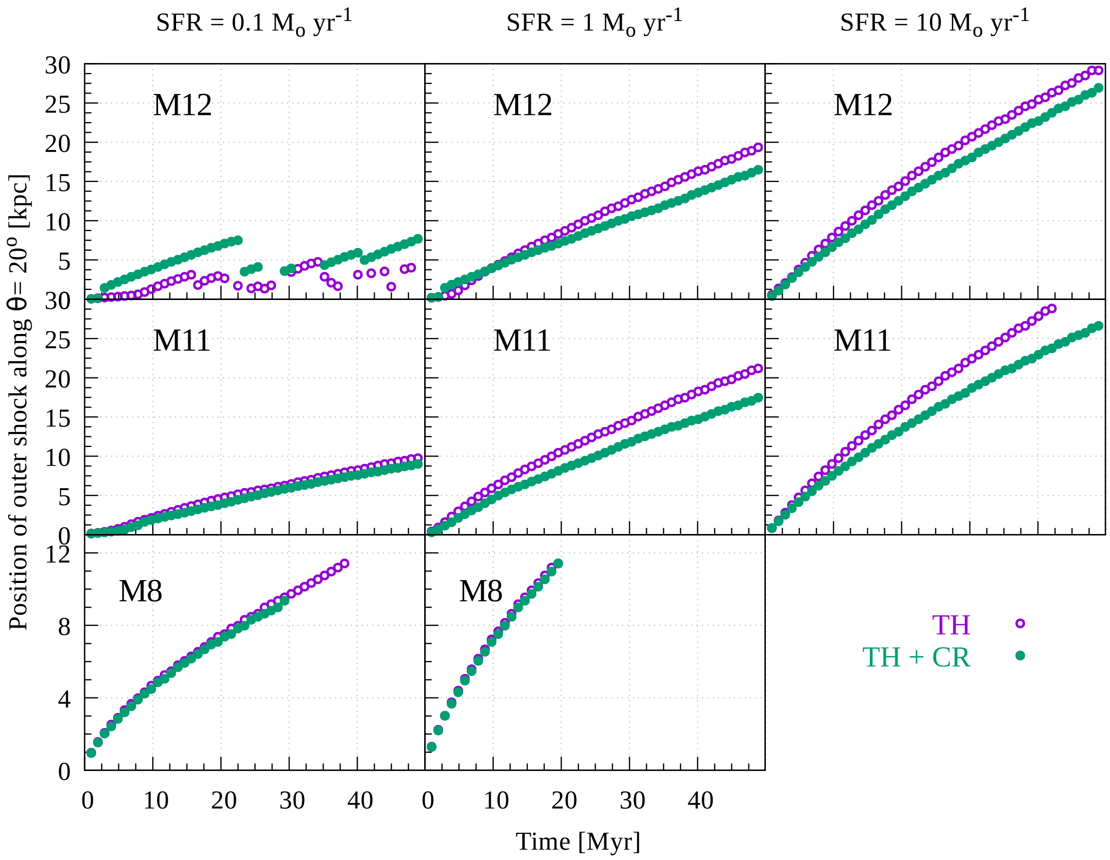

Figure 4.5: Position of forward shock detected at $\theta = 20°$ for M12, M11 and M8 galaxy for star formation rate 0.1, 1 and 10 $M_\odot$ yr^{-1}. The purple dots are for TH run and the green dots are for TH+CR run with diffusion coefficient, $D_{cr} = 10^{28}$cm^{2}s^{-1}. It is clear that the shock traverses a shorter distance when CR is included since a fraction of the energy within the bubble (region within outer shock) escapes due to CR diffusion.

be smaller if the gas is mostly dominated by CRs. Previous studies (for eg. Pfrommer et al. (2017), see Fig. 3, top right corner) that investigated blastwave with CR shock acceleration through 3D simulations also reported similar results. This effect is enhanced by CR diffusion. Diffusion causes the leakage of CR energy from the bubble, which further reduces the size of bubble.[3] This is why the outer shock distance is decreased in the case of TH+CR.

We further elaborate upon these issues in Section 4.2. We show that, in the case of with-CRs no-diffusion run, the outer shock position is slightly smaller than without CR runs. When diffusion is turned on, the difference becomes much larger and the outer shock travels to a shorter distance. In Fig. 4.6, we have shown the total energy (E_t) within the bubble (i.e., within forward shock) as a function of time. In case of TH+CR runs the

[3]The reduced value of effective γ, and the loss of energy through CR diffusion (as in the case of radiation loss) also implies a slightly higher density jump behind the shock, which we have confirmed from our simulation (see for e.g., Fig. 2 in Gupta et al. 2018a).

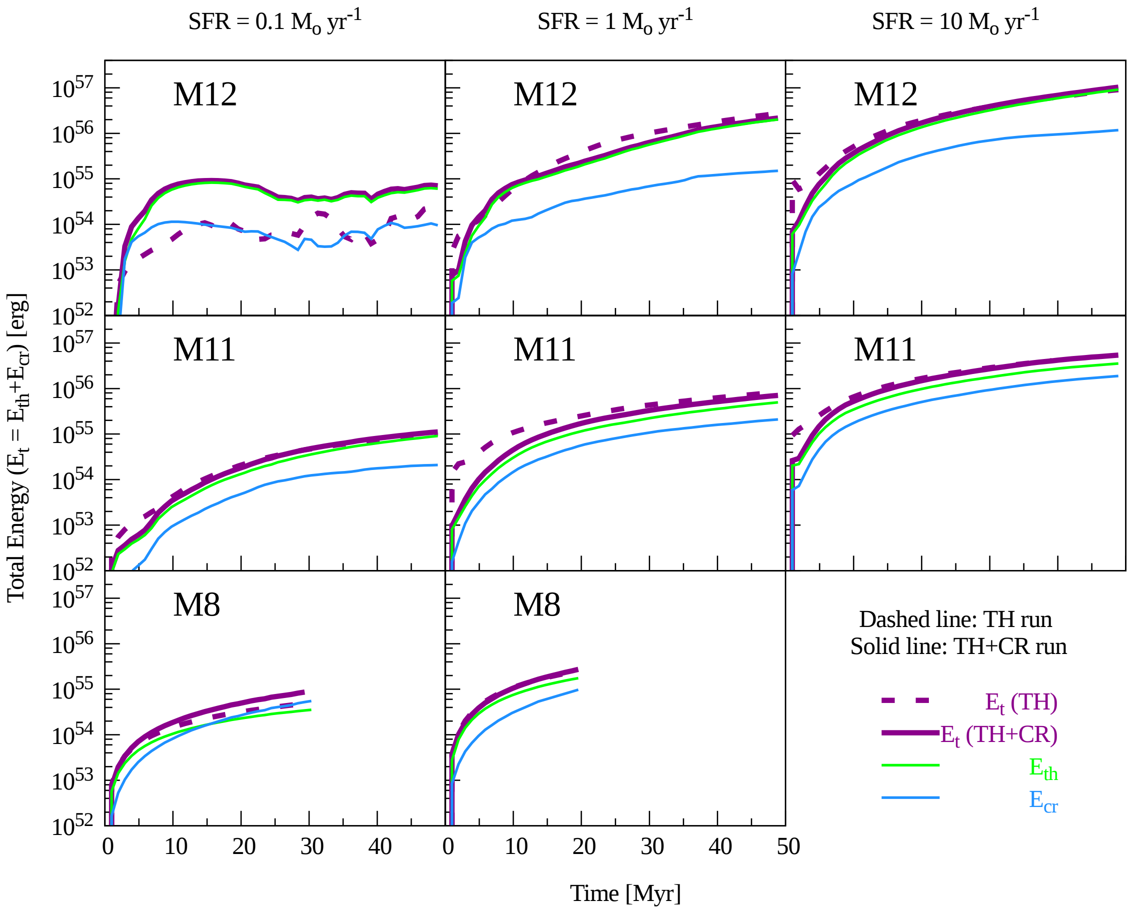

Figure 4.6: Total energy *within* the bubble (region within outer shock) is plotted for the TH (dotted purple lines) and TH+CR runs (solid purple lines) for all the cases. The green and blue solid lines show the thermal and relativistic component respectively in each TH+CR run. Comparing the dashed and solid purple lines we notice that, in most of the cases, the total energy within the bubble becomes slightly less when CRs are included, because CR energy leaks out due to diffusion.

total energy includes the thermal as well as CR energy, i.e. $E_t = E_{th} + E_{cr}$ and we have shown these two components separately. Fig. 4.6 shows that in case of TH+CR run, for most of the cases, CR energy is less than the thermal energy and it is expected since our injection prescription assumes $w = p_{cr}/(p_{th} + p_{cr}) = 0.2$ (i.e., CR energy density fraction $e_{cr}/(e_{th} + e_{cr}) = 2w/(1 + w) = 1/3$). Comparison of total energy (purple curves) between TH and TH+CR runs shows that at early epochs total energy is slightly lower in the case of TH+CR runs, because of CR diffusion. However, this difference decreases as bubbles become larger, because CR diffusion is less effective at larger distances (due to the increase in CR diffusion timescale, which is $\propto (distance)^2$, see e.g. Eq.4.12). For M12 galaxy, SFR = 0.1 $M_\odot$ yr^{-1}, total energy within the bubble is larger in the TH+CR run compared to the purely thermal run because, here, the forward shock is detected at the position of the acoustic wave. As a result, thermal energy contribution from the CGM is also included in this analysis.

For M8 galaxy and SFR = 0.1 $M_\odot$ yr^{-1}, we notice that the CR energy within the bubble increases with time and after a certain time ($\approx$ 20 Myr) it becomes larger than the thermal energy, resulting in an increase of total energy in TH+CR run compared to TH run (purple solid curve above the dashed curve). This is an artifact of boundary effect near the pole for this case, as can be seen in the left column of Fig. 4.4.

4.3.3 Mass loading factor

Mass loading factor (η) is defined as the ratio of the mass outflow rate through a given surface to the SFR at a given epoch. Despite a simple definition, there is disparity between the way mass loading factor is determined in simulations and in observations. One main difference is in the definition of the surface area through which mass outflow rate is calculated. For example, Booth et al. (2013) defined the surface as a plane at 20 kpc above the disk and Jacob et al. (2018) used a cylinder of different radii and of height reaching up to the virial radius. However, observers define the mass outflow rate as $\approx \Omega N\, r\, v\, m_p$, where Ω signifies the total solid angle considered, N is the column density of material along the line of sight, r is a characteristic distance of the location of most of the outflowing material and v is the outflow speed (Heckman et al., 2015). Such differences make it difficult to interpret the results.

In order to compare our results with previous works, we use two different definitions of mass loading factor, as described below.

Outflow rate across a plane

In this case, we estimate the mass outflow rate through a plane parallel to the galactic disk. To calculate the mass loading factor from our simulation, we define three planes at distances $z = 2\,,4$ and 10 kpc above and below the galactic disk of radius[4] $R_p = 15$ kpc for M11 and M12, and $R_p = 5$ kpc for M8. The mass loading factor η has been calculated using,

$$\eta \equiv \frac{\dot{M}_{\rm load}}{\rm SFR} = 2 \times \frac{\left[\int_{R=0}^{R_p} \hat{z}\cdot d\mathbf{A}\, \rho\, v_z\right]}{\rm SFR}\,, \tag{4.13}$$

where $d\mathbf{A} = \hat{z}\, 2\pi R\, dR$ is a differential area element in the plane and v_z is the vertical component of gas velocity. The factor 2 takes into account the contributions in mass flux both above and below the galactic disk.

We show the mass loading factor (η) as a function of time for three different galaxies in Fig. 4.7 by red curves (solid: TH+CR run, dashed: TH run). The curves show that, in the early epochs, η rises to a peak value and thereafter it becomes small. In some cases, it also shows negative values because of infalling gas. The peak(s) in the evolution of η

[4]We have checked that the choice of radius (R_p) does not affect the calculations as long as the extent of the outflowging gas does not exceed this radius. For M8, this constraint restricts our analysis to an epoch beyond which the outflow becomes larger than 5 kpc.

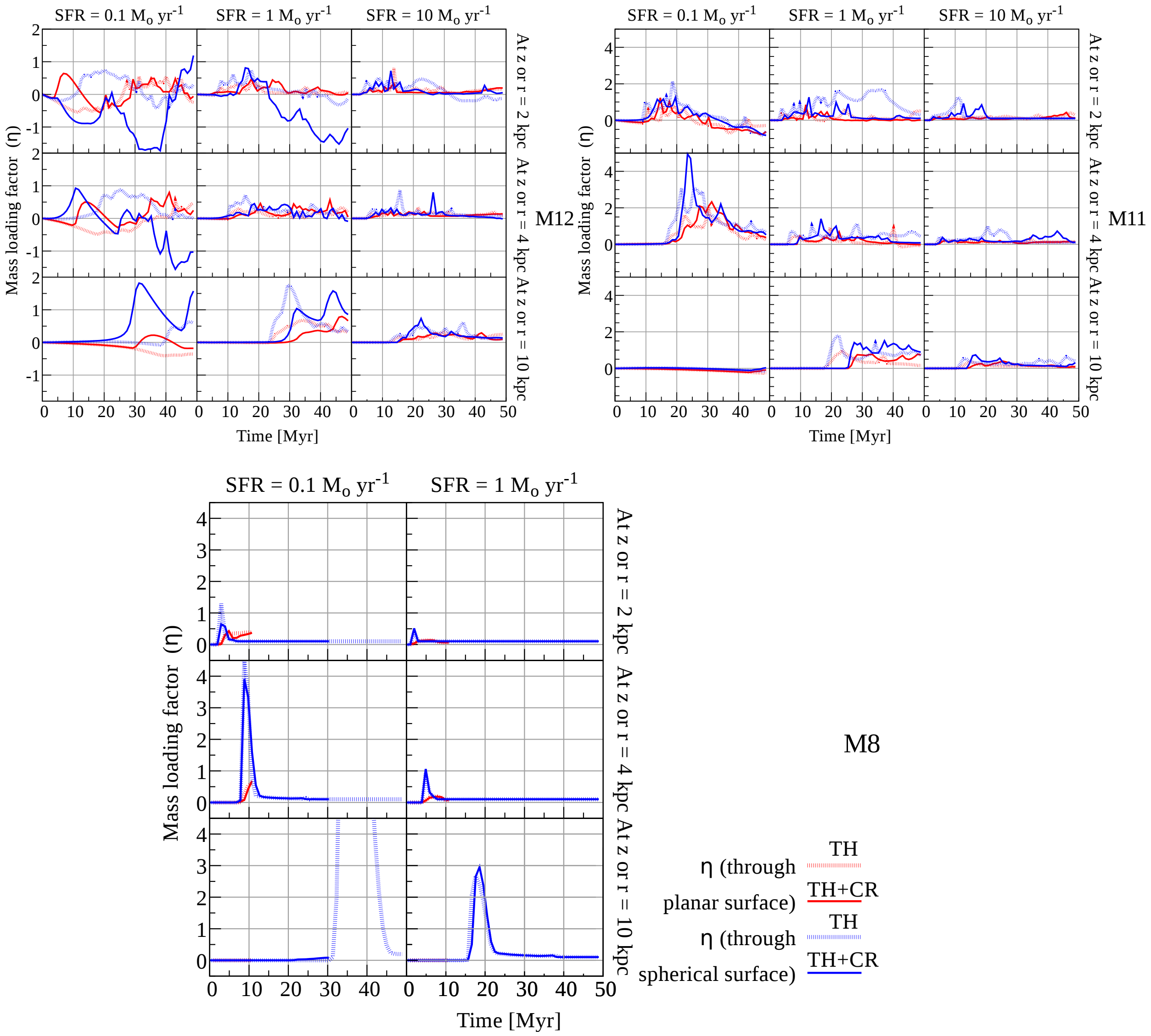

Figure 4.7: Time evolution of mass loading factor (η), calculated in two different ways, are shown for all the cases. The first method (red lines) involves the calculation of mass outflow rate through planes at a height of 2, 4 and 10 kpc from the galactic disk and the second method (blue lines) involves the calculation of mass outflow rate through spherical surfaces at radius 2, 4 and 10 kpc from the center. In each case, the dashed line is for TH runs and the solid lines are for TH+CR runs. We see no significant difference between the dashed and solid lines. Galaxies with higher mass and lower SFR has more negative values of η owing to the infall of gas due to gravity.

is due to the crossing of the swept-up dense shocked gas near the contact discontinuity. After this epoch, the value of $\eta \sim 0.1$, which comes from the gas in the free wind region. In this region, the mass loading factor is $\approx \dot{M}_{\rm inj}/{\rm SFR} \simeq 0.1$ because we have taken $\dot{M}_{\rm inj}$ as 10% of the SFR[5].

Comparing the solid (TH+CR) and dashed (TH) lines, we find no significant difference in the magnitude of η in case of SFR = 1 and 10 $M_\odot$ yr^{-1}. For M12 galaxy, SFR = 0.1 $M_\odot$ yr^{-1}, the time variation of η has a distinct feature for the run with CR, displaying a peak that propagates with time to higher z. This is the signature of the acoustic disturbance already described in the Section 4.3.1.

Outflow across a spherical surface

Next, we estimate the mass outflow rate through a spherical surface of radius r centered at $r = 0$ as,

$$\eta \equiv \frac{\dot{M}_{\rm load}}{\rm SFR} = \frac{4\pi r^2}{\rm SFR} \int_0^{\pi/2} \rho v_r \sin\theta \, d\theta \tag{4.14}$$

where v_r is the radial component of the gas velocity. We show the mass loading factor as a function of time for different galaxies with blue lines (solid: TH+CR run, dashed: TH run, as used earlier) in Fig. 4.7.

The curves show that the evolution of mass loading factors qualitatively remains similar to the planar case (Section 4.3.3). However the peak value in this case is larger than that in the previous case. Since the morphology of the outflowing gas is spherical, considering a spherical surface results in a larger mass outflow rate.

We note that mass loading factor is prominently negative for M12 and SFR =0.1 $M_\odot$ yr^{-1}, for z =2 kpc and r = 2 kpc. One can understand this by considering two relevant speeds, namely, the outflow speed and the escape speed. The outflow speed is roughly 100 km s^{-1}, compared to the circular speed of 150 km s^{-1} of such a galaxy and also the escape speed of the dark matter halo (Fig. 2 of Sharma & Nath 2012). This results in the infall of cold gas clumps produced in the shocked gas layer, producing negative values of η. In other words, galaxies with higher mass and lower SFR are likely to exhibit negative values of η. Fig. 4.7 also shows negative values in some other cases at later times, which essentially comes from the infall of cold clumps produced near the base of the outflow for the Kelvin-Helmholtz instability due to shear.

We notice in Fig. 4.7 that η tends to decrease with increasing SFR, except in the high-mass galaxy low-SFR cases, where η often becomes negative due to the effect of stronger gravity. This effect is most prominent for M8 galaxy where gravity effects are the least. From the analytical solution by Weaver et al. (1977), the position (r) of the outflow at time (t) is estimated as $r \propto (Lt^3/\rho)^{1/5}$ where L is the luminosity of the source and ρ is the density of ambient gas. Hence the velocity (v) of the outflow when it is at distance

[5]We can also analytically estimate the mass loading factor from the self-similar solution, calculating the contribution of the shocked gas (shell) and free wind separately (see Appendix 4.D).

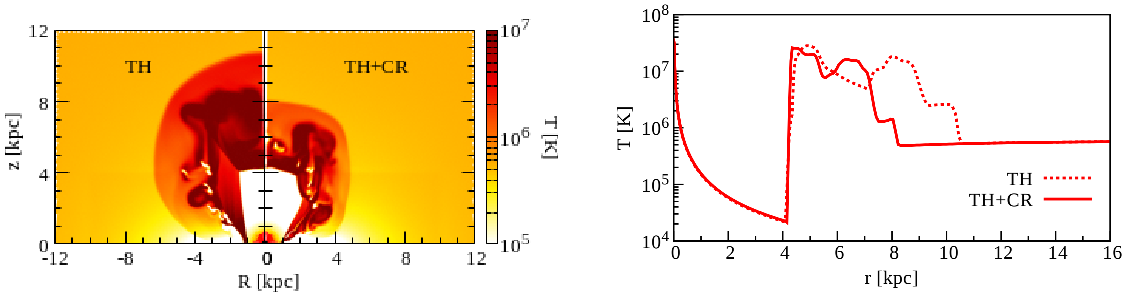

Figure 4.8: For the fiducial case (M11 galaxy, SFR = 1 $M_\odot$ yr^{-1}, Time $\approx$ 20 Myr) both the 2D temperature plot and the 1D temperature profile at $\theta = 20°$ show that shocked CGM in the outflow has a lower temperature when CRs are included compared to purely thermally driven outflow.

r is $v \propto (L/\rho)^{1/3} r^{-2/3}$. The mass outflow rate ($\dot{M}_{\rm out}$) at r would be proportional to the mass swept up by the outflow ($\propto r^3\rho$, does not change with L) and the outflow velocity v. Hence $\eta = (\dot{M}_{\rm out}/{\rm SFR}) \propto L^{-2/3}$ or $\eta \propto {\rm SFR}^{-2/3}$ since SFR is proportional to the source luminosity. The peaks in Fig. 4.7 for M8 galaxy is consistent with this expected scaling.

4.3.4 Temperature distributions

It has been claimed in previous studies that the shocked gas in a CR driven outflow is at a lower temperature compared to a purely thermally driven outflow. Fig. 4.8 shows that for the fiducial case, our simulation results are in accordance with this findings. The temperature of the shocked gas at the outer shock is ~ 1.7 times lower in TH+CR run.

To undestand the role of CRs in multiphase structure of the outflow the temperature distribution of gas has been used in different studies. We study the time evolution of the total mass content in five temperature bins. The temperature bins represent different phases of the gas:

- very cold ($T < 10^4$ K)
- cold (10^4 K $< T < 10^5$ K)
- warm (10^5 K$< T < 10^6$ K)
- hot (10^6 K $< T < 10^7$ K)
- very hot ($T > 10^7$ K)

The time evolution of the total mass in each temperature bin is shown in Fig. 4.9. The curves show that the simulated galaxies M12 and M11 initially have almost negligible gas content in very cold ($T < 10^4$ K) and very hot ($T > 10^7$ K) range. However, the gas mass in these two phases gradually grow with time. The increase in very cold gas content suggests cooling due to adiabatic expansion of gas, whereas the increase in very

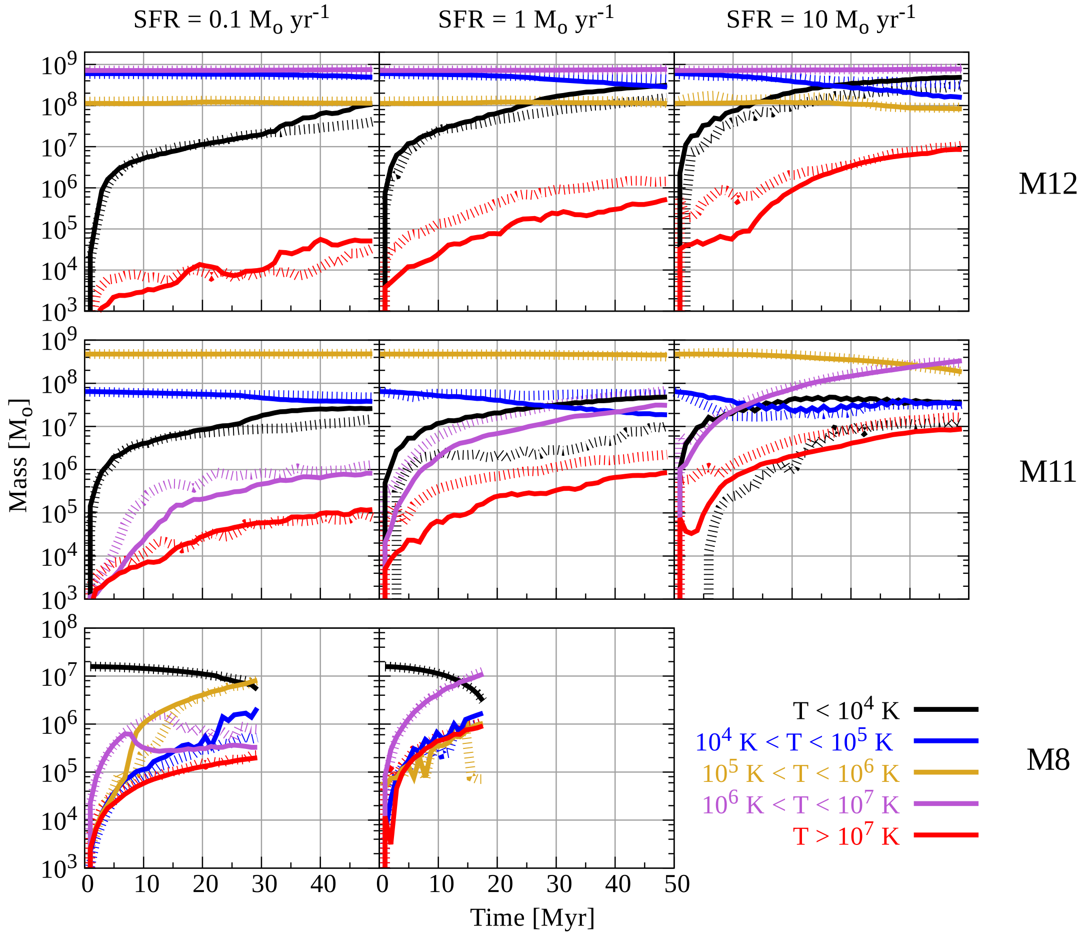

Figure 4.9: Gas mass contained in the simulation box are shown with dashed (TH) and solid (TH + CR) lines of different colours for different temperature ranges. It shows that gradually amount of very cold gas ($T < 10^4$ K) becomes more in the cases where CRs are included, compared to purely thermal models.

hot gas content suggests the increase of mass content in the shocked wind region with time. For M12, the halo gas temperature is 3×10^6 K and for M11 it is 6×10^5 K, and so the gas mass in these bins for the respective galaxies remains almost constant since the maximum contribution in these ranges come from the halo gas. In both M12 and M11, the cold (10^4K$< T < 10^5$K) gas content decreases gradually with time which suggests the mass loss from the disk due to outflow. For M8, since all the gas is initially at 10^4 K, the gas mass in all phases increases with time as expected, except the very cold ($T < 10^4$ K) gas. Comparing the results for runs with and without CRs, we find that the amount of very hot ($> 10^7$ K) gas in TH+CR runs is 2–4 times lower compared to TH runs in both M12 and M11. This is expected from the consideration that a fraction of the total energy in shocked gas is imparted to CRs, thereby reducing the thermal energy density there, consequently reducing the temperature. This has been known since the calculations by Chevalier (1983) for blast and driven waves with cosmic rays, where it was shown that the temperature of the hot gas behind the shock is reduced in the presence of CRs (see also Gupta et al. 2018a). Since a reduction of temperature increases the radiative cooling rate in this temperature range, the presence of CRs also increases cooling and the amount of cold gas. This is borne out by the fact that in our simulation, the amount of very cold ($T < 10^4$ K) gas in TH+CR runs is 2–5 times higher than runs without CRs. This finding of increase of cold gas in the presence of CRs is consistent with previous studies.

To get a better idea of the multiphase structure of the outflow, we show a 2-D probability distribution of gas mass in the simulation box within specified density and temperature bins [$\Delta\log_{10}(\mathrm{T/K}) = 0.1$ and $\Delta\log_{10}(\rho/\mathrm{m_H\,cm^{-3}}) = 0.1$] at $\approx$ 20 Myr in Fig. 4.10. Gas mass in each density and temperature bin has been normalized by the total gas mass within the simulation box. In the initial distribution of M11 galaxy, the bright spot in the low density and high temperature ($\sim 10^6$ K) region represents the hot and tenuous halo gas. The high density and low temperature ($\sim 10^4$ K) region is the signature of the dense and cold disk gas. The gas that falls between these two regions follow a straight line with negative slope (≈ -0.8) in the $\rho - \mathrm{T}$ diagram. This negative slope which approximately follows the power law, $T \propto \rho^{-1}$ indicates that the initial density distribution is in pressure equilibrium[6], as expected for a stable galaxy set-up. For M8 galaxy, such a region is absent in the initial distribution since there does not exist a wide distribution of density as well as temperature. Most of the halo gas has density $\sim 10^{-4} m_{\mathrm{H}}\mathrm{cm}^{-3}$ and temperature $\sim 10^4$ K.

At a later time, at $\approx$ 20 Myr, a fraction of the CGM (halo) gas reaches higher temperature and lower density compared to their initial states, arising from the shocked wind region of the outflow. Another feature to be noticed is that an amount of gas is accumulated towards the bottom right corner of the diagram, i.e., at a high density and low temperature region. This is the shocked gas near the weak outer shock in the disk.

For SFR = 1 and 10 $M_\odot$ yr^{-1}, another interesting aspect is that, for M11 galaxy, there is an accumulation of gas that shows up along a straight line with positive slope in the $\rho - \mathrm{T}$ diagram. This line is a characteristic of adiabatic expansion in the free wind region of the outflow. We do not see this feature for SFR = 0.1 $M_\odot$ yr^{-1} because the wind is not powerful enough and as a result, the outflow may not have a distinct free wind region, as previously shown in Fig. 4.3. However, for M8 galaxy this feature is noticeable even for low SFR because in this case, outflow is strong enough due to weaker gravity of the halo and the absence of a thick disk compared to M11 .

Comparing the results for TH and TH+CR runs for M11, we find that the temperature of the shocked disk gas (right bottom corner) is lower by a factor ~ 2. These results are also valid for M12, albeit these effects are more prominent for M11 galaxy.

[6]The slope is not exactly -1 since gravitational force is also included in setting up the initial hydrostatic equilibrium.

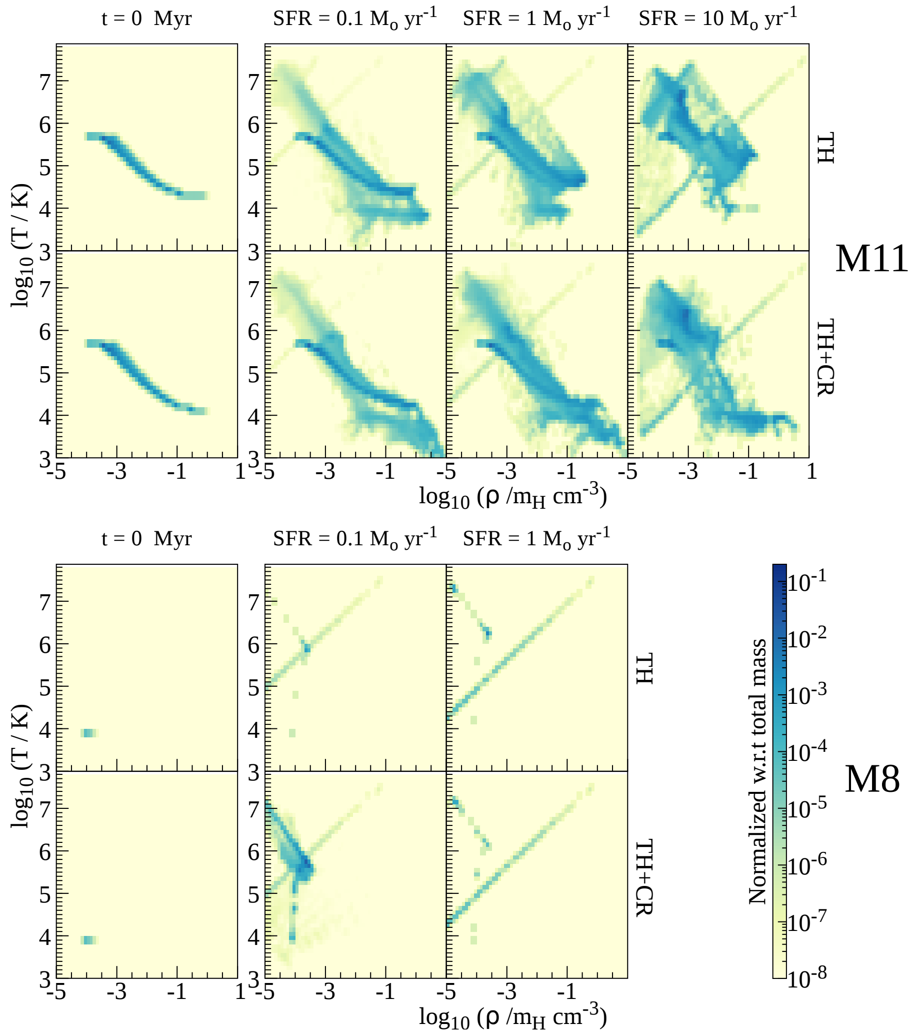

Figure 4.10: The 2-D probability distribution of gas mass fraction (normalized to total mass in the simulation box) within specified density and temperature bins at $\approx$ 20 Myr for M11 and M8 galaxy. The left most columns for each panel show the initial mass probability distribution. This figure suggests enhanced cooling of shocked gas when CRs are included, as indicated by the portions with $T \leq 10^4$ K in TH+CR runs compared to TH runs.

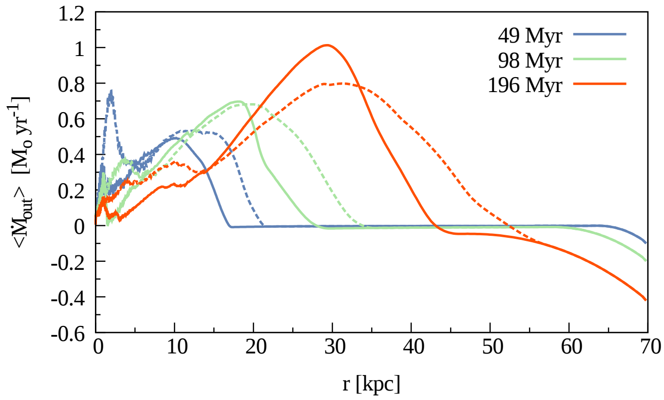

Figure 4.11: Time averaged mass outflow rate, $\langle \dot{M}_{out} \rangle$, as a function of distance for with (solid curves) and without (dashed curves) CR runs. Three colours denote the epoch up to which the time average is done (see Eqn. 4.15). Figure shows that with and without CR runs give a similar evolution of $\langle \dot{M}_{out} \rangle$.

4.4 Effect of long duration outflow evolution

In previous sections, we have presented results by focusing on first $\sim$ 50 Myr of galactic outflows. We would like to emphasize that our idealized simulation in which the star formation is not coupled to any feedback processes is a controlled experiment, and the aim is to determine the role of CRs by comparing our findings with previously published results. In order to understand the long term evolution, we extend the simulation of our fiducial galaxy (M11) until 210 Myr. Since, SFR cannot be kept constant for such a long duration, we consider a period of star formation events with the period being 30 Myr. In other words, star formation is kept uniform between 0–30, 60–90, 120–150, 180–210 Myr, and it is switched off in the intermediate periods. As an alternative to using two different free parameters, we assume the period of star formation and the quiescent period both to be 30 Myr, being motivated by Booth et al. (2013). This allows us to study the structure and evolution of sequential outflows triggered by periods of star formation, which produces numerous shocks.

We find that each star formation event gives rise to a shock structure. The subsequent shocks produced after the first event of star formation, travel faster than the previous shocks since they travel in a comparatively rarefied medium. It can be observed that after sufficient amount of time, the subsequent shocks catch up with the first shock produced. This phenomenon has been previously noticed by Tang & Wang (2005). However, as found in the short duration runs, here also we find that the shocks travel to a shorter distance in the presence of CRs.

4.4.1 Mass loading in the long term evolution

To study the mass loading in the long-duration simulation with periodic star formation, we calculate the time averaged mass outflow rate instead of the previously used mass loading factor. At a particular time (say, $T_{\rm dy}$) we show the time averaged mass outflow rate through each spherical surface of radius r,

$$\begin{aligned} \langle \dot{M}_{out}(r) \rangle &= \frac{1}{T_{\rm dy}} \int_0^{T_{\rm dy}} \dot{M}_{out}(r,t)\, dt \\ &= \frac{4\pi r^2}{T_{\rm dy}} \int_0^{T_{\rm dy}} \int_0^{\pi/2} \rho v_r \, sin\theta \, d\theta \, dt \end{aligned} \tag{4.15}$$

in Fig.4.11. The figure shows that the mass loading gradually increases with time as the outflow progresses outwards and accumulates more mass. After the outflow crosses the region where most of the mass resides within that timecale, the mass outflow rate starts to decline and gradually approaches zero. At large radii, the negative values of mass loading is a numerical artifact, which arises because of the logarithmic grid that makes the radial width of the computational cells large near the outer boundary. We have confirmed that this artifact can be reduced by extending box size, and it does not affect our results.

Comparing the dashed (TH) and solid (TH+CR) curves of Fig.4.11 we note that mass loading is almost independent of whether the outflow is driven by purely thermal gas or a composition of thermal and CR gas. However, we notice that $\langle \dot{M}_{out}(r) \rangle$ has a sharper peak when CRs are considered and at later time, 100 Myr onwards, the peak is slightly higher ($\sim$ 1.3 times) compared to TH case. This analysis justifies our previous results on mass loading and it verifies that the findings are robust as they are also valid in case of multiple star formation episodes in a longer time-scale.

4.4.2 Nature of cold clumps and the role of CR feedback

The long duration simulation with periods of star formation allows us to study the formation of cold clumps due to thermal instability in the presence or absence of CRs. This investigation leads to an important insight to the basic role of CRs in galactic outflows. It has been reported (e.g, Booth et al. 2013; Dashyan & Dubois 2020) that the presence of CRs can produce a greater feedback effect, which has been shown through an increase in the mass loading factor and a suppression of SFR. As we have found that for time-independent SFR, the mass loading does not show a significant difference between TH and TH+CR runs, we need to study the formation of cold clumps in these two cases. The formation of high density and low temperature gas clumps and their infall on the galactic disk can increase the SFR of the galaxy and thereby can decrease the efficiency of feedback.

To illustrate this, we show the snapshot of density and temperature distribution at 156.5 Myr in Figure 4.12, which refers to an epoch of 6.5 Myr after the most recent burst of star formation is over (at 150 Myr). It is seen that numerous cold clumps (with temperature $\sim 10^4$ K) are formed in the TH run, while they are absent in TH+CR run. We can understand the inhibition of clump formation by CRs in the following way. The minimum size of cold clumps is given by $c_{\rm s} t_{\rm cool}$ (McCourt et al., 2018), where $c_{\rm s}$ is the sound speed and $t_{\rm cool}$ is the cooling time of the cold gas. If we consider the cooling time

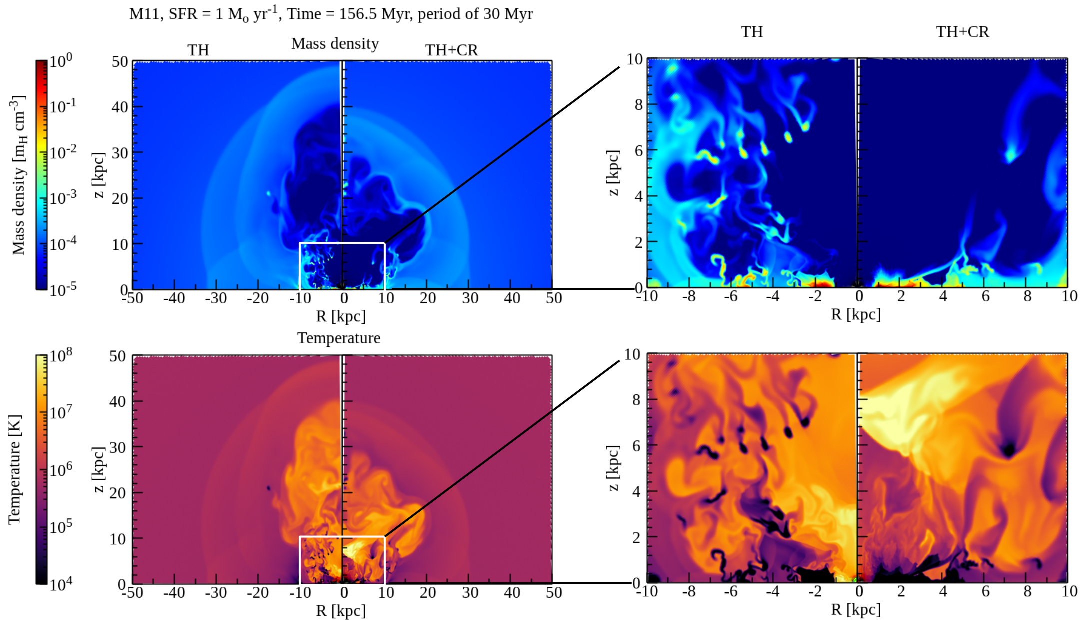

Figure 4.12: Density and temperature distribution of M11 galaxy at 156.5 Myr in the long duration simulation with periodic star formation. The outer shock produced in the first star formation event evolve independently, however the shocks produced in the subsequent star formation events travel in a comparatively rarefied medium and can catch up with the first shock. In the zoomed in version (shown on the right) of the density and temperature distribution one can see *more* high density and low temperature gas clumps in TH case compared to the TH+CR run. (for details, see Section 4.4.2)

of the ambient gas, this will lead to a larger size, but here we are more interested in the *lower limit*. On the other hand, while the gas cools, the diffusion of CRs tries to wash out perturbation unless it is larger than $\geq \sqrt{6D_{\rm cr}t}$, where t corresponds to $t_{\rm cool}$. This is similar to the damping of small perturbation by the streaming of hot dark matter in cosmological context. Therefore the formation and growth of cold clumps requires $c_{\rm s}t_{\rm cool} \geq \sqrt{6D_{\rm cr}t_{\rm cool}}$. This leads to a lower limit on the cooling time scale

$$t_{\rm cool} \geq \frac{6D_{\rm cr}}{c_{\rm s}^2}\,. \tag{4.16}$$

Using $D_{\rm cr} \sim 10^{28}$ cm^2 s^{-1} and the sound speed of a 10^6 K gas ($c_s \sim 10^7$ cm s^{-1}), this gives a lower limit of ~ 20 Myr on the cooling time scale. For a 10^6 K gas with solar metallicity, the cooling rate is $\Lambda_{\rm N} \approx 10^{-22}$ erg cm^3 s^{-1}, and a cooling time scale of 20 Myr implies an upper limit on the clump density $\leq 1.5k_{\rm B}T/\Lambda_{\rm N}t_{\rm cool} = 3\times10^{-3}$ cm^{-3}. The basic point is that in the presence of CR diffusion, clumps can only form with very low density, and they may not have high density contrast with surroundings. Since the period between two bursts of star formation here is 30 Myr, if clouds take a long (≥ 20 Myr) time to form, then they are likely to be crushed and evaporated by the next outgoing shock, instead of raining down on the galaxy. The inhibition of thermal instability in the presence of CR is therefore a likely explanation of the greater feedback effect of CR found in previous works.

In addition to the above effect, we notice that the shape of the free wind region of outflow changes due to diffusion. Left panel of Fig.4.12 shows that the shape of the free wind is more elongated along z direction when the outflow is driven by purely thermal gas. The morphology becomes more flattened or squashed when the effect of CRs is included and the difference is a result of CR diffusion as can also be seen from Fig.4.15. As a result, in TH runs, the contact discontinuity (CD) remains near the free wind region and the wind created by the subsequent star formation episodes hits the CD and it breaks into high density gas clumps. However, due to the flattened nature of the free wind region in CR runs, the CD cannot be hit directly by the wind produced later. Taken all together, it is evident that the CR diffusion inhibits the clump formation either by washing out the small perturbations or by changing the morphology of the outflow. We therefore suggest that suppression of cloud formation due to CRs can reduce the SFR.

4.5 Discussion and Conclusions

With the help of our results from idealized simulations of galaxies of three different halo masses and three different SFRs we have shown that there is no significant effect of CRs in the *dynamics* of galactic outflow, but it alters the temperature distribution of gas. Here we explore the impact of the parameters we have used and compare the results with previous works.

4.5.1 Comparison with previous works

We find that there is no significant difference in the time evolution of mass loading factor between runs with and without CR in all cases. This is in agreement with Fujita & Mac Low (2018), who considered a galaxy of mass $5 \times 10^{12}\ M_\odot$ (although their mass outflow rate includes all mass moving upward with $v_{\rm z,min} = 10$ km s^{-1}). However our result is in partial agreement with Booth et al. (2013), who did not find any significant difference in mass loading factor after the inclusion of CR in Milky Way-sized galaxy, but found a ten-fold increase for a SMC-type (with mass $2\times10^9\ M_\odot$) galaxy. It is, however, not easy to trace the reason for the difference, because the halo gas temperature and density used by them are not mentioned.

One result that is similar to Booth et al. (2013), Salem & Bryan (2014) and Butsky & Quinn (2018) is that we find the multiphase structure of the outflow in both the TH and TH+CR runs, however the amount of very cold gas ($T < 10^4$ K) is more in the models where CRs are included. We have traced the reason of this phenomenon to the reduction of gas temperature in the case of CR, which enhances cooling rate for $T < 10^7$ K.

Our results, however, contradict the analytical results by Samui et al. (2018). They

Table 4.2: Comparison of a few recent studies

Some recent results	Simulation time ($t_{\rm sim}$)	Halo properties	SFR	Mass loading factor (η) with CR	Effect on SFR by CR
Booth et al. (2013)	500 Myr	$M_{\rm halo}$ = 10^{12} &$10^{9} M_{\odot}$ $T_{\rm CGM}$ = NM* $n_{\rm CGM}$ = NM	discrete**	For MW, $\eta \sim 0.5$ for both feedback model. For SMC, η is 10 times higher for CR feedback	For both MW & SMC SFR is more suppressed by CR feedback
Fujita & Mac Low (2018)	2.2 Myr	$M_{\rm halo}$ = 5× $10^{12} M_{\odot}$ $T_{\rm CGM}$ = NM $n_{\rm CGM}$ = NM	continuous	CR pressure initially loads about twice as much mass as thermal pressure alone at blowout, but the mass loading is similar afterwards	feedback is not coupled to SFR, no effect on SFR
Butsky & Quinn (2018)	13 Gyr	$M_{\rm halo}$ = 10^{12} $M_{\odot}$ $T_{\rm CGM}$ = NM $n_{\rm CGM}$ = NM	discrete	CR pressure support lifts thermal gas higher out of the gravitational potential well; no comment on η	higher value of $p_{\rm cr}/p_{\rm th}$ implies more suppression of SFR by CR feedback
Samui et al. (2018)	10 Gyr	$M_{\rm halo}$ = 10^{8--11} $M_{\odot}$ $T_{\rm CGM}$ = $T_{\rm vir}$ $n_{\rm CGM}$ = follows a beta model	analytical	η = 33 for M8 & η = 0.7 for M11 (assumed)	uses a SF model dependent on assumed values of η
Jacob et al. (2018)	6 Gyr	$M_{\rm halo}$ = 10^{10--13} $M_{\odot}$ $T_{\rm CGM}$ = NM $n_{\rm CGM}$ = NM	discrete	$\eta \propto M_{\rm vir}^{-1} - M_{\rm vir}^{-2}$	no comparison with thermal
Dashyan & Dubois (2020)	250 Myr	$M_{\rm halo}$ = 10^{10}&10^{11} $M_{\odot}$ $T_{\rm CGM}$ = 10^{6} K $n_{\rm CGM}$ = 10^{-6} cm^{-3}	discrete	Iso diffusion of CR increases mass loading	reduced by a factor of 2
Hopkins et al. (2020)	14 Gyr	$M_{\rm halo}$ = 10^{9--12} $M_{\odot}$ $T_{\rm CGM}$ = NM $n_{\rm CGM}$ = NM	discrete	volume filling factor of outflow increases, however, the rate of outflow is similar near the disk	suppressed 4 times than thermal where CR pressure dominate
Our Model	50 Myr, 210Myr (for fiducial case)	$M_{\rm halo}$ = $10^{8}, 10^{11}, 10^{12} M_{\odot}$ $T_{\rm CGM}$ = $T_{\rm vir}$ $n_{\rm CGM}$ = $10^{-3} - 10^{-4}$ cm^{-3}	continuous	similar as thermal	feedback is not coupled to SFR, no effect on SFR

$\star\star$ For details see section 4.5.2

suggested that galactic winds driven by CRs travel a larger distance compared to thermally driven winds in massive galaxies. They reported that in a galaxy of mass $\sim 10^8 M_{\odot}$, a steady outflow is possible only with the inclusion of CR since they lose less energy due to adiabatic expansion because of the softer equation of state. However, even in the analytical calculation of blastwaves in the presence of CRs by Chevalier (1983), it was shown that shocks propagate to shorter distances compared to the case of purely thermal gas. Our results are consistent with these theoretical expectations. In Table 4.2 we summarise the differences among some previous works.

4.5.2 Dependence on the choice of SFR

There is a basic difference in the way star formation is implemented in our work and most of the previous works. We assumed that star forms *continuously* in the galactic disk, for the first few Myr with a time-independent SFR, whereas others assume that stars form *discretely* whenever a grid point in their simulation reaches a critical density. Such a grid point is then called a 'star particle'. Each star particle represents an ensemble of stars which follow an initial mass function (IMF). Depending on the IMF, in a given time duration Δt, there will be a number of SNe. For each SNe, they inject 10^{51} erg of energy and thereafter, the density of the grid point is updated accordingly. It can be understood that for the same IMF, a continuous SFR will inject more momentum into the ISM compared to a method where star formation happens discretely in some cells.

In the case of discrete star formation in dense grid points, SFR at a given time is dependent on the SFR at earlier time, which means there is a feedback channel which couples with the SFR. All previous works except Fujita & Mac Low (2018) used discrete star formation with feedback and found that outflows with CRs are more effective for increasing mass loading and suppressing SFR compared to purely thermal outflow. On the other hand we find that CRs do not have any significant effect on the dynamics of the outflowing gas and our result matches with Fujita & Mac Low (2018). This contrast suggests that the result is dependent on the choice of how SFR is implemented in the setup which lead us to the discussion in section 4.4.2.

4.5.3 Choice of CR injection region

In this study, we have injected CRs at the locations of shocks, which differs from most previous studies where a fraction of the total energy is directly injected into CRs at the same location where SNe energy is injected (see e.g., Booth et al. 2013; Salem & Bryan 2014; Butsky & Quinn 2018; Fujita & Mac Low 2018). We find that these two injection methods can affect the morphology of outflowing gas, which is shown in Fig. 4.13. Note that, to distinguish these two methods, we have labelled them by *shock injection* (as described in section 4.2.5) and *central injection* (where 20% of total input energy is injected into CRs within $r_{\rm inj}$). In addition to these two methods, we also show a combined case - central + shock injections.

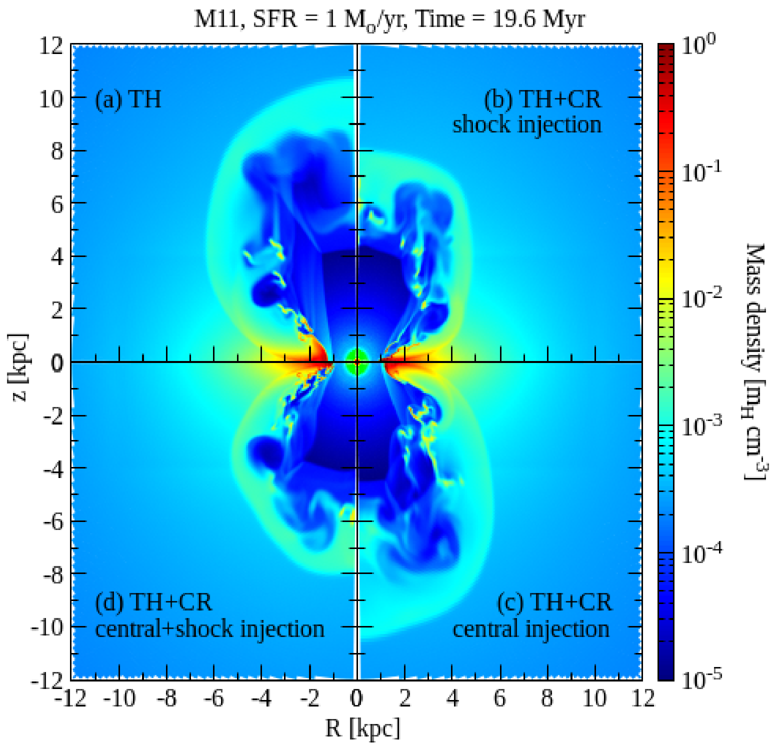

Figure 4.13: The 2-D density plot for the fiducial case (M11, SFR = 1 $M_\odot$ yr^{-1}) at $\approx$ 20 Myr are shown for different CR injection schemes. In the fiducial TH+CR case, CRs are injected as pressure at the shock fronts (shock injection). CRs can also be injected at the centre of the thermal injection region (central injection) or as a combination of both shock and central injection. We see that the dynamical effect of the CRs is to shrink the outer shock in a more pronounced manner when CRs are included at the shock fronts.

Fig. 4.13 shows that outer shock travels a shorter distance in the shock injection case (panel b) compared to the central injection case (panel c). For both cases, the reverse shock is located at a similar location (along z axis, it is located at $\approx$ 4.5 kpc). However, the gas swept-up by outer shock is denser in the shock injection model compared to the central injection model. The reason behind this can be understood as follows.

- In case of shock injection, the CRs are continuously injected at the location of shocks, thereby it maintains a constant CR pressure fraction in the shocked gas region. Whereas in the central injection case, CR energy in the shocked gas evolves with time, and we find that the CR energy is quite high near $r_{\rm inj}$ and also in the shocked wind region, however, it drops gradually near the outer shock (thereby it reduces CR pressure gradient w.r.t. the CGM). It can be seen by comparing solid and dashed blue curves (representing shock and central injections respectively) in Fig. 4.14, which represent the radial distribution of CR pressure fraction at θ = 20°. Therefore, the leakage of CR energy from the outer shocked gas to the halo is more

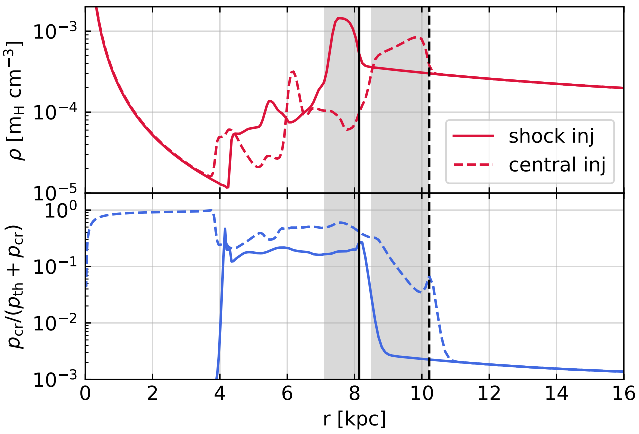

Figure 4.14: For the fiducial case (M11 galaxy, SFR=1 $M_{\odot}$ yr^{-1}, along $\theta = 20°$), density (red curves) and CR pressure fraction ($p_{cr}/(p_{th} + p_{cr})$, blue curves) are shown at $\approx$ 20 Myr in case of shock injection (solid curves) and central injection (dashed curves). The outer shock position in these two cases are marked with two black lines (dashed: central injection, solid: shock injection) and the shocked gas regions are shown by grey shaded area. The density jump at the outer shock is higher in case of shock injection. We also note that $p_{cr}/(p_{th} + p_{cr})$ is less near the outer shock position in the central injection case.

effective in the shock injection case compared to the central injection case.

- Due to efficient CR diffusion in the shock injection case, the shocked gas of the outflow gets compressed to a higher density than the central injection case (compare solid and dashed red curves in Fig. 4.14). This effect also enhances the radiative cooling of the gas, swept-up by outer shock, since the cooling rate of the gas $\propto \rho^2$. As a result, in the shock injection case, the outer shock travels a shoter distance.

Therefore, both CR diffusion and radiative cooling of the gas play a crucial role in determining the location of outer shock.

4.5.4 Dependence on CR diffusion coefficient

To understand the importance of CR diffusion, we show 2-D density plots for M11 galaxy, SFR = 1 $M_{\odot}$ yr^{-1}, at $\approx$ 20 Myr, for three different values of diffusion coefficient (D_{cr}) in Fig. 4.15. We note that the position of the outer shock decreases with increasing D_{cr}. This confirms our explanation that the energy contained within the bubble leaks more with increasing CR diffusion as described in Section 4.3.2. This can also be verified from Fig. 4.15, right panel, where it shows that the CR energy within the bubble decreases for higher value of diffusion coefficient (D_{cr}).

4.5.5 Limitations of our work

- A 3D simulation is more favourable to study the morphology of the outflowing gas, however, it is computationally expensive and a 2D version is unlikely to change the

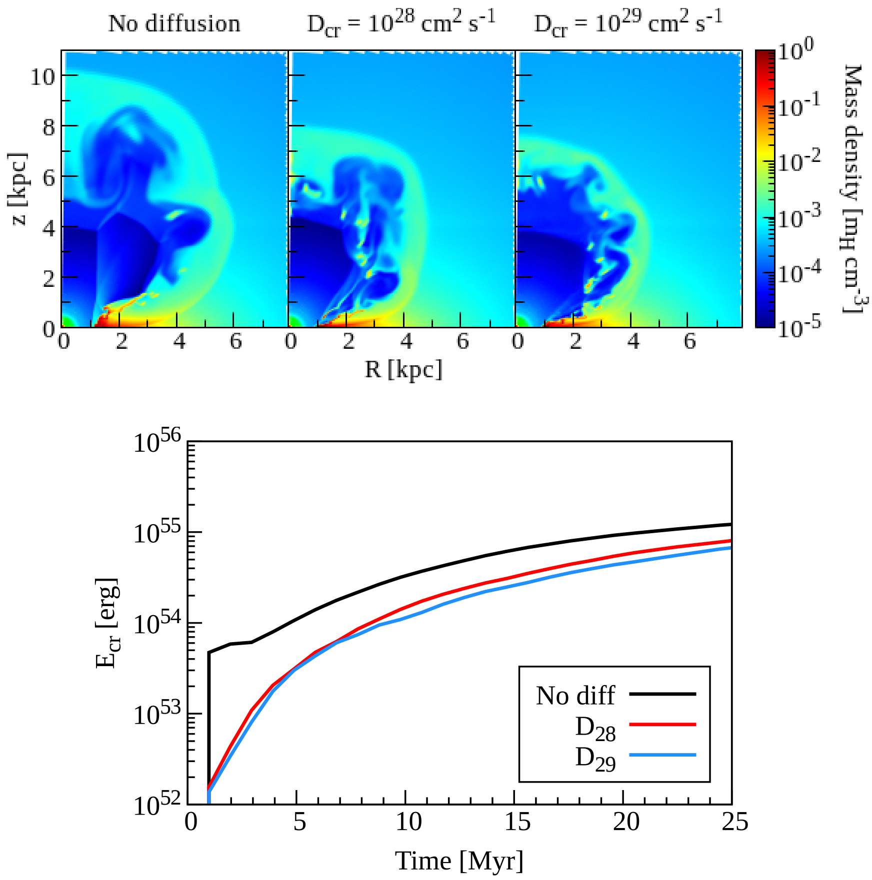

Figure 4.15: Position of outer shock in the 2D density plots at ≈ 20 Myr for M11 galaxy, SFR = 1 $M_\odot$ yr^{-1} including CRs but with different values of CR diffusion coefficients (D_{cr}). It can be seen that the outer shock traverses a shorter distance with increasing values of D_{cr}. In a separate lower panel we also show how CR energy (E_{cr}) within outer shock changes depending upon the value of D_{cr}.

global dynamical features. We would like to point out that Fujita & Mac Low (2018) found that the kinematic behaviour of the outflow in their 3D simulation agrees well with the 2D version (Fujita et al., 2009). Hence it is expected that our results will not change in a more realistic 3D simulation.

- The results described here are valid for our assumption of CR transport mechanism i.e. isotropic diffusion which is a necessary assumption in CR-hydro simulations. When the magnetic field is considered, the effect of CR diffusion is mostly dominated by the choice of the diffusion coefficient parallel to the magnetic field ($k_{||}$) since the diffusion coefficient perpendicular to the magnetic field is much smaller than $k_{||}$. However, given the uncertainty in the value of parallel/perpendicular CR diffusion coefficient, the choice of isotropic diffusion is still a good assumption.

4.6 Summary

We have performed idealized hydrodynamical (HD) simulation of three galaxies with virial mass 10^8, 10^{11} and 10^{12} $M_\odot$ for constant star formation rates 0.1, 1 and 10 $M_\odot$ yr^{-1}. Our aim has been to find the dynamical effects of CRs on galactic scale outflow of gas in the early evolutionary stage ($\leq$ 50 Myr). Hence we have performed two sets of simulations for each case, one, in which thermal pressure alone drives the outflow (TH runs) and another, in which 20% of the total pressure at the shocks is attributed to CRs (TH + CR runs). Comparing these two sets of simulations, our results are summarized as follows:

1. We find that the outflow reaches a shorter distance when CRs are included in the model compared to purely thermally driven outflows. The main reason behind this is the diffusion of CRs out of the bubble (within outer shock, where CR pressure is high, compared to the halo gas outside). We also note that the inclusion of CRs decrease the value of the effective adiabatic index of the combined fluid from 5/3 and from the energy conservation it can be shown that the volume of the outflowing gas is less if it is driven by CR pressure instead of thermal pressure. This result is more prominent for higher mass galaxies and higher SFRs. However, for M8 galaxy, we do not see any difference in the outer shock position between the runs with and without CRs. This is because the speed of outflow in this case is few hundred km s^{-1}, one order of magnitude larger than the escape speed ($\sim$ 10 km/s) of M8 galaxy. The outflow moves so fast that the effect of diffusion is not observed in this case.

2. The mass loading factor (ratio of the mass outflow rate to SFR) has been calculated in two ways, one in which the mass outflow rate is estimated through a plane parallel to the galactic disk (above and below) and another in which it has been calculated through a spherical surface. In both cases, we do not find any significant difference between the mass loading factors in TH and TH+CR cases. This result is valid for all the galaxies for all constant SFRs. However, for higher mass galaxies and lower SFR there is a trend to show a few negative values in the time evolution of the mass loading factor owing to the strong gravitational potential of high mass galaxies.

3. We have studied the distribution of gas in different temperature bins, as well as distribution of gas mass in different density and temperature bins within the simulation box. We find that the amount of cold gas ($\sim 10^4$ K) is more for models which includes CR. This arises from the fact that a part of the thermal energy is attributed to CR energy in TH+CR models, hence the effective temperature of the outflowing gas decreases and increases its radiative cooling rate.

4. We have investigated the long term evolution of the outflow by performing a simulation of the fiducial case (M11 galaxy) for a duartion of 210 Myr with periodic

star formation events. After $\approx$ 160 Myr, we observe that a few high density and low temperature gas clumps form in TH run, which are abesnt in TH+CR. We have identified a possible explanation for the suppression of these clump formation by the diffusive nature of CRs. Our discussion suggets that the formation of these clumps and their infall on the galactic disk can decrease the efficiency of feedback (by enhancing star formation due to the presence of cold clumps) which is reported by previous results.

In a nutshell, we found that CRs do not change the dynamics of the outflowing gas significantly in the early stage of galactic outflow ($\leq$ 50 Myr), however the temperature of the outflowing gas decreases in the presence of CRs. Moreover, the idealized simulation provided us a suitable platform to study the reason behind the higher efficiency of CR driven feedback as reported in earlier works.

4.A Cooling box

The cooling timescale of the gas in the galactic disk is usually shorter than the dynamical timescale that has been considered in this study. If there is no additional physical process to increase the energy of the gas then it would lose its thermal energy as time evolves. In reality, the disk gas is heated by photoionization radiation from stars and its temperature is maintained at $\sim 10^4$ K. In our simulations, since we do not include radiation, we keep the temperature of the disk at $\sim 10^4$ K for all runs. This is achieved by setting a box within which the cooling is allowed only for the the injected material (not the disk or halo gas in that region). In order to choose the width and height of this box, we first estimate the cooling time scale of the gas by using

$$\begin{aligned}\tau_{\rm cool} &= \frac{E_{\rm g}}{n_{\rm i}\, n_{\rm e}\, \Lambda_{\rm N}(T)} \\ &\approx 60\,{\rm Myr}\left(\frac{T}{10^6{\rm K}}\right)\left(\frac{\rho}{10^{-3}\, m_{\rm H}\,{\rm cm}^{-3}}\right)^{-1} \\ &\quad \left(\frac{\Lambda_{\rm N}}{10^{-22}\,{\rm erg\,cm^3\,s^{-1}}}\right)^{-1}\end{aligned} \tag{4.17}$$

where $\Lambda_{\rm N}$ is the normalized cooling rate, T is the gas temperature, and ρ is the gas density. Figure 4.A.1 shows the cooling timescale for M12 and M11 galaxy and also the box within which the cooling of disk or halo gas is not allowed. The size of this box is chosen such that the cooling timescale of the gas beyond the box is longer than our simulation timescale. For the galaxy with mass $10^8\, M_\odot$, the disk is expected to be small and hence we have not considered any box in this case.

4.B CR cooling

In this study, we have not included CR energy loss. CRs can lose energy while interacting with matter. However, the cooling timescale of CRs due to these interactions is longer than the timescale used in our simulations. For example, the cooling timescale of CRs due to hadronic and leptonic interactions (Guo & Oh, 2008) is given by

$$\begin{aligned}\tau^{\rm cr}_{\rm cool} &= \frac{e_{\rm cr}}{7.5\times 10^{-16} n_{\rm H} e_{\rm cr}} \\ &\approx 4\times 10^4{\rm Myr}\left(\frac{\rho}{10^{-3}\,{\rm m_H\,cm^{-3}}}\right)^{-1}\end{aligned} \tag{4.18}$$

which is much longer than our simulation time scale.

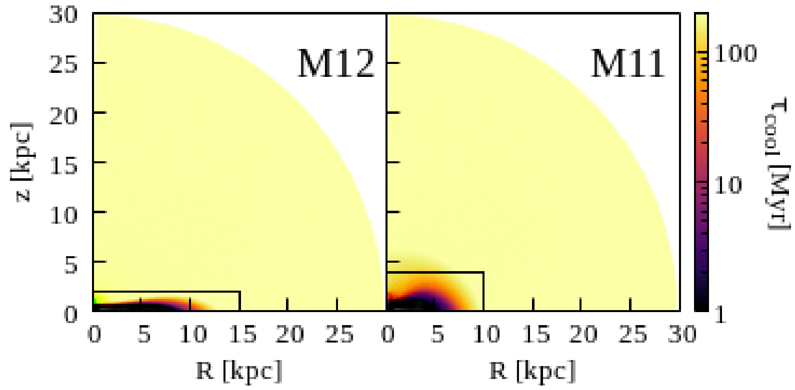

Figure 4.A.1: Cooling timescale of M12 and M11 galaxy. The black outlined box shows the region where radiative cooling of the injected gas is only allowed, for details see Appendix 4.A.

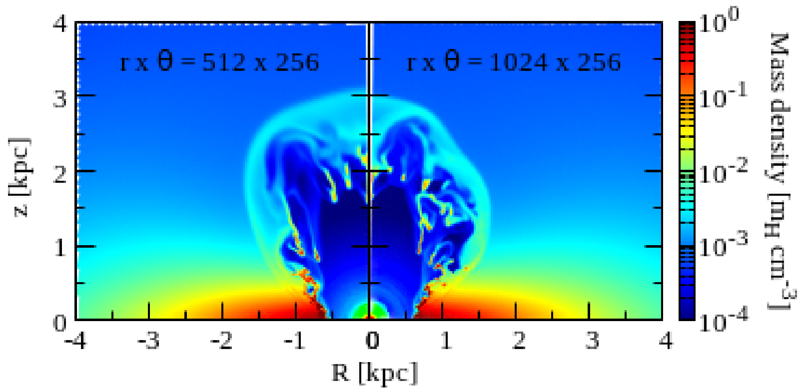

Figure 4.C.1: The 2D density plots for M11 galaxy, SFR = 1 $M_\odot$ yr^{-1} at ≈ 7 Myr show no significant difference in our fiducial resolution and a higher resolution (see text for details) considered.

4.C Convergence test

The resolution used in all our simulations is described in Section 4.2.3. We performed a high resolution run for our fiducial case (M11 galaxy, SFR = 1 $M_\odot$ yr^{-1}, at ≈ 7 Myr). For this particular run, we use 1024 grid points along r direction and 256 grid points along θ direction. We do not find any qualitative difference between the results of these two runs. This confirms that the resolution used in this study is adequate for the purpose.

4.D Analytical estimation of mass loading factor

In this section, we analytically estimate the mass loading factor for the planar case. For this we choose a plane parallel to galactic disk (as discussed in Section 4.3.3) at a height of z kpc both above and below the disk. The net mass outflow rate can be considered as the sum of the gas mass flowing out through the shocked CGM (hereafter shell; $\dot{M}_{\rm shell}$) and

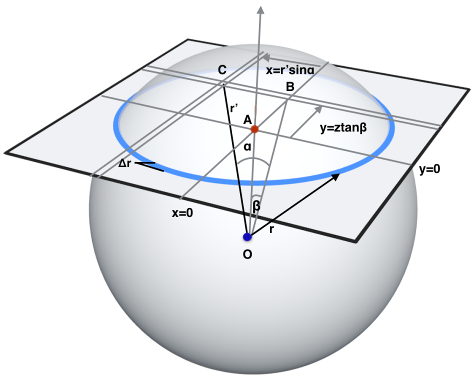

Figure 4.D.1: Schematic diagram for estimating mass loading factor analytically.

the shocked wind region ($\dot{M}_{\rm wind}$). The mass flux carried by the shell can be estimated as

$$\begin{aligned} \dot{M}_{\rm shell} &= 2\pi r sin\theta \Delta r \rho_{\rm sh} v_{\rm z} \\ &= 2\pi \rho_{\rm sh} v_{\rm r} z \Delta r \sqrt{1-\frac{z^2}{r^2}} \end{aligned} \tag{4.19}$$

where r is the position of forward shock and $v_{\rm z}$ is the z component of the gas velocity, which can be written as $v_{\rm z} = v_{\rm r} cos\theta = v_{\rm r}(\frac{z}{r})$. Here, $\rho_{\rm sh}$ is the gas density of the shell which is taken to be 4 times the ambient gas density assuming strong shock condition. Δr is the width of the shell.

Next, to calculate the mass flux carried by the shocked wind, we define the planar surface to be an integration of differential area elements dx and dy. Following the geometry shown in the schematic diagram (Fig. 4.D.1), $x = OB \tan\alpha = \frac{z}{\cos\beta}\tan\alpha$ and $y = z\tan\beta$. We also have $\frac{z}{r'} = \cos\alpha\cos\beta$, since in triangle COB, $\cos\alpha = OB/r'$, and in triangle OAB, $OB = (\cos\beta/z)$. Therefore $dx = (z/\cos\beta)\sec^2\alpha d\alpha$ and $dy = z\sec^2\beta d\beta$. Also, $v_z = v_r\cos\alpha\cos\beta$. Hence the mass flux carried by the wind is given by

$$\begin{aligned} \dot{M}_{\rm wind} &= \int\int \rho_{\rm w}(r') v_z dx dy \\ &= 2\times 2\times \frac{\dot{M}_{\rm inj}}{4\pi}\int_{\alpha=0}^{\alpha=\cos^{-1}\frac{z}{r\cos\beta}}\int_{\beta=0}^{\cos^{-1}\frac{z}{r}} \\ &\quad \frac{\cos\alpha\cos\beta}{(r')^2}\left(\frac{z}{\cos\beta}sec^2\alpha\right)\left(z\sec^2\beta\right)d\alpha d\beta \\ &= \frac{\dot{M}_{\rm inj}}{\pi}\int_{\beta=0}^{\cos^{-1}\frac{z}{r}} d\beta\int_{\alpha=0}^{\alpha=\cos^{-1}\frac{z}{r\cos\beta}}\cos\alpha d\alpha \\ &= \frac{\dot{M}_{\rm inj}}{\pi}\int \sin\left(\cos^{-1}\frac{z}{r\cos\beta}\right)d\beta \\ &= \frac{\dot{M}_{\rm inj}}{\pi}\int_{\beta=0}^{\cos^{-1}\frac{z}{r}}\sqrt{1-\frac{z^2}{r^2\cos^2\beta}}\,,d\beta \qquad r\geq z \end{aligned}$$

$$
\begin{aligned}
&= \frac{\dot{M}_{\rm inj}}{\pi}\Big[\tan^{-1}\Big(\frac{\frac{r}{z}\tan\beta}{\sqrt{\frac{r^2}{z^2}-1}\sqrt{1-\frac{\tan^2\beta}{\frac{r^2}{z^2}-1}}}\Big)\Big|_0^{\cos^{-1}\frac{z}{r}} \\
&\qquad -\frac{z}{r}\sin^{-1}\Big(\frac{\tan\beta}{\sqrt{\frac{r^2}{z^2}-1}}\Big)\Big|_0^{\cos^{-1}\frac{z}{r}}\Big] \\
&= \frac{\dot{M}_{\rm inj}}{\pi}\Big[[\frac{\pi}{2}-0]-\frac{z}{r}\sin^{-1}\Big(\frac{\frac{z}{r}\tan(\cos^{-1}\frac{z}{r})}{\sqrt{1-\frac{z^2}{r^2}}}\Big)\Big] \\
&= \frac{\dot{M}_{\rm inj}}{\pi}\Big[[\frac{\pi}{2}-0]-\frac{z}{r}\sin^{-1}\Big(\frac{\sqrt{\frac{r^2}{z^2}-1}}{\sqrt{\frac{r^2}{z^2}-1}}\Big)\Big] \\
&= \frac{\dot{M}_{\rm inj}}{2}\Big(1-\frac{z}{r}\Big)
\end{aligned}
\tag{4.20}
$$

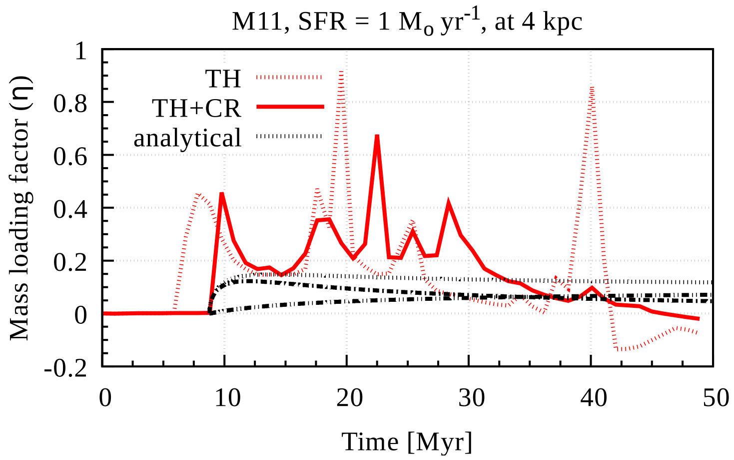

Figure 4.D.2: Comparison of mass loading factor for M11 galaxy, SFR = 1 $M_\odot$ yr^{-1} between our simulation (red curves) and analytic method (black curves). The dash-dotted and dash-dot-dotted curves show mass loading by the shocked gas ($\dot{M}_{\rm shell}$; see Eq. 4.19) and by the wind ($\dot{M}_{\rm wind}$, see Eq. 4.20) respectively, and the black dotted curve represents the total mass loading factor when the outflow reaches 4 kpc. In the early evolutions, the dash-dot-dotted curve is below the dash-dotted curve because wind is less denser compared to shocked-CGM gas until the shell exceeds 4 kpc. The red dashed (TH) and solid (TH+CR) curves show the mass loading factor calculated from simulation at a height z = 4 kpc.

A comparison of analytically estimated mass loading factor with our simulation for M11 galaxy (SFR = 1 $M_\odot$ yr^{-1}) is shown in Figure 4.D.2. The curves show that the time evolution of mass loading factor in our simulation is qualitatively similar to the above analytic estimates, albeit with some noticeable differences. This is due to various assumptions in our analytic calculation, e.g., the morphology of the outflowing gas (which is assumed as spherical) and shock jump condition. Moreover, the formation of cold clumps may increase the mass loading factor and it is difficult to include all these in analytical calculations self-consistently.

5

Concluding remarks

5.1 Summary

In this thesis we have studied various interactions between galaxy and its surrounding medium that occur through high energy particles called cosmic rays. The results presented in this thesis are divided into three chapters. In the first part we have studied the nature of cosmic ray heating around galaxies. We have also studied the impact of this heating at very high redshift ($z \sim 20$) arising from supernova explosion of population III stars. In the second part we have studied the interaction of cosmic ray electrons accelerated in pop III supernova explosions with the intergalactic medium (IGM) magnetic field. This interaction gives rise to synchrotron emission in the radio band. This high redshift radio background and IGM heating both modify the depth of the absorption trough in the 21 cm global signal from the beginning of the epoch of reionization. In the third part we studied the importance of cosmic rays in driving galactic scale outflowing gas through hydrodynamical simulations.

5.1.1 Cosmic ray heating of heating of IGM

Cosmic rays or high energy particles are accelerated in the star forming region of the galaxy. These particles diffuse out of the galaxies and interact with the IGM gas through *Coulomb interaction*. By this process, they lose a large fraction of their energy which eventually increases the IGM temperature. This interaction is being studied recently in light of preheating of the Universe in the beginning of Epoch of Reionization (EOR). The global 21 cm signal, which is an important probe of EOR, directly depends on the deviation of the HI spin temperature from that of the cosmic microwave background (CMB). The spin temperature is modified by the kinetic temperature of IGM filling the early Universe. We found that for the predicted distribution of galaxies at high redshift from ΛCDM cosmology and typical values of diffusion coefficient, the increase in IGM temperature is not concentrated around the galaxies. We believe that future observations of global 21 cm radiation will shed more light on this inevitable physical process.

Another significant result from our study is that the increased temperature around the galaxies can inhibit the cosmological gas accretion. As a result, the star formation rate of the galaxy will get suppressed. Hence cosmic ray heating of IGM not only modifies the global 21 cm radiation but also plays a crucial role in the galactic evolution.

5.1.2 Importance of radio background

In the wake of the first ever detection of global 21 cm signal from 'cosmic-dawn' by the EDGES group, there was a concern regarding the depth of the absorption trough which was larger than expected and could not be explained by the standard ΛCDM cosmological models. There were numerous follow up works trying to explain the trough using high redshift radio backgrounds, dark matter particles and various other exotic physics.

Instead of trying to *explain* the EDGES results, we put a limit on the depth of the absorption trough considering two astrophysical processes – i) radio background from population III stars and ii) cosmic ray heating of high redshift IGM. At $z \sim 20$ the first generation of stars were born in dark matter mini-halos of mass $10^{5-7} M_{\odot}$. Within a few Myr most of them exploded in such powerful supernova explosions that they destroyed their host halos. The high energy cosmic ray electrons accelerated in these explosion sites interacted with the intergalactic medium (IGM) gas and gave rise to synchrotron emission. As a result, a uniform radio background was formed which can increase the absorption trough depth. The resulting radio background from this process was found to be substantial enough to explain the EDGES result. However, the cosmic ray protons which were also accelerated at the same time were capable of increasing the temperature of the IGM which can potentially decrease the depth of the trough. The two competing processes — *the production of the radio background and the heating of IGM* — determine the depth of the trough in 21 cm brightness temperature. We showed that the differential brightness temperature at the trough cannot be greater than ~ 0.25 K, which can be tested in future experiments.

5.1.3 Role of cosmic rays in galactic outflows

The process of star formation in galaxies often lead to gaseous outflows. Understanding these galactic scale outflows is important because they play a significant role in galactic evolution. Thermal pressure due to shock heating of the interstellar medium (ISM) has been the focus of most previous studies. The effect of non-thermal pressure components, such as radiation coming out from young stars and cosmic rays (CRs) have also been suggested as important driving mechanisms. However, their effects have mostly been studied in large cosmological simulations.

The perks of doing an idealized simulation is that it allows us to distinguish the role of individual physical processes separately, which can be extended in a more realistic scenario. With the help of a simple *idealized hydrodynamical* simulation, we tried to understand how CRs play a role to launch the outflow and later how CRs impact its dynamics and morphology. To study the importance of various parameters, we performed simulations for three different galaxies of halo masses: 10^8, 10^{11} and $10^{12} M_{\odot}$, and three constant star formation rates (SFRs). We study the outer shock position, mass loading factor and density-temperature distribution of the outflowing gas. We suggest that at early stages of evolution, ($\lesssim$ 50 Myr, a typical lifetime over which a star of mass $> 8M_{\odot}$ explode as type II supernova) when constant SFR is a justified assumption, the dynamical effects of CRs may not be as important as previously claimed, rather it can reduce the size of the outflow in most of the cases due to CR diffusion and the decrease in the effective adiabatic index.

5.2 Future Work

The projects presented in this thesis has opened up many possibilities for future investigations.

In chapters 2 and 3 we have studied the interaction between galaxies and intergalactic medium through *cosmic ray heating* and the emission of *synchrotron radiation* respectively. We have used analytical models to show that these interactions at high redshift through charged particles can leave an impact on the intergalactic medium which can be tested through global 21 cm signal. Hence our previous study focusing on the effects of high-redshift radio background from population III stars on 21 cm global signal, demands to be pursued further through simulations. The limitation of the *analytical* work was the assumption of Lyman-α coupling as an instantaneous event, which is shown by a sudden drop in 21 cm differential brightness temperature. Details *radiative transfer modeling* can replace this sudden jump by a smooth absorption profile.

In the cosmological simulation set-up, after identifying the mini-halos (the birth-places of pop III stars) we can simulate the pop III supernova explosions taking into account the initial mass function of the stars. As the pop III SNe starts to occur in different galaxies, Lyman alpha coupling and synchrotron radio emission will come into play. Then we can determine the brightness temperature along different lines of sight and produce a simulated sky-map of the brightness temperature which will be helpful for the future global 21 cm observations.

In chapter 4, we studied the effect of cosmic rays on the dynamics of galactic outflows. We noticed the presence of gas clumps in the outflowing gas when the outflow was purely thermally driven. The formation and stability of gas clumps is a critical part of gas dynamics study in galaxies. These clumps have a higher density and lower temperature than the ambient medium. The clumps are formed via condensation due to thermal instabilities in the galactic outflow as well as the circumgalactic gas. From the studies of intra-cluster medium, it is known that the gas can be condensed if locally, the ratio of cooling time to free fall time, $t_{\rm cool}/t_{\rm ff} \lesssim 10$. Alternatively, they can be uplifted from the galactic disk where the gas density is higher. After the formation, the clumps are either carried away by the ram pressure of the outflow or get crushed by subsequent shock waves. They can also rain down to the galactic disk. The fate of these clumps is directly linked to the star formation of the galaxy, depending on whether they are adding or driving away more gas mass from the star forming region. Another significant role played by the clumps in galactic evolution is by providing the CGM gas a multiphase structure.

We had noticed that the number of gas clumps decrease significantly in the presence of cosmic rays. We tried to understand this with cosmic ray diffusion inhibiting the clump formation, however the presence of cosmic ray pressure can also have an effect. In the complex set up of a galaxy, it is very difficult to study the role of cosmic rays in the stability of gas clumps. This problem needs to be explored by building a simple set-up of a 3D Cartesian box with uniform density and temperature and a gas clump at the center and then study the stability of the clump in presence and absence of cosmic rays.

Moreover, the galaxy-IGM interactions discussed in this thesis can be extended to the circumgalactic medium. Recently the effect of cosmic rays on the CGM has received attention. There are evidences that support a cosmic ray dominated galactic halo. Cosmic rays can change the density and temperature distribution of the diffuse gas in the galactic halo. As a result, they change the ionization structure of the CGM which can be probed through quasar absorption studies. Not only that, the presence of cosmic rays are also capable of modifying the thermal instability of the CGM gas. Cosmic rays in CGM is a growing field and the analytical models developed in this thesis for galaxy-IGM interactions will be useful in the study of CGM as well.

References

Ackermann M., et al., 2015, ApJ, 799, 86

Agertz O., Kravtsov A. V., Leitner S. N., Gnedin N. Y., 2013, ApJ, 770, 25

Armillotta L., Fraternali F., Werk J. K., Prochaska J. X., Marinacci F., 2017, MNRAS, 470, 114

Barkana R., 2018, Nature, 555, 71

Barkana R., Loeb A., 2001, Phys. Rep., 349, 125

Barkana R., Outmezguine N. J., Redigol D., Volansky T., 2018, Phys. Rev. D, 98, 103005

Behroozi P. S., Conroy C., Wechsler R. H., 2010, ApJ, 717, 379

Bell A. R., 1978, MNRAS, 182, 147

Bell A. R., 2013, Astroparticle Physics, 43, 56

Bell A. R., Lucek S. G., 2001, MNRAS, 321, 433

Benson A. J., Bower R. G., Frenk C. S., White S. D. M., 2000, MNRAS, 314, 557

Benson A. J., Bower R. G., Frenk C. S., Lacey C. G., Baugh C. M., Cole S., 2003, ApJ, 599, 38

Berezinsky V., Blasi P., 2012, Phys. Rev. D, 85, 123003

Berlin A., Hooper D., Krnjaic G., McDermott S. D., 2018, Phys. Rev. Lett., 121, 011102

Biermann P., 1986, Zenit, 13, 14

Biermann P. L., Kusenko A., 2006, Phys. Rev. Lett., 96, 091301

Biermann P. L., Nath B. B., Caramete L. I., Harms B. C., Stanev T., Becker Tjus J., 2014, MNRAS, 441, 1147

Biermann P. L., et al., 2018, Advances in Space Research, 62, 2773

Birnboim Y., Dekel A., 2003, MNRAS, 345, 349

Bisnovatyi-Kogan G. S., Ruzmaikin A. A., Syunyaev R. A., 1973, Soviet Ast., 17, 137

Blanc G. A., Lu Y., Benson A., Katsianis A., Barraza M., 2019, ApJ, 877, 6

Booth C. M., Agertz O., Kravtsov A. V., Gnedin N. Y., 2013, ApJ, 777, L16

Bower R. G., Benson A. J., Malbon R., Helly J. C., Frenk C. S., Baugh C. M., Cole S., Lacey C. G., 2006, MNRAS, 370, 645

Bowman J. D., Rogers A. E. E., Monsalve R. A., Mozdzen T. J., Mahesh N., 2018, Nature, 555, 67

Breitschwerdt D., McKenzie J. F., Voelk H. J., 1991, A&A, 245, 79

Bressan A., Chiosi C., Fagotto F., 1994, ApJS, 94, 63

Bromm V., Yoshida N., Hernquist L., McKee C. F., 2009, Nature, 459, 49

Butsky I. S., Quinn T. R., 2018, ApJ, 868, 108

Butsky I. S., Fielding D. B., Hayward C. C., Hummels C. B., Quinn T. R., Werk J. K., 2020, ApJ, 903, 77

Caprioli D., Spitkovsky A., 2014, ApJ, 783, 91

Chevalier R. A., 1983, ApJ, 272, 765

Chiappini C., 2009, The chemical evolution of the Galactic thick and thin disks. pp 191–196, doi:10.1017/S1743921308027580

Chiappini C., Matteucci F., Gratton R., 1997, ApJ, 477, 765

Condon J. J., et al., 2012, ApJ, 758, 23

Couchman H. M. P., Rees M. J., 1986, MNRAS, 221, 53

Dashyan G., Dubois Y., 2020, arXiv e-prints, p. arXiv:2003.09900

Davé R., Rafieferantsoa M. H., Thompson R. J., Hopkins P. F., 2017, MNRAS, 467, 115

Davé R., Anglés-Alcázar D., Narayanan D., Li Q., Rafieferantsoa M. H., Appleby S., 2019, MNRAS, 486, 2827

Dekel A., Silk J., 1986, ApJ, 303, 39

Dowell J., Taylor G. B., 2018, ApJ, 858, L9

Draine B. T., 2011, ApJ, 732, 100

Drury L. O., Voelk J. H., 1981, ApJ, 248, 344

Dubois Y., et al., 2020, arXiv e-prints, p. arXiv:2009.10578

Efstathiou G., 1992, MNRAS, 256, 43P

Efstathiou G., 2000, MNRAS, 317, 697

Eufrasio R. T., Dwek E., Arendt R. G., de Mello D. F., Gadotti D. A., Urrutia-Viscarra F., Mendes de Oliveira C., Benford D. J., 2014, ApJ, 795, 89

Everett J. E., Zweibel E. G., Benjamin R. A., McCammon D., Rocks L., Gallagher III J. S., 2008, ApJ, 674, 258

Ewall-Wice A., Chang T. C., Lazio J., Doré O., Seiffert M., Monsalve R. A., 2018, ApJ, 868, 63

Fardal M. A., Katz N., Gardner J. P., Hernquist L., Weinberg D. H., Davé R., 2001, ApJ, 562, 605

Feng C., Holder G., 2018, ApJ, 858, L17

Fenner Y., Gibson B. K., 2003, Galactic Chemical Evolution: The Solar Neighborhood. p. 237, doi:10.1007/978-94-010-0115-1_43

Fermi E., 1949, Phys. Rev., 75, 1169

Fixsen D. J., et al., 2011, ApJ, 734, 5

Fujita A., Mac Low M.-M., 2018, MNRAS, 477, 531

Fujita A., Martin C. L., Mac Low M.-M., New K. C. B., Weaver R., 2009, ApJ, 698, 693

Fukugita M., Peebles P. J. E., 2004, ApJ, 616, 643

Genzel R., et al., 2010, MNRAS, 407, 2091

Ginzburg V. L., Ozernoi L. M., 1966, Soviet Ast., 9, 726

Girichidis P., et al., 2016, MNRAS, 456, 3432

Goerdt T., Ceverino D., 2015, MNRAS, 450, 3359

Gronke M., Oh S. P., 2020, MNRAS, 492, 1970

Gunn J. E., Peterson B. A., 1965, ApJ, 142, 1633

Guo F., Oh S. P., 2008, MNRAS, 384, 251

Gupta S., Nath B. B., Sharma P., Eichler D., 2018a, MNRAS, 473, 1537

Gupta S., Nath B. B., Sharma P., 2018b, MNRAS, 479, 5220

Gupta S., Sharma P., Mignone A., 2019, arXiv e-prints, p. arXiv:1906.07200

Haiman Z., Thoul A. A., Loeb A., 1996, ApJ, 464, 523

Hanasz M., Lesch H., 2003, A&A, 412, 331

Heckman T. M., et al., 2011, ApJ, 730, 5

Heckman T. M., Alexandroff R. M., Borthakur S., Overzier R., Leitherer C., 2015, ApJ, 809, 147

Heger A., Woosley S. E., 2002, ApJ, 567, 532

Heger A., Woosley S. E., 2010, ApJ, 724, 341

Henry R. B. C., Worthey G., 1999, PASP, 111, 919

Hills R., Kulkarni G., Meerburg P. D., Puchwein E., 2018, Nature, 564, E32

Hirano S., Hosokawa T., Yoshida N., Umeda H., Omukai K., Chiaki G., Yorke H. W., 2014, ApJ, 781, 60

Holmberg E., 1958, Meddelanden fran Lunds Astronomiska Observatorium Serie II, 136, 1

Hopkins P. F., Quataert E., Murray N., 2012, MNRAS, 421, 3522

Hubble E. P., 1929, ApJ, 69, 103

Hui L., Gnedin N. Y., 1997, MNRAS, 292, 27

Ipavich F. M., 1975, ApJ, 196, 107

Jacob S., Pakmor R., Simpson C. M., Springel V., Pfrommer C., 2018, MNRAS, 475, 570

Johnson J. L., Khochfar S., 2011, ApJ, 743, 126

Kennicutt Robert C. J., 1989, ApJ, 344, 685

Kereš D., Katz N., Weinberg D. H., Davé R., 2005, MNRAS, 363, 2

Kitayama T., Yoshida N., 2005, ApJ, 630, 675

Kormendy J., 1977, ApJ, 218, 333

Kronberg P. P., 1994, Reports on Progress in Physics, 57, 325

Krumholz M. R., Thompson T. A., 2012, ApJ, 760, 155

Krumholz M. R., Dekel A., McKee C. F., 2012, ApJ, 745, 69

Kulsrud R., Pearce W. P., 1969, ApJ, 156, 445

Lacki B. C., 2015, MNRAS, 448, L20

Lehnert M. D., van Driel W., Le Tiran L., Di Matteo P., Haywood M., 2015, A&A, 577, A112

Leite N., Evoli C., D'Angelo M., Ciardi B., Sigl G., Ferrara A., 2017, MNRAS, 469, 416

Lucek S. G., Bell A. R., 2000, MNRAS, 314, 65

Lynds R., 1971, ApJ, 164, L73

Madau P., 2000, arXiv e-prints, pp astro–ph/0005106

Mannheim K., Schlickeiser R., 1994, A&A, 286, 983

Martizzi D., Fielding D., Faucher-Giguère C.-A., Quataert E., 2016, MNRAS, 459, 2311

McCourt M., Oh S. P., O'Leary R., Madigan A.-M., 2018, MNRAS, 473, 5407

Merten L., Becker Tjus J., Eichmann B., Dettmar R.-J., 2017, Astroparticle Physics, 90, 75

Mignone A., Bodo G., Massaglia S., Matsakos T., Tesileanu O., Zanni C., Ferrari A., 2007, ApJS, 170, 228

Mirabel I. F., Dijkstra M., Laurent P., Loeb A., Pritchard J. R., 2011, A&A, 528, A149

Miyamoto M., Nagai R., 1975, PASJ, 27, 533

Münch G., Zirin H., 1961, ApJ, 133, 11

Murray N., Quataert E., Thompson T. A., 2005, ApJ, 618, 569

Murray S. G., Power C., Robotham A. S. G., 2013, Astronomy and Computing, 3, 23

Nath B. B., Biermann P. L., 1993, MNRAS, 265, 241

Nath B. B., Madau P., Silk J., 2006, MNRAS, 366, L35

Nath B. B., Gupta N., Biermann P. L., 2012, MNRAS, 425, L86

Navarro J. F., Frenk C. S., White S. D. M., 1997, ApJ, 490, 493

Oppenheimer B. D., Davé R., 2006, MNRAS, 373, 1265

Pagel B. E. J., Patchett B. E., 1975, MNRAS, 172, 13

Penzias A. A., Wilson R. W., 1965, ApJ, 142, 419

Persic M., Rephaeli Y., 2014, A&A, 567, A101

Pfrommer C., Pakmor R., Schaal K., Simpson C. M., Springel V., 2017, MNRAS, 465, 4500

Planck Collaboration et al., 2014, A&A, 571, A16

Planck Collaboration et al., 2016, A&A, 594, A13

Prada F., Klypin A. A., Simonneau E., Betancort-Rijo J., Patiri S., Gottlöber S., Sanchez-Conde M. A., 2006, ApJ, 645, 1001

Ptuskin V., 2012, Astroparticle Physics, 39, 44

Ptuskin V. S., Moskalenko I. V., Jones F. C., Strong A. W., Zirakashvili V. N., 2006, ApJ, 642, 902

Puchwein E., Haardt F., Haehnelt M. G., Madau P., 2019, MNRAS, 485, 47

Putman M. E., 2017, An Introduction to Gas Accretion onto Galaxies. p. 1, doi:10.1007/978-3-319-52512-9_1

Putman M. E., Peek J. E. G., Joung M. R., 2012, ARA&A, 50, 491

Recchia S., Blasi P., Morlino G., 2016, MNRAS, 462, 4227

Reed D. S., Bower R., Frenk C. S., Jenkins A., Theuns T., 2007, MNRAS, 374, 2

Rees M. J., Ostriker J. P., 1977, MNRAS, 179, 541

Rosdahl J., Schaye J., Teyssier R., Agertz O., 2015, MNRAS, 451, 34

Ruszkowski M., Yang H. Y. K., Zweibel E., 2017, ApJ, 834, 208

Rybicki G. B., Lightman A. P., 1986, Radiative Processes in Astrophysics. Wiley-VCH

Salem M., Bryan G. L., 2014, MNRAS, 437, 3312

Salpeter E. E., 1955, ApJ, 121, 161

Samui S., Subramanian K., Srianand R., 2010, MNRAS, 402, 2778

Samui S., Subramanian K., Srianand R., 2018, MNRAS, 476, 1680

Sarkar K. C., Nath B. B., Sharma P., Shchekinov Y., 2015, MNRAS, 448, 328

Sazonov S., Sunyaev R., 2015, MNRAS, 454, 3464

Schaerer D., 2002, A&A, 382, 28

Schaye J., et al., 2015, MNRAS, 446, 521

Schmidt M., 1959, ApJ, 129, 243

Schmidt M., 1963, ApJ, 137, 758

Sérsic J. L., 1963, Boletin de la Asociacion Argentina de Astronomia La Plata Argentina, 6, 41

Sharma P., 2018, MNRAS, 481, L6

Sharma M., Nath B. B., 2012, ApJ, 750, 55

Sharma P., Roy A., Nath B. B., Shchekinov Y., 2014, MNRAS, 443, 3463

Shull J. M., Smith B. D., Danforth C. W., 2012, ApJ, 759, 23

Silk J., 1977, ApJ, 211, 638

Skinner M. A., Ostriker E. C., 2015, ApJ, 809, 187

Socrates A., Davis S. W., Ramirez-Ruiz E., 2008, ApJ, 687, 202

Speagle J. S., Steinhardt C. L., Capak P. L., Silverman J. D., 2014, ApJS, 214, 15

Spitkovsky A., 2008, ApJ, 673, L39

Steidel C. C., Giavalisco M., Dickinson M., Adelberger K. L., 1996, AJ, 112, 352

Strickland D. K., Heckman T. M., 2007, ApJ, 658, 258

Subramanian K., 2016, Reports on Progress in Physics, 79, 076901

Sur S., Schleicher D. R. G., Banerjee R., Federrath C., Klessen R. S., 2010, ApJ, 721, L134

Sutherland R. S., Dopita M. A., 1993, ApJS, 88, 253

Tang S., Wang Q. D., 2005, ApJ, 628, 205

Tegmark M., Silk J., Rees M. J., Blanchard A., Abel T., Palla F., 1997, ApJ, 474, 1

Tinsley B. M., 1980, Fundamentals Cosmic Phys., 5, 287

Tominaga N., Umeda H., Nomoto K., 2007, ApJ, 660, 516

Uhlig M., Pfrommer C., Sharma M., Nath B. B., Enßlin T. A., Springel V., 2012, MNRAS, 423, 2374

Vasiliev E. O., Vorobyov E. I., Shchekinov Y. A., 2008, A&A, 489, 505

Veilleux S., Cecil G., Bland-Hawthorn J., 2005, ARA&A, 43, 769

Venkatesan A., Truran J. W., 2003, ApJ, 594, L1

Vogelsberger M., et al., 2014a, MNRAS, 444, 1518

Vogelsberger M., et al., 2014b, Nature, 509, 177

Wakker B. P., et al., 1999, Nature, 402, 388

Weaver R., McCray R., Castor J., Shapiro P., Moore R., 1977, ApJ, 218, 377

Weibel E. S., 1959, Phys. Rev. Lett., 2, 83

Wiedenbeck M. E., Greiner D. E., 1980, ApJ, 239, L139

Williams R. E., et al., 1996, AJ, 112, 1335

Yoshida N., Abel T., Hernquist L., Sugiyama N., 2003, ApJ, 592, 645

Yoshida N., Oh S. P., Kitayama T., Hernquist L., 2007, ApJ, 663, 687

Zahid H. J., Dima G. I., Kudritzki R.-P., Kewley L. J., Geller M. J., Hwang H. S., Silverman J. D., Kashino D., 2014, ApJ, 791, 130

Zaldarriaga M., Furlanetto S. R., Hernquist L., 2004, ApJ, 608, 622

Zirakashvili V. N., Breitschwerdt D., Ptuskin V. S., Voelk H. J., 1996, A&A, 311, 113

de Graaff A., Cai Y.-C., Heymans C., Peacock J. A., 2019, A&A, 624, A48

de Vaucouleurs G., 1948, Annales d'Astrophysique, 11, 247

van den Bergh S., 1962, AJ, 67, 486

van den Bergh S., Abraham R. G., Ellis R. S., Tanvir N. R., Santiago B. X., Glazebrook K. G., 1996, AJ, 112, 359